2011

Sliding wear behaviour of eutectic Al-Si alloy under lubricated conditions: An investigation on the effect of ethanol (E85) addition

Victor Francis
University of Windsor

Sliding wear behaviour of eutectic Al-Si alloy under lubricated conditions: An investigation on the effect of ethanol (E85) addition

by

Victor Francis

A Thesis
Submitted to the Faculty of Graduate Studies
through Engineering Materials
in Partial Fulfillment of the Requirements for
the Degree of Master of Applied Science at the
University of Windsor

Windsor, Ontario, Canada

2011

Sliding wear behaviour of eutectic Al-Si alloy under lubricated conditions: An investigation on the effect of ethanol (E85) addition

by

Victor Francis

APPROVED BY:

_____

Dr. R. Riahi
Department of Mechanical, Automotive, and Materials Engineering

_____

Dr. J. Urbanic
Department of Industrial and Manufacturing Systems Engineering

_____

Dr. A. T. Alpas, Co-advisor
Department of Mechanical, Automotive, and Materials Engineering

_____

Dr. A. Edrisy, Co-advisor
Department of Mechanical, Automotive, and Materials Engineering

_____

Dr. H. Hu, Chair of Defense
Department of Mechanical, Automotive, and Materials Engineering

September 19, 2011

DECLARATION OF ORIGINALITY

I hereby certify that I am the sole author of this thesis and that no part of this thesis has been published or submitted for publication.

I certify that, to the best of my knowledge, my thesis does not infringe upon anyone's copyright nor violate any proprietary rights and that any ideas, techniques, quotations, or any other material from the work of other people included in my thesis, published or otherwise, are fully acknowledged in accordance with the standard referencing practices. Furthermore, to the extent that I have included copyrighted material that surpasses the bounds of fair dealing within the meaning of the Canada Copyright Act, I certify that I have obtained a written permission from the copyright owner(s) to include such material(s) in my thesis and have included copies of such copyright clearances to my appendix.

I declare that this is a true copy of my thesis, including any final revisions, as approved by my thesis committee and the Graduate Studies office, and that this thesis has not been submitted for a higher degree to any other University or Institution.

ABSTRACT

Bio-fuels such as E85 (85% ethanol and 15% gasoline) are clean and cost effective alternative fuel sources. Their effects on the tribological performance of the IC Al-Si engine alloy needs to be investigated. This study explores the ultra mild wear (UMW) mechanisms of an Al-12.6%Si alloy operating under a mixture of E85 fuel and motor oil (5W30) blended at a 1:1 ratio and only engine oil using boundary lubricated condition. Wear tests were conducted at room temperature using a pin-on-disk configuration and 52100 steel balls counterface. They show that samples lubricated with only engine oil and an engine oil E85 blend exhibited similar UMW characteristics. Lower wear rates were obtained when the engine oil was mixed with E85 fuel. Although the oil residue layer is of reduced thickness it is tribologically effective due to the formation of a protective tribochemical film by the alcohol.

To my dearest Kagi,

Thank you for your support, motivation, and above all your love

ACKNOWLEDGEMENTS

I would first and foremost like to express my sincere thanks to both my advisors Dr. Afsaneh Edrisy and Dr. Ahmet T. Alpas for their guidance, support and professionalism throughout the course of my studies. I would also like to thank Dr. M. Lukitsch from General Motors R&D Center for his support and encouragement.

I would like to thank my committee members for being part of my research and for taking their time to attend my seminars and providing me with valuable suggestions and comments.

To all my friends of the IRC Tribology of Lightweight Materials group for their contributions, support and encouragement. In particular, I would like to thank A. Aboughram and S. Dey for their help in starting this research and for all the help during my research.

I would like to express my gratitude to Nicholas Irish and Deborah Eckel from General Motors for providing me with XPS and FTIR scans. Dr. Xianying Meng-Burany for her time and patience in helping me with TEM observation and analysis.

Finally, I would like to thank my mother and father for providing me with the opportunity to continue my education. To Jude and Zincia for all their support and motivations. All my friends who have been with me through this experience. A special thanks to Chris for helping me to make some of the most important decisions in my life.

TABLE OF CONTENTS

LIST OF TABLES

LIST OF FIGURES

CHAPTER 2

CHAPTER 3

CHAPTER 4

CHAPTER 5

NOMENCLATURE

Abbreviations

AFM	atomic force microscopy
AOF	area of interest
BS	backscattered
COF	coefficient of friction
CrN	chromium nitrite
DLC	diamond-like carbon
EDM	electrical discharge machine
EDS	energy dispersive spectroscopy
EELS	electron energy-loss spectroscopy
EHL	elasto hydrodynamic lubrication
EP	extreme pressure
FIB	focused ion beam
FTIR	Fourier transform infrared
HR-TEM	high resolution transmission electron microscopy
IC	internal combustion
MML	mechanically mixed layer
Modtc	molybdenum dithiocarbamate
MW	mild wear
NIRAM	negative-ion-radical action mechanism
NSS	nitrided stainless steel
OCB	over based calcium borate

ORL	oil residue layer
RH	relative humidity
SEM	scanning electron microscopy
SI	spark ignition
SW	severe wear
TEM	transmission electron microscopy
Top-SIMS	time-of-flight secondary ion mass spectrometry
UFG	ultra fine grain
UMW	ultra mild wear
VSI	vertical scanning interferometer
XPS	X-ray photoelectron spectroscopy
XANES	X-ray absorption near edge structure
ZDDP	zinc dialkyl-dithiophosphate

Symbols

a	contact area radius
E	elastic modulus
E*	composite elastic modulus
H	indentation hardness
h_{min}	minimum film thickness
L	overall length
pH	acid/ base measurement
r*	r.m.s surface roughnessradius
R	radius of sphere

R_a	average roughness
Tm	melting temperature
U	sliding speed
ν	Poisson's ratio
VBI	viscosity blending index
W	normal load
w	load
w_{si}	weight fraction of silicon phase
Y	uniaxial yield stress
Z	asperity height
α	kinematic viscosity
η_o	dynamic viscosity
μ	coefficient of friction
λ	lambda
ψ	plastic index

CHAPTER I INTRODUCTION

The automotive industry has invested a large amount of resources in an attempt to improve modern passenger car emission standards through the reduction in the overall mass of the vehicle, improvement of energy conserving engine oils and improvement of bio-fuel technology for cleaner alternative fuels [1-2]. Another key area of focus has been on the elimination of cast iron cylinder liner and on the introduction of alternative aluminum based engine blocks. The technology was first attempted in the Chevrolet Vega, which offered a hypereutectic Al-18.5% Si alloy; however, large production costs and manufacturing issues forced the technology to be delayed [3]. Since then, advancements in casting technology and alloy development, coating technology, and manufacturing methods have allowed for cost effective ways for the linerless technology to be implemented once again.

The microstructure on the aluminum-silicon cylinder interface consists of silicon particles, which protruds above the aluminum matrix, and various inter-metallic phases. The concept of the linerless engine is that the harder silicon particles support the applied contact load from the piston rings while protecting the aluminum matrix. It is expected that under normal operating conditions, the engine should not experience more than a few nanometers of material removal per hour [4-5].

The progression of engine wear has been studied through post-mortem characterization of engine cylinder walls that followed dynamometer tests and various bench tests that incorporated operating temperatures, various oil additive interactions, and different loading configurations. It has been shown that the regime, which accurately

characterizes the low material removal observed in normal engine operations corresponds to the ultra-mild-wear (UMW) regime, which is less than 10^{-4} mm^3/m [6].

Chen and Alpas [7] and Dey et al. [5] observed wear of Al-18.5% Si alloy under lubricated sliding conditions under 0.5N and 5N respectively in order to understand the wear mechanism associated with Al-Si alloy. At 0.5 N loads, silicon particles began to fracture and sink into the matrix, supporting the direct load. Damage was limited to only a few scratch marks on top of silicon particles and it was concluded that the matrix did not sustain any damage. When loads were increased to 5N, a second stage was identified when the matrix became exposed to the counterface resulting in wear characterized as mild wear. Chen et al. [4] later characterized the wear behaviour of Al-Si alloys near the eutectic composition. The mechanism of UMW was identified as consisting of three stages. UMW I stage occurs during the period when silicon particles begin to fracture and sink into the matrix, allowing for aluminum to pile up. The second stage UMW II occurs over the period where the exposed aluminum matrix is removed resulting in rapid wear. The third stage UMW III occurs when a decrease in wear occurs due to the formation of a smooth and stable surface featuring a zinc based oil residue layer supported by an underlying structure of sliding deformation induced ultra-fine aluminum grains. Meng et al. [8] characterized the oil residue layer (ORL), which develops due to sliding at room temperatures under boundary lubrication with engine oil. The authors observed the formation of a thin ORL supported by the ultra fine aluminum grains that correlated the reduction in wear rates to the formation of the ORL. The layer consisted of a mixture of aluminum oxide and amorphous carbon as the main components, whereas constituents of the synthetic oil such as Zn, S, C, and Ca, become incorporated within the

layer. It was observed that increasing the sliding cycles increased the thickness of the layer.

Nicholls et al. [9] researched the formation of the tribofilm produced from zinc dialkyl dithiophosphate (ZDDP) on Al-Si alloys. The authors identified species of phosphide, unreacted-ZDDP, linkage isomer, and polyphosphate which develop on the wear track due to combined mechanical and chemical reactions from sliding contact under boundary lubrication. Pereira et al. [10] concluded that ZDDP resultant film formation under boundary lubrication consisted of zinc phosphates, zinc sulphides, and sulphates.

In recent years the demand for alternative fuels such as ethanol based fuels has resulted in vast amount of research into the combustion properties of ethanol/gasoline blends and the formulation of ethanol/gasoline mixes. However the impact of ethanol on the engine lubrication is limited. It is important to consider the effect of ethanol on engine lubrication since it differs from gasoline. Ethanol has a high latent heat of vaporization and a high boiling point (78^{o}C), making it possible for ethanol to find its way into the lubrication reservoir [11]. The high latent heat of vaporization makes cold start conditions particularly an area of concern and it has been shown that during cold start conditions extended cranking times are required leading to a high level of fuel dilution. If engine operating temperatures are below the boiling point of ethanol, the alcohol will not evaporate from the oil reservoir. Tung and Gao [12] studied the effects of 2% engine oils and 98% ethanol blended fuel mixtures (E85) under boundary lubricated wear conditions on cast iron liners and stated that fuels with higher acidity (4

pH vs. 6 pH) resulted in severe metal-to-metal contacts between piston rings and cylinder liner. Schwartz [13] investigated the effects of methanol fuel on engine oils pertaining to cast iron engine cylinder wear and concluded that the addition of methanol to engine oil caused no significant increase in the wear volume; however, stated that upper cylinder wear might be attributed to the ability of methanol to transport the additives away at the initial contact regions (upper cylinder). Hu et al. [14] explored the effects of alcohol as an impurity on ZDDP additives and concluded that alcohol decreased the degradation temperature from 215^{o}C to 145^{o}C, and increased the extreme-pressure properties, which allowed the load-carrying capacity to be improved, a combined effect which lead to an improved wear resistant lubricating oil.

In addition, concerning the wear resistance for aluminum alloys, using alcohols, diols, and amines, particularly implemented for cold rolling procedures, has been shown to reduce wear on aluminum alloys by forming a chemical film that separates the contacting bodies and thereby reduces wear [15]. Wan et al. [16], studied the effect of diol compounds on the friction and wear of aluminum alloys, attributed the mechanism of wear to tribochemical products which form on the surface between the diols and aluminum. The authors stated that differences in the structure of the diols can govern the ability of the diols to provide adequate wear resistance. Diols form bidentate bonds on the sliding surface, which acts as a protective film responsible for reducing friction and wear. Igari et al. [17] found similar film generation on top of the aluminum surface with aliphatic diols and glycols as lubricants on the wear of aluminum. Hu et al. [18] studied the tribological properties of alcohols as lubricating additives on aluminum and concluded that the antiwear mechanism is due to the chemi-adsorption of alcohols and

the formation of protective film on the contacting surface. The authors also stated that an increase in the hydroxyl group number of the alcohol improves the molecular polarity, consequently forming a more stable film. Hu et al. [19] offered evidence for the chemi-adsorption of amines onto the surface of the contacting body through FTIR analysis and suggested the formation of aluminum and amine protective film. Kubo et al. [20] used deuterium substituted ethanol during boundary lubricated wear and concluded that a tribochemical film (chromium ethoxide) does in fact occur during sliding contact with ethanol.

The lack of research in the area of linerless aluminum-silicon engine alloys under boundary lubricated sliding conditions with contaminated engine oil has prompted the need for an in-depth study. The objective of this study is to perform pin-on-disk wear tests under 2N loads to observe the wear behaviour of Al-12.6% Si under boundary lubrication in order to understand the effects of alcohol on the lubricating properties of the engine oil.

This thesis is organized into seven chapters. **Chapter 1** is an introduction to the objective and organization of this thesis. **Chapter 2** is a review of topics pertaining to the overall understanding of this thesis. Information has been provided to cover the alloy development, the different regimes of wear which are governed by its respective mechanisms, information of engine oil technology, and alternative fuel technology. **Chapter 3** covers the details pertaining to the testing procedures and methodology used throughout this thesis. **Chapter 4** is an accumulation of the observations and results from testing. This chapter details observations, calculations, and analyses in order to

determine the mechanism of wear. **Chapter 5** discusses in detail the progression of wear and the mechanisms which were observed during wear tests. **Chapter 6** presents the conclusions of this research based on all the observations.

CHAPTER II REVIEW OF THE LITERATURE

2.1 Introduction

The first section of this chapter reviews the principles of the internal combustion engine followed by properties of the specific engine alloy. A review on the implementation of linerless engine alloy has also been provided along with the different alloys used for linerless engine technology. The review continues on to the wear behaviour under dry lubricated conditions followed by a summary of the regimes and the wear mechanism and a review of lubricated sliding wear mechanisms. The review also covers the topic of engine oils and engine oil additives followed by a description of the contact mechanics in which they work. The final section of the review covers ethanol fuels and the effects on engine cylinder wear.

2.2 Internal combustion engine

The principle of internal combustion (IC), which is based on spark ignited petrol fuel or compression sparked diesel fuel, has had a global impact. In IC engines, chemical energy is transformed into mechanical energy and this technology is employed in motorcycles, scooters, mopeds, vans, trucks, buses, agricultural vehicles, construction vehicles, trains, boats, and ships [1]. The IC engine became a popular tool for its performance, reliability, and versatility; however, the process is far from efficient. Much of the energy from combustion is lost to thermal and frictional losses [1]. The typical IC engine configuration contains components such as rockers, valve springs, piston rings, an oil filter, journal bearings, an oil pump and oil, camshafts, valves, pistons, a cylinder block, con rod, crankshaft, and oil sump as shown in Figure 2- 2.

A study by Andersson [21] on the performance of a medium size passenger car, showed that from combustion, roughly 12% of the energy is used to drive the wheels of the car, and roughly 15% of the energy is lost through mechanical losses (friction). The author was able to estimate that if even 10% of the friction were to be reduced, a 1.5% increase in fuel consumption would be possible. When considering only the mechanical losses from an IC engine system, the components which contribute to mechanical loss through friction are displayed on a pie chart as shown in Figure 2- 2. Of these components, the skirt friction, piston rings, and bearings total roughly 66% of the total friction loss, and the valve train, crankshaft, transmission, and gears add to roughly 34% of the overall energy loss.

Improving the engine tribology performance through effective lubrication and design can greatly reduce fuel consumption, increase engine power output, reduce oil consumption, reduce harmful exhaust emissions, improve durability, reliably, and engine life, and reduce the maintenance required with longer service intervals.

2.2.1 Piston assembly

The piston assembly is the heart of the IC engine, where the proper amount of fuel and air mix together to create combustion. The piston assembly includes a series of metallic rings which serves to create an effective gas seal between the combustion chamber and the crankcase. The rings form a seal by closely conforming to the piston and the cylinder wall. The second function of the rings is to transfer heat from the pistons to the cylinder walls, which are in turn cooled by the circulating coolant and limits the amount of oil that is mixed into the combustion chamber. Shown in Figure 2- 3 is a schematic of the piston assembly. The grooves in the piston hold the piston rings in

place, while the piston skirt transmits the transverse loads from the piston to the cylinder walls. The top two piston rings are called the compression rings. The firing pressure pushes the rings outward conforming to the cylinder walls. These rings form the major gas seal and encounter the highest loads and temperatures because they are the closest to the combustion chamber. The top compression ring is typically coated with molybdenum for wear resistance purposes [1]. The second compression ring limits the upward oil flow in addition to providing a secondary gas seal. The bottom ring is the oil control ring, which limits the amount of oil transported from the crankcase to the combustion chamber.

The design and function of the piston assembly varies between manufacturers; however, the principal functions are quite similar. In order to provide appropriate wear resistance for piston rings and the cylinder wall, a variety of coatings and energy efficient lubricants can be employed. It is important to take into consideration the large variations in load, speed, temperature, and lubricant availability during the design of the piston assembly and coatings. The most common base materials for piston rings typically range from gray cast iron, malleable/nodular iron, carbides/malleable iron, and steels. Rings can be coated with chromium plating, flame sprayed molybdenum, diamond like carbon coatings (DLC), and nitrided stainless steel (NSS) in order to enhance wear resistance [1, 22]. Pistons were originally made from grey cast iron but have been replaced by aluminum for several reasons. Lighter alloys reduce the overall engine mass and reciprocating mass, which reduces engine vibration. The higher thermal conductivity of the aluminum helps transfer heat but must be designed for adequate clearance due to thermal expansion [2]. Cylinder bores are typically made from cast iron inserts, which

are incorporated into the engine block casting process. Recent development of single engine blocks from new light weight materials such as the aluminum silicon alloy and new thin film coatings for piston rings have allowed for the elimination of the heavy cast iron inserts [3-4, 7, 23-27]. The process of achieving a cylinder wall adequate for withstanding the combustion and necessary wear resistance will be discussed in the following sections.

2.2.2 Aluminum silicon alloy

Aluminum-silicon (Al-Si) alloys are among the most commercially used alloys desired for its wide applications. However Al-Si alloy have a poor resistance to wear in comparison to iron alloys. The challenge remains to find a cost effective way to make Al-Si alloys strong enough for engine application and importantly cost effective for high volume manufacturing. Such methods include the low-carbon thermal spray deposition process and surface etching to expose silicon particles [4, 7, 23, 26-27].

Aluminum-silicon alloys can be divided into three categories: eutectic, hypoeutectic, and hypereutectic alloys. Silicon as an alloy has the ability to reduce the thermal expansion coefficient, and increase corrosion and wear resistance [28]. The simple eutectic system consists of aluminum in the form of face center cubic and silicon in the form of diamond cubic structures. Murray and McAlister [29] compiled data from various publications to produce an Al-Si alloy phase diagram as shown in Figure 2- 4. Initially, solidification of the alloy occurs as the primary aluminum forms and grows in dendrite formation and/or the silicon phase forms and grows in angular primary particles [28]. Hypoeutectic alloys consist of 5-10% Si, whereas eutectic alloy consists of 11-13% Si, and hypereutectic alloy consists of 14-20% Si. A strong agreement on the eutectic

temperature at 557 +/- 1^{o}C and the eutectic composition at 12.2 +/-0.1 wt.% Si has been established based on a compilation of hundreds of experimental works and discussions [29].

2.2.3 Alloying elements for aluminum castings

Alloying elements are specifically chosen to achieve a desired property or to control the effects of impurities. Commonly utilized alloying elements for aluminum are copper, magnesium, manganese, zinc, and iron [28]. Elements such as copper, zinc, and magnesium are known to improve the hardenability of the alloy. Copper improves the tensile strength, machinability, and thermal conductivity of the alloy at the expense of reduction in ductility and corrosion resistance. Alloying elements are beneficial during the casting process by controlling the porosity content. Some alloying elements can influence the freezing range of the Al-Si melt, inherently influencing the porosity formation or aiding the formation of dendritic intermetallics during solidification, which in turn allows the porosity to form along intermetallic dendrites. An investigation into an Al-9 wt.% Si-3 wt.% Cu alloy illustrated that during solidification, pores did in fact nucleate along the sides of the β-Al_5FeSi needles [28]. However, an Al-Si-Mg alloy containing Sr showed that copper content over 0.2% increased the dispersed microporosity. The increase in copper content lead to an increase in the volume fraction of porosity in the casting. Iron content is typically found around 1.5-2.0%. Iron can induce Al-Fe-Si phase formation, which helps to prevent the die from sticking to the casting. Magnesium can be used to increase the hardness of the alloy through precipitation hardening by forming Mg_2Si phases throughout the matrix. Manganese has been found to modify the Al-Fe-Si phase, improving the ductility and shrinkage

properties in the alloy. Nickel has been found to be beneficial for high temperature applications by improving Si modification process and promoting primary Si precipitation in eutectic Al-Si alloys. Alloying elements such as sodium, phosphorus, titanium, and boron can affect the silicon phase morphology and have an influence on the grain refinement. Increasing the grain refiners increases the number of nucleation sites, leading to a decrease in both the volume fraction and size of pores, which in turn increases the overall homogeneity of the casting. Adding phosphorus to an Al- 9 wt.% Si- 3 wt.% Cu alloy displayed remarkable reduction in the porosity content [28].

Silicon particles have been shown to provide excellent wear resistance. Increasing the silicon content has been shown to increase the wear resistance of the alloy. Hypereutectic alloys have been implemented without cast iron linear inserts by preparing the Al-Si surface in order to allow the harder silicon particles to stand above the aluminum matrix, sustaining the loads [4, 7, 23, 30]. Alloys such as the Al-14%, Si- 2%, Cu-0.5%, as well as Mg-0.5% and Mn-0.05%, and Zr with -0.05% strontium have been found to have excellent machinability, high temperature capability, and wear and corrosion resistant properties, all of which are desired for linerless engine applications [28].

2.2.4 Alternatives to engine cylinder liners

Elimination of the cast iron liner with a homogeneous engine block will reduce the weight and improve engine performance through better heat transfer, while still maintaining the durability and performance. The aim is to achieve wear and scuffing resistance similar to or better than cast iron liners. The first linerless engine was manufactured by General Motors Corporation and was implemented in the Chevrolet

Vega engine as a light weight, durable, fuel efficient, and reliable engine [3, 31]. The engine was designed so that the pistons slide directly on the aluminum bore with no liners. The surface of the aluminum bore was first mechanically honed, followed by an electro-chemical treatment to expose the silicon particles above the aluminum matrix. The harder silicon particles provided the wear resistant layer capable of withstanding the conditions during combustion. With the elimination of the cast iron liners, the overall size of the engine became smaller and lighter for roughly the same production cost. Five different alloys were cast and tested. The base hypereutectic Al-Si alloy (A390) consisted of 16-18% Si, 4-5% Cu, 0.45-0.65% Mg, 0.5% Fe, 0.1% Mn, 0.1% Zn, and 0.2% Ti. It was found that the high concentration of silicon content offered comparable wear resistance as cast iron liners but posed difficulty under cold start conditions were insufficient lubrication lead to scuffing damage.

Riahi et al. [30] investigated the scuffing resistance of two eutectic Al-Si alloys (12.0 wt.% Si) in order to better understand the morphology of second phase particles and the optimal conditions which are needed for linerless engine application. Alloy A and B consisted of the same silicon percentages and alloying elements; however, alloy B consisted of a higher nickel content resulting in a higher number of second phase particles with a needle like morphology. The author correlated the time required for scuffing to initiate with the duration of etching time and stated that between 5 to 7 minutes of etching resulted in the best conditions for scuffing resistance, and prolonged etching past 7 minutes resulted in a weakening of the particles/matrix bonding due to excessive dissolution of the matrix as shown in Figure 2- 5. The ideal etching conditions expose the harder particles, which act as the load bearing elements and prevent the

counterface from coming into direct contact with the soft aluminum matrix. The fracturing of the silicon particles occurs due to the development of tensile stresses at the root of the silicon particles which anchors the particles to the matrix and results in the removal of relatively large fragments when they fracture. The edges of the particles also fracture and fragment when they come into contact with the counterface. The fractured pieces act as third body abrasive elements and in turn plough the matrix. Alloy B, which contained a higher concentration of nickel, resulted in a large number of hard phases per unit area with a needle like morphology, decreasing the scuffing resistance of the alloy. Larger needle like particles fracture more in comparison to smaller round particles found in Alloy A.

Das et al. [32] also confirmed similar results of the effects of surface etching by conducting lubricated wear tests on near-eutectic Al-Si alloy (10 wt.% Si) after etching the surface. The authors concluded that when the surface is etched, and the silicon particles are exposed, plastic deformation initiates at higher loads than what is observed under unetched conditions. Etching the surface reduces the peak contact pressure on the alloy and thus reduces plastic deformation. In order to understand the scuffing mechanism, an overall investigation of the mechanical, thermal, physical, and chemical interactions among the contacting bodies, the environment, the lubricant, and other species at the sliding interface must be considered. Scuffing has been associated with the breakdown in the lubrication film, and this has been supported by researchers. Researchers have also argued that a critical temperature criterion should be considered for the onset of scuffing to occur. The critical temperature is affected by material properties, engine operation conditions, and physical/chemical interactions between the

two contacting bodies. Studies by Wang et al. [33] investigated the wear behaviour of various piston ring coatings against cylinder bore in order to evaluate the scuffing mechanism. During testing, the authors describe the onset of scuffing when a sharp increase in coefficient of friction (COF) was noticed, indicating increase in metal to metal contact. Friction curves typically follow three stages: the break-in stage where the COF increases with the normal load, followed by a steady stage where it stabilizes. The final stage occurs during failure where the COF increases sharply and is associated with scuffing. At the onset of contact, the peaks of the machining marks are first to come into contact and begins to flatten due to wear, increasing the contact area. The oil film is able to partially support the load and operates under a mixed lubricated regime. If the loads are increased and temperatures start to rise, the boundary lubrication regime is achieved. During scuffing, the two surfaces directly contact each other under starved lubricated condition. In order to better classify scuffing, the authors adopted the following statement: "Scuffing is a sudden departure from proper functioning of lubricated sliding pairs, resulting in a progression toward catastrophic surface failure." The newly developed engine alloy cylinder bore exhibited promising scuffing resistance; however, the scuffing resistance is affected by surface porosity. Higher porosity levels result in lower scuffing resistance. Surface hardness and substantial intermetallic phases, along with eutectic silicon phase, also provide additional wear resistance and beneficial tribo-chemical reactions.

2.3 Behaviour of aluminum silicon alloys in dry sliding conditions

2.3.1 Wear regimes in Al-Si alloys

Before understanding the wear mechanisms involved during the contact of two surfaces, it is important to identify which type of wear regimes exist with Al-Si alloys. The fundamental work was first published by Lim and Ashby [34] who developed an empirical wear map to summarize the wear rates and wear mechanisms for *steel-on-steel* contact under dry sliding as shown in Figure 2- 6. The authors reported on regimes of ultra-mild wear, delamination wear, mild-oxidation wear, severe-oxidation wear, melt wear, and seizure.

When observing the wear behaviour of Al-Si alloys, it is evident that different regimes can be achieved based on varying sliding conditions. Liu et al. [35] compiled various experimental results to develop a physical model similar to what was initially developed by Lim and Ashby [34]. Improving on the models, an empirical wear map for Al-Si alloy was generated as shown in Figure 2- 7. The importance of this particular map allows for a broad observation of the different wear regimes and mechanisms which exist for a given condition. It is essential to realize that within each regime, the dominant wear mechanism is different and can be changed by varying parameters such as speed, load, and atmospheric conditions. Based on these novel ideas and methodology, Zhang and Alpas [36] investigated the working mechanism of delamination wear by conducting dry sliding wear tests on Al-7% Si alloy; this is particularly important in order to determine the stress and strain distributions as a function of sliding distance and applied normal loads. The authors concluded that both the magnitude of the strains and the depth of the deformed zones increase with sliding distance and applied load. Using the Voce

equation, strain hardening of the material was calculated and illustrated to show that towards the contacting surface, hardening capacity of the material was exhausted and exponentially decreased when moved further away from the surface. Void nucleation sites initiated at Al-Si interfaces and linked together to form subsurface cracks below the surface as shown in Figure 2- 8. When the subsurface cracks reach the surface, delamination of the material occurred. Zhang and Alpas [37] proceeded to study the transition point from one regime to another on Al-Si (6061) by changing the load, sliding velocity, and sliding distance, allowing them to understand how each condition effects the transition point. The authors reported that wear rates were mild at low loads and increased gradually until the material experienced a transition from mild to severe wear as indicated by a sharp increase in the slope of the wear rate versus load curve as shown in Figure 2- 9. It was evident when observing the wear debris and wear scar that severe wear generated massive surface damage, larger scale aluminum transfer to the counterface, and the generation of coarse debris. Transition from mild to severe wear was observed when the bulk surface temperature T_b exceeded a critical temperature limit when the load or sliding speeds were increased. The temperature increase affects the hardness of the matrix, which was made evident by the recrystallization of the matrix. This implied that the transition point was not a single influencing factor but a combination of systems acting together.

The most commonly reported wear regimes for an Al-Si system contacting with a steel counterface are the mild wear (MW) and severe wear (SW). Mild wear occurs under low loads resulting in wear rate between 10^{-4} and 10^{-3} mm^3/m. Severe wear occurs under higher loads, higher temperatures and high sliding velocity producing wear rates of

$>10^{-2}$ mm3/m. Figure 2- 10 shows a wear rate versus load map for an Al-Si binary system and various Al-Si systems with Cu, Fe, and Ni as the alloying elements [38]. The binary Al-Si system contains a transition point at 30N where the regimes change from mild wear to severe wear. This transition signals a change in the mechanisms. Alloying with 2% Cu increased the transition point from 30N to 80N, similarly when Ni and Fe were added the transition point only increased slightly.

Yen and Ishihara [39] and Goto et al. [40] postulated that testing conditions such as humidity, atmosphere, and counterface materials were factors which can all change the tribological properties of any system under observation. An important observation was made by Elmadagli et al. [41] when studying the sliding behaviour of Al-18.5%Si, Al-8% Si, and Al-25% Si in a controlled dry environment containing 5% relative humidity. The authors reported that the transition from mild to severe wear exists for all the alloys tested; however, two new sub-regions of wear were observed. Evidence for the ultra-mild wear (UMW) regime was provided with wear rates below 10^{-5} mm^3/m. The state of UMW was achieved when loads of 10N were used during contact with 52100 stainless steel counterface in an argon atmosphere. When the counterface was changed to a diamond like carbon (DLC)-coated steel counterface running in dry air (RH 5%) atmosphere, the same condition of UMW was achieved.

2.3.2 Wear mechanisms in Al-Si alloys

The characterization of wear regimes can only be completed by understanding the mechanisms that induce damage. Following a physical modelling approach first outlined by Lim and Ashby [34] for steels, Liu et al. [35] combined their experimental data with data collected from the literature to develop the wear map for aluminum alloys as shown

in Figure 2- 7. The authors identified different wear regimes, which were each obtained by varying both the contact pressure and sliding velocity, and proposed a mechanism for each regime. As an example, at relatively low speeds and loads, the heat generated by the asperity contact leads to oxide formation on the aluminum surface. The layer is thin and can deform elastically contributing to very low wear rates which the author considers ultra-mild wear. Increasing the load causes adhesion to occur between the two materials in contact and removal of the surface oxide in the form of laminar particles ranging in size from 50 to 200μm. Delamination wear involves plastic shearing of the metal. Subsurface nucleation of cracks propagates to the surface resulting in particle-like wear debris generation also observed by Zhang and Alpas [36].

Li and Tandon [42] investigated the sliding wear behaviour of Al-Si alloys against tool steel and reported that a mechanically mixed layer (MML) formed comprised of elements from both sliding materials. Initial contact occurred between asperities on the microscopic scale leading to high compressive pressures and large shear strains in the asperities, which further progressed to a large number of dislocations in cells and elongated subgrains. The formation of the early fragments from the contacting surfaces mix together and in turn, compact and smear under the applied loads. These mixed and compacted materials progressively accumulate and as a result, transfer layers are created. The formation of the MML provides a layer of protection and can act similar to a solid lubricant. Under low loads, the MML consisted mainly of α-Al and α-Fe, whereas under high loads, intermetallic compounds of FeAl and α-Al_2O_3 exist. The formation and removal of the MML will inherently control the amount of wear as a result of dry sliding.

Work by Li et al. [43] explored the properties of tribolayers as a result of sliding wear under different atmospheric conditions in order to relate the content of oxygen to the mechanical nature of the tribolayer. The authors found that the layer which formed in air was richer in oxygen (32.5 wt.%) and iron (24.8 wt.%) than the layer which formed in argon (13.3 wt.% of oxygen and 1.2 wt.% iron). Under both conditions of sliding, the development of ultra-fine aluminum grains occurred, which was attributed to severe plastic deformation. The microstructure of the layer under air was more brittle due to the high amount of oxide which leads to more fracture (800 ± 100 kg/mm^2). Under the argon atmosphere the lower quantity of oxygen resulted in a less brittle and softer layer delaying fracture of the layer (400 ± kg/mm^2). The morphology of the two layers is shown in Figure 2- 12 where the layer in argon was almost featureless. The layer under air was more brittle with networks of cracks.

Reddy et al. [44] reviewed the conditions necessary to induce seizure on Al-Si alloys under dry sliding conditions. The authors stated that the mechanism of seizure of Al-Si alloys is related to the bulk shear stress of the material, where the frictional forces and the resistance to shear are the controlling factors. Friction forces are determined by the hardness of the alloy, whereas the resistance to shear is inversely proportional to the hardness. At higher sliding speeds the frictional forces increase the temperature which reduces hardness and the resistance to shear. This was also observed by Zhang and Alpas [37] who investigated the effects of applied load and sliding velocity in aluminum alloys to further understand the transition from mild to severe wear. No single wear mechanism can be attributed as the rate controlling mechanism throughout the mild wear regime. It was found that low loads and velocities produced sub-microscopic aluminum and iron

particle debris which initially detach from the contact surfaces. This mechanically mixed phase predominantly consisted of aluminum oxide. The hardened aluminum oxide then facilitates the detachment of iron from the steel counterface to produce the iron debris. This debris deposits on the surface and from time to time spalls off, contributing to wear. Increasing the loads or sliding speeds would inherently increase surface temperatures to a critical point near the transition area, softening the material. Subsurface crack initiation and propagation are attributed to the detachment of the layers. It was also concluded that the wear resistance of aluminum alloys can also be increased through reinforced misconstrues such as SiC particles or Al2O3 which increase transition loads.

Wilson and Alpas [45] correlated the effect of applied load and velocity on Al356 Al-Si alloy with 7.0 wt.% Si and A356 alloy with a 20% SiC composite. It was found that the transition onset for both alloys was achieved when a critical surface temperature ($0.4T_{melting}$) was reached. They observed that in the severe wear regime, the specimen generally experienced an initial period of mild mixed oxidation type wear prior to the onset of seizure by extensive plastic deformation and material transfer to the counterface. At higher loads and high sliding speeds, immediate seizure was noticed. Alloys containing 20% Si showed that similarly a transition point from mild to severe wear existed depending on applied load and sliding speed. However this material was able to withstand higher loads before showing signs of severe wear. Increasing the load and sliding speed resulted in higher wear but was not severe enough to induce seizure.

2.4 Behaviour of aluminum silicon alloys under lubricated conditions

2.4.1 Lubrication regime and its properties

Hydrodynamic lubrication occurs when the sliding surfaces are separated by a thick film of lubricant. Due to the relative motion of the surfaces, internal viscous forces are created. The pressures which are hydrodynamically created support the normal loads. In hydrodynamic lubrication, the friction is caused by the shearing of the fluid because the fluid completely isolates both surfaces, and the asperities do not come into contact. Equilibrium is achieved under the condition in which the load and hydrodynamic pressures equal each other. Lowering the sliding speeds and increasing the load will increase the local pressure on the film and in turn increase the film viscosity resulting in asperities that come into contact and progress into elastohydrodynamic lubrication.

Under a mixed lubrication or elastohydrodynamic lubrication, the load carrying becomes a combined effect of hydrodynamic pressure and the contact pressures between asperities. In the event that the sliding velocity of the moving surfaces decreases or if an increase in the normal load or an increase in the lubricant temperature occurs, a decrease in viscosity will result. Any one of these condition may prevent the formation of hydrodynamic lubrication film to occur. In this regime, the defining characteristics are the fluid viscosity, the viscosity-pressure coefficient, and the elastic coefficient of the solid surface.

Under extreme loads or low sliding speeds, the regime enters boundary lubrication which can be characterized by three points: (i) the friction surfaces which contact at the asperities, (ii) the hydrodynamic effects of lubricating oil or rheological characteristics of bulk which do not significantly influence the tribological

characteristics, and (iii) interaction in the contact between friction surfaces and between friction surfaces and the lubricant (including additives) that dominate the tribological characteristics.

The nature of the contact can be modelled by representing it as a sphere and a flat plate. An equation can be derived in order to determine the minimum lubricant film thickness (h_{min}) at the contact point based on the radius of the sphere (R), the viscosity constants of the lubricating fluid (η_o and α), the sliding velocity (U), the applied normal load (W), and the reduced surface modulus as described by Hertzian theory (E*):

$$h_{min} = 1.79R^{0.47}\alpha^{0.49}{\eta_o}^{0.68}U^{0.68}(E*)^{-0.12}W^{-0.07} \quad (2.1)$$

By representing a ratio (λ) of fluid film thickness over the r.m.s surface roughness (r*), a relationship to measure the potential for asperity contact to occur can be created. When the ratio of $\lambda>3$ is achieved, a full fluid film will separate the two surfaces through hydrodynamic lubrication. When the ratio falls between $1< \lambda <3$, partial contact between asperities occur and the regime can be considered as elasto hydrodynamic lubrication (EHL). If the ratio $\lambda<1$ occurs, the fluid film does not develop and boundary lubrication occurs.

2.4.2 Lubrication additives and engine oils

Modern engine oils are manufactured by blending base oils with a wide range of additives. Base oils are comprised of different hydrocarbons generally classified into three paraffinic groups in which the naphthenes have long side chains; naphthenic which have short side chains; and a combination of both [46]. Lubricant additives can be either

organic or organo-metallic chemicals which are added in order to improve the lubricating capacity and durability of base oils. Various additives are used in order to achieve a specific quality in the oil such as improving the wear and friction characteristics, improving the oxidation resistance, prevention of corrosion, and controlling the contamination due to combustion products. Among the additives, the most common anti-wear additive is zinc dialkyldithiophosphate (ZDDP). ZDDP additive is used mainly for its antioxidant and antiwear properties. As an antioxidant, ZZDPs undergo a series of molecular processes which forces them to form organo-substituted phosphates, thiophosphates, and phosphorus acids which are incorporated into the antiwear films [47-48]. The decomposition route of ZDDP can depend on many factors such as (but not limited to) temperature and the chemical environment. The overall decomposition ultimately proceeds to the formation of antiwear film precursors which include phosphorus, oxygen, sulphur, and zinc. The details of the ZDDP film formation will be explained in later chapters; however, the overall process occurs by first reacting with the metal surface or from the film precursor products. The initial layer serves as a bonding layer between the metal substrate and the bulk antiwear film. The film thickness can vary up to 100 nm depending on the sliding conditions and environment in which they interact.

Detergents can include calcium and magnesium sulphonates, phenates, and salicylates [47]. They exist in the form of basic, neutral, or over-based and act to keep the oil insoluble contaminants and degradation products in suspension and to neutralize acids. The variation in the structure of the detergent can influence the effectiveness to neutralize acids. The neutral structure is simple divalent metal usually calcium or

magnesium bonded to an alkyl substituted suffonate, phenate or salicylate anion. More effective detergent packages such as the basic or the overbased packages contain an increased number of divalent metals and metal carbonate particles. These become extremely useful for preventing damage from acids created from by-products of combustion. Detergents can also be considered as antiwear additives; however, they are far less superior to ZDDP, and typically friction forces are higher. Detergent products can also absorb onto the metal surface even without rubbing, although in the presence of mechanical stress, a coherent film forms as a compacted amorphous metal carbonate film known to sustain contact pressures on the order of 100 MPa [47]. Dispersants are primarily used to suspend oil insoluble contaminants and degradation products. They are more effective under low temperature environments.

2.4.3 Antiwear film formation

The formation of antiwear films is crucial in reducing wear, and it has been shown to be a combined effect of many conditions including sliding conditions (hardness, roughness, load, temperature, sliding speed) and chemical environment [4, 7, 9, 23, 49-52]. The most widely studied antiwear additive is ZDDP. The structure of ZDDP is shown in Figure 2- 13. The structure contains four sulphur atoms arranged equivalently in a tetrahedron around zinc. ZDDP has the ability to form either a thermal film under high temperatures or a tribofilm under mechanical stresses [48, 51]. When ZDDP is heated above 100^{o}C, a transparent, solid, reaction film forms on the metal surface. The rate of thermal film formation increases with temperature and can reach up to 200 nm in thickness on steel surfaces [48]. Wear tests on thermally formed films showed that they are resistant to wear and can survive for a number of hours when rubbed in base oils [48].

The thermal film appears to develop as separate islands to form a mound-like structure which develops into smooth structures.

Heuberger et al. [51] employed x-ray photoelectron spectroscopy (XPS) analysis to study the effect of temperature on ZDDP tribofilm composition using the ball-on-disk setup with an AISI 52100 steel ball. The authors demonstrated that the temperature has a significant influence on film formation for both thermal films and tribofilms, which are formed under stress. Low temperature thermal and tribofilms were calculated to be very thin (1-2 nm), and upon increasing the temperature to 180^{o}C the thermal film grew to about 2-4 nm thick and the tribofilms grew to greater than 6 nm thick. The thickness of the films increased with increasing temperature. At room temperature the films mainly consisted of adsorbed dialkyldithiophosphate and at intermediate temperatures changed to short-chain zinc phosphate and to a cross-linked polyphosphate at 180^{o}C.

An extensive study into the chemical composition of tribofilms were conducted by Nicholls et al. [9] on Al-Si alloys using X-ray absorption near edge structure (XANES) analysis. Films were generated on A319/A319, A319/52100, 52100/A319, A6061/A6061, A6061/52100, and 52100/A6061 systems, and the results from the P K-edge spectrum are shown in Figure 2- 14. The first four spectra show unreacted ZDDP, Zn Phosphide (Zn_3P_2), Zinc polyphosphate ($Zn_4P_6O_{19}$), and the standard film, respectively. The standard film was considered as the intended target for an ideal film because this film was shown to have the lowest wear. In spectra A for the A319/A319 system, three peaks were detected on the surface, which were a combination of unreacted-ZDDP and species of phosphide and phosphide. When steel was introduced

into the A319/52100 and 52100/A319 systems, only polyphosphate films resembling the standard film was noticed. For the A6061/A6061 system, peaks from unreacted ZDDP and polyphosphate peaks were detected. Under the A6061/52100 system, unreacted ZDDP and phosphide species were noticed. The standard film was not detected until the 52100/A6061 was used. It was noted that when unreacted-ZDDP and phosphide were detected, large amounts of wear occurred. The authors also showed the development of the film as a function of rubbing time, shown in Figure 2- 15. It was observed that under the A319/A319 system, species of unreacted-ZDDP and polyphosphate were detected. The formation of phosphide species were also detected but decreased as the sliding time increased. When steel was introduced into the system, after 5 minutes of sliding, fully formed polyphosephate species were detected. Based on observations made the authors concluded that in order to form a good and sustainable film, four conditions must be met: (i) the temperature in the contact zone between the rubbing couple must be high enough to transform ZDDP to form an antiwear film, (ii) the hardness and yield strength of the couple must be similar to sustain the film, (iii) the antiwear film must be glassy and have yield strength less than the surfaces in contact, and (iv) a third body abrasive must not be present in the contact zone.

Grossiord et al. [52] explored the tribochemical interactions between antiwear zinc dithiophosphate (Zndtp), friction modifier molybdenum dithiocarbamate (Modtc), and over based detergent calcium borate (OBC) lubricant additives. The author reported that under rubbing stresses, the tribofilms which are generated provide good wear resistance and acceptable surface friction values. XPS analysis was then used in order to determine the composition of the elements from additives and showed that the films

consist of C, O, P, B, S, Mo, Zn, and Ca. A combination of the binary or ternary systems results in similar wear behaviour with slight variations in the film formation and friction forces. The thermal film which is generated under room temperature consisted of absorbed dialkyldithiophosphate molecules on the iron oxy-hydroxide, together with zinc oxide. When mechanical stresses were applied to generate the tribofilm, it consisted of zinc orthophosphate $Zn_3(PO_4)_2$, zinc sulphate, zinc oxide, and zinc/iron sulphides. When temperatures were increased to 60^{o}C, both thermal and tribofilms were similar to the film generated at room temperature but consisted of higher amounts of zinc orthophosphate. At temperatures of 90-110^{o}C, the thermal film consisted of a mixture of zinc orthophosphate and zinc pyrophosphate together with zinc oxide and sulphur. The tribofilm at this temperature resulted in film with more zinc phosphate but less zinc sulphate.

2.4.4 Wear behaviour of Al-Si alloys under boundary lubricated conditions

The regime which accurately portrays the action of the piston ring and the Al-Si interface is found to be ultra mild wear regime. The development of the linerless Al-Si alloy has evolved from many stages based on bench tests and dynamometer tests [3, 28, 30, 53-54]. Chen et al.[23] began to first observe the consequence of matrix hardness on Al-11%Si and Al-12% alloy. The two alloys had similar silicon morphologies; however, the hardness of the Al-11% Si was higher than that of Al-12% alloy. Operating under boundary lubrication, using only 0.5 N loads, the author calculated contact pressures for both alloys, stating that a harder matrix would impede wear. Under ultra mild wear, Al-11% Si exhibited less damage than the softer Al-12% Si, which lead to the conclusion that the matrix hardness was determined to be a controlling factor for wear loss.

Chen et al. [4] extended the investigation into the micromechanisms and the mechanics of ultra-mild wear on hypereutectic Al-Si alloys by performing wear tests using 0.5, 1, and 2 N loads under boundary-lubricated conditions. At low loads of 0.5 N, small numbers of fractured silicon particles were observed within the wear track. It was concluded that the damage mechanism included: (i) wear of the top surfaces of silicon particles, (ii) fracture of some silicon particles, and (iii) a reduction of particle height without visible damage to aluminum. When observing the wear mechanism at 1 N load, the addition of local damage to the aluminum adjacent to the silicon particles became apparent. Through SEM analysis, Si particles inside the wear track became partially embedded in the aluminum matrix as shown in Figure 2- 16. Si particle sink-in is accompanied by the formation of aluminum pile-up around these particles. Pile-up occurs in order to accommodate the displacement caused by the rigid particle indentation into the plastically deforming matrix. When silicon particle damage occurs due to the sink-in process, direct contact between aluminum and the counterface materializes which leads to the formation of scratch marks on the aluminum matrix; however, no mass loss can be detected. The 1 N load wear mechanism consist of the following: (i) particle fracture and fragmentation, (ii) particle sinking-in and embedding into the aluminum matrix, (iii) development of aluminum pile-up adjacent to the sunken-in particles, and (iv) slight wear damage on the aluminum in the form of surface scratches, but with no measureable material loss.

Observation of the 2 N track showed that silicon particles appear to be fully embedded into the aluminum matrix. Almost all silicon particles were fractured. The continuous scratch marks that appeared on the aluminum surface were identified as an

important contact damage feature. The wear track was covered with a solid tribolayer with a glassy appearance after sliding as shown in Figure 2- 17. This layer forms during the course of sliding, and XPS analysis showed that it consisted of a mixture of carbon and other constituents which include Ca, S, and Zn that originated from the synthetic oil. Electron energy-loss spectroscopy (EELS) showed that the carbon in the oil residue layer had an amorphous structure; it also identified the aluminum oxide as one of the main constituents of the layer.

The microstructure directly below the oil layer showed the formation of a deformation microstructure consisting of ultra-fine aluminum grains. After the fracture and sinking-in of silicon particles, wear of aluminum matrix became evident. This tended to stabilize when an oil residue layer was established. The UMW mechanism consisted of the following: (i) initially, wear to the top surfaces of silicon particles occurred along with particle fracture and particle sinking-in. This is referred to as UMW I, where the damage was limited to the silicon particles and the aluminum matrix remained protected. (ii) The aluminum was no longer sheltered, and measurable quantities of material loss occurred in UMW II. (iii) The UMW II stage was not persistent, and the rate of damage decreased due to the formation of the oil residue layer on the contact surface as well as the formation of a subsurface structure consisting of ultrafine aluminum grains entering UMW III stage [4].

Comparison of 11% Si and 25% Si microstructures revealed that the estimated maximum contact pressure applied to the particles in 11% Si was about 1.6 times higher compared to 25% Si, primarily because of the smaller area density of silicon on the

contact surfaces [7]. The larger pressure exerted on the silicon particles combined with the lower matrix hardness caused the silicon particles to exhibit a greater decrease in height. The oil residue layer was approximately 150 nm thick. The formation of ultra fine aluminum grains can be attributed to the generation of large subsurface strains when aluminum comes into sliding contact with the counterface during the UMW II stage. Under the contact surfaces, a hydrostatic stress field exists that facilitates the development of large strains without allowing subsurface voids or cracks. Once an ultra fine subsurface microstructure is established during the sliding process, it is conceivable that the hardened subsurface will help to sustain the oil residue layer above it, and these newly generated surfaces appear to be effective in restraining the extension of high wear rate in the UMW II stage to high sliding cycles. Similar results were also achieved by Dey et al. [5]

Meng et al. [8] further characterized the protective tribolayer development by employing ion beam and cross-section transmission electron microscopy (TEM) techniques on Al-11% Si alloys under boundary sliding conditions. The author stated that after the course of sliding, the stabilization of wear rates were due to the development of a protective thin oil residue layer supported by ultra fine aluminum grains. The formation of ultra fine aluminum grains are a result of large hydrostatic pressure fields which were calculated, based on Bridgman's method, to be around 3-5 GPa of hydrostatic pressure and plastic strain on the order of 5-7. The protective oil layer consisted of aluminum oxide and amorphous carbon as the main component; whereas, components of the oil additives such as Zn, S, Mo, and Ca become incorporated into the

layer. The evolution of the film was observed to grow thicker up to 110 nm as the number of laps increased.

Slattery et al. [24-25, 55] studied the evolution of wear on Al-Si engine alloy after high load, high speed, and high temperature durability dynamometer tests. The author found that the development of wear resistance was due to a combining effect of oil deposits, silicon particle exposure, and ultrafine aluminum grains. The silicon particles experience fracture and reduce to roughly 0.6-0.7μm in height and prevent direct metal-to-metal contact between the piston ring and the matrix. The surface was covered with a rich layer of amorphous oil residue consisting of P, S, Zn, Ca, C, and O. The exposed silicon particles do in fact support the majority of the loads, whereas the aluminum underneath transform into ultra fine grains in order to accommodate the loads and pressure.

2.5 Measurements and surface profiling

2.5.1 Surface profiling

In order to understand contact mechanics, the measure of surface roughness is a crucial subject to cover. Methods such as electron microscopy, optical microscopy, stylus profilometry, and recently atomic force microscope (AFM) can all be utilized in order to study the topographic features of the surface. The measure of surface roughness is typically represented by the average roughness (R_a) which is defined as the arithmetic mean deviation of the surface height from the mean line through the profile. The mean line is defined so that equal areas of the profile lie above and below this line as shown in Figure 2- 18 [56]. The average roughness can be represented by the equation below;

$$R_a = \frac{1}{L}\int_0^L |y(x)| d_x \quad (2.2)$$

where *y* is the height of the surface above the mean line at a distance *x* from the origin along the overall length *L*.

2.5.2 Contact between surfaces

When two surfaces come into relative contact with one another, contact will initially occur at the highest points known to be asperities. When the load increases, the surfaces move closer to each other resulting in an increase in the area of surfaces in contact. Since the asperities isolate the rest of the surfaces, they are inherently responsible for supporting the normal load. If the surfaces slide against each other, the points of the asperities then control the frictional forces.

The asperity can be considered as a blunt object, modelled as perfectly smooth protuberances of spherical, conical, or pyramidal shapes. If a spherical asperity is pressed against a plane with a load of *w*, the contact is a circular area of radius *a*, which can be modelled through a Hertz derived equation as illustrated in Figure 2- 19 [56],

$$a = \left(\frac{3wr}{4E}\right)^{1/3} \quad (2.3)$$

The radius of the asperity is considered to be *r*, and *E* is the elastic modulus depending on E_1, E_2, and the Poisson's ratios v_1, v_2.

The value of Young's modulus E is then calculated using the following equation:

$$\frac{1}{E} = \frac{\left(1-{v_1}^2\right)}{E_1} + \frac{\left(1-{v_2}^2\right)}{E_2} \quad (2.4)$$

The area of contact can be modelled as:

$$\pi a^2 \approx 0.83\pi(\frac{wr}{E})^{2/3} \quad (2.5)$$

When considering a purely elastic case, the area of contact is proportional to $w^{2/3}$. If considering a plastic deformation case, the analysis can be considered depending on two conditions. The first condition assumes that the sphere is rigid, and plastic flow is confined to the plane. The second condition assumes that the plane does not deform, and plastic flow occurs only in the sphere. If the sphere is rigid, the maximum shear stress beneath the indenter occurs at a depth of about *0.47a*, where *a* is the radius of the contact circle. Plastic flow occurs once the yield criterion is satisfied. Plastic deformation initiates at a mean contact pressure of *1.1Y*. *Y* is the uniaxial yield stress of the material. The mean pressure over the contact area will reach *3Y*. It does not matter which component yields, but the mean pressure over the contact area will always be of the order of three times the uniaxial yield stress of the softer material.

2.5.3 Simple theory of multiple asperity contact

The problem is approached by considering the contact between a single rough surface and a rigid frictionless plane. The rough surface will have an array of spherical asperities of constant radius and height and each asperity will deform independently of all the others. Each asperity will bear the same fraction of the applied load. The total real area of contact will be related to the total load exactly the same way as an individual asperity. If elastic case is considered, then

$$A \propto W^{\frac{2}{3}} \quad (2.6)$$

If considered as plastic behaviour,

$$A \propto W \tag{2.7}$$

2.5.4 Statistical theories of multiple asperity contact

It is assumed that all the asperities have spherical surfaces of the same radius *r*, and that they will deform elastically under load according to Hertz's equations. The load *w*, can be predicted by:

$$w = \frac{4}{3} E r^{1/2} (z - d)^{3/2} \tag{2.8}$$

The height is statistically distributed. Figure 2- 20 can be used to illustrate the use of this equation. The height above the reference plane is *z*, the separation between the reference plane and the flat surface is *d*. If d is less than *z*, elastic deformation is considered. This consideration is on the basis of purely elastic contact. For plastic flow considerations, the plastic index is given by:

$$\psi = \frac{E}{H} \left(\frac{\sigma^*}{r}\right)^{1/2} \tag{2.9}$$

Where H is the indentation hardness, E is the elastic modulus, and σ^* is the standard deviation of the distribution of the asperity height. If the index is less than 0.6, plastic flow at the asperities would be caused only by extremely high normal pressures. If the index is greater than 1, most asperities will deform plastically under even the lightest loads.

2.6 Ethanol fuels and effects on engine oil contamination

2.6.1 Ethanol and fuels

The use of alternative fuels and alternative fuel vehicle development has seen a steady increase as a way to lessen the dependency on imported oil [57]. Early automakers such as Henry Ford saw the potential of ethanol because of its availability; he considered that it could be the world's primary fuel source. According to the US department of Energy, studies have shown that by 2030 ethanol and other bio fuels can replace 30% or more of the US demand [58]. Roughly two-thirds of the US petroleum demand is in the transportation sector. In order to meet the demand of the economy, about sixty percent of the petroleum is imported from foreign nations. Ethanol on the other hand can be manufactured on domestic soil and alleviate the need to import [59]. Ethanol is a clear, colourless liquid derived from various plant matters making it a renewable source of energy. The composition of ethanol contains the hydroxyl group (-OH) bonded with carbon atoms to form C_2H_5OH. The availability of corn in the US has made it the most used material to derive ethanol from; whereas, in Brazil, ethanol is derived from sugar canes. Ethanol is a high-octane fuel which delivers a higher compression ratio. Pure ethanol can replace gasoline on modified engines; however, up to 20% may be added to fuel in order to be used on unmodified engines [57]. Ethanol is produced from starches found in grains, which are converted to sugar and fermented. A second method of deriving ethanol is through hydrolysis of cellulose which is found in plant-based materials; this allows for a wide range of materials to be used such as corn stalks, wheat stalks, other agricultural or forestry waste, and municipal waste. The process to produce fuel ethanol is similar to the process to produce beverage ethanol. In order for ethanol to be sold as fuel, a denaturing process occurs where hydrocarbons such

as gasoline are added in order to make it unfit for drinking [58]. Ethanol has a higher heat of evaporation, roughly twice the amount as that of gasoline, making it difficult for vaporization under cold temperatures. To ensure proper operation in cold temperatures, 15% of hydrocarbons are added, which is commonly found throughout America. Unlike gasoline, ethanol also contains a very narrow temperature range where it vaporizes. The blending of fuel ethanol is standardized through ASTM, following specific guidelines which take into consideration a variety of concerns such as geographical location and temperatures.

2.6.2 Ethanol fuels and engine wear

Researchers have debated that alcohol fuelled vehicles can contribute to a higher cylinder bore wear and that increased oil consumption results in a loss of performance [22, 60]. Marbach et al.[61] conducted several engine tests in order to study the wear rates of alcohol fuels and published that fuels such as neat methanol can result in an overall increase in engine wear during low temperature operations. When anhydrous ethanol and blends of fuel were tested, no apparent increase in engine wear was noticed. The use of alcohol fuels decreased the overall engine deposits on the cylinder walls in comparison to unleaded gasoline. In addition the accumulation of water was greater in the lubrications for alcohol fuelled engines in comparison to gasoline fuelled engines. Methanol fuelled engine wear was attributed to the formation of formic acid reacting with the iron cylinder to produce iron formate; this was not evidenced in ethanol fuelled engines. The authors concluded that further study was necessary in order to determine exactly the mechanism of engine wear with alcohol as a fuel.

Tung and Gao [22, 60] investigated the tribological properties of various piston ring coatings in a blend of energy-conserving oils and ethanol fuels. Wear tests were conducted on a high frequency reciprocating friction machine using a cast iron liner against piston rings coated with nitride stainless steel (NSS), chromium nitride (CrN), and diamond like coating (DLC). Fuel and engine oil were delivered through two pumps at a controlled rate in order to have a mixture roughly around 98% fuel and 2% oil. Friction development with running time data were compiled for a fully submerged lubrication condition using only engine oil as shown in Figure 2- 21. After a short period of *"breaking-in"*, a protective film is formed, and this stabilizes the friction and wear loss. Under the blended fuel -oil conditions the CrN and NSS coated rings never reach a stable coefficient of friction. Only DLC coated rings stabilize as shown in Figure 2- 22. The stabilizing of DLC coated rings can be attributed to the self lubricating properties in the carbon base boating. The authors also investigated the effects of different acidity in the fuels by conducting wear tests with two fuels of pH value of 4 and 6. It was concluded that the friction coefficient in the more acidic fuel (pH 4) was much higher than that in fuel which was more neutral (pH 6) possibly due to severe acidic corrosion. When a superficial film was detected, a drop in the COF occurred; however, the film was seen to destruct and then to replenish. Wear under the higher acidic fuel was observed to have severe metal-to-metal contact resulting in more wear. A starved lubricating condition with only E85 fuel as lubrication resulted in limited lubricity, and the more acidic fuel was seen to have less lubricity than the neutral fuel.

Hu et al. [14, 62] looked into the possible effects of residue alcohols, such as 2-ethylhexanol ($C_8H_{18}O$), which may be carried over from the manufacturing of ZDDP.

The authors reported, firstly, that in the presence of alcohol in ZDDP, the thermal decomposition temperature of ZDDP reduced from 215^{o}C to 150^{o}C. It was also found that when small amounts of alcohol were added to ZDDP (up to 5 wt.%), the load-carrying capacity of the oil with ZDDP increased; however, further addition of alcohol only decreased the values as shown in Figure 2- 23. This positive effect was also evidenced when the wear scar diameter initially decreased as alcohol was added to ZDDP; however, further addition of alcohol past 5 wt.% showed the wear scar to increase as shown in Figure 2- 24. The authors concluded that the hydroxyl group (-OH), which is a polar group in the alcohol, can easily adhere to the frictional surface to create a protective film, which in turn increases the wear resistance of the lubricating oil under lower load and at slower speeds. The alkyl group in the alcohol and ZDDP may also help create synergism between the two and formulate good boundary conditions for adhesion to the surface. The layer development can be attributed to the decrease in thermal stability of ZDDP, and in the course of temperature increase from friction, may lead to early decomposition species of ZDDP, precursors for film formation.

Hu and Lie [19] investigated the mechanism of alcohols for lubrication of aluminum by conducting wear tests on 2024Al against steel counterface, lubricated with liquid paraffin (C_nH_{2n+2}) containing alcohols. The paraffins included n-butanol, ethandiol, 1,3-butanediol, 1,4 butanediol, and propanetriol. The wear scar width, as a function of applied load for 3 wt.% addition of alcohol to base oil, was plotted and shown in Figure 2- 25. It is clear that different alcohols provide different antiwear abilities. With n-butanol, the system failed at a maximum load of 600 N, whereas with ethandiol, the failure load increased to 1000 N. Propanetriol showed to contain the best antiwear

ability by reaching failure load of 1600 N. The authors stated that based on Hotton's and Wan's bidentate bonding hypothesis, the antiwear and load-carrying capacities can be attributed to the alkyl chain length which form aluminum diol complexes. The diol complex variations can also influence the antiwear ability. For example, the 1,3-diol complex was shown to be more chemically stable than corresponding 1,4-diol or 2,3-diol, resulting in better antiwear behaviour. It was also found that when the hydroxyl group number increased, the molecular polarity improved, consequently forming a more stable chem-adsorbed film. Figure 2- 26 is a schematic diagram of a possible chemical film formation which acts as the primary mechanism for antiwear by alcohols.

Igari et al. [17] and Wan et al. [16] also found similar results when investigating the effect of molecular structure of diols as lubricants on the wear of aluminum alloys. The authors found that the amount of wear rapidly decreased when methyl groups were added to diol as shown in Figure 2- 27. The authors stated that the functional groups, such as OH groups, help adhere the molecule firmly to the surface to provide good lubrication. A schematic of the layer formation for 1,4 Butanediol, 1,2-Butanediol and 2,3-Butanediol is shown in Figure 2- 28. The latter two films show better wear protection due to a double layer instead of a single layer.

2.7 Summary

The previous chapter provided some of the necessary information regarding the alloy, the effect of changing certain test conditions such as load, atmosphere, lubrication, coatings and the behaviour of bio-fuels. The combined effects of load, lubrication, alloy composition, morphology, temperature, sliding speed and counterface relating to the tribological behaviour of an alloy can only be obtained though bench tests and

characterization. The following chapter will outline the setup, calculations and characterization techniques in order to understand the progression of wear on Al-12.6% Si alloy under boundary lubricated conditions.

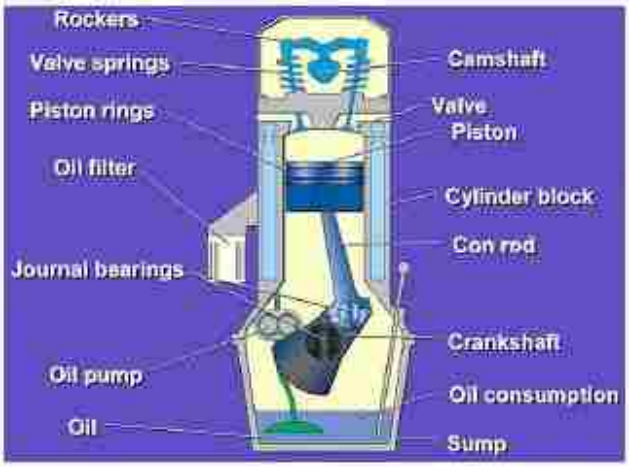

Figure 2- 1: Components typically found in an internal combustion (IC) engine. [1]

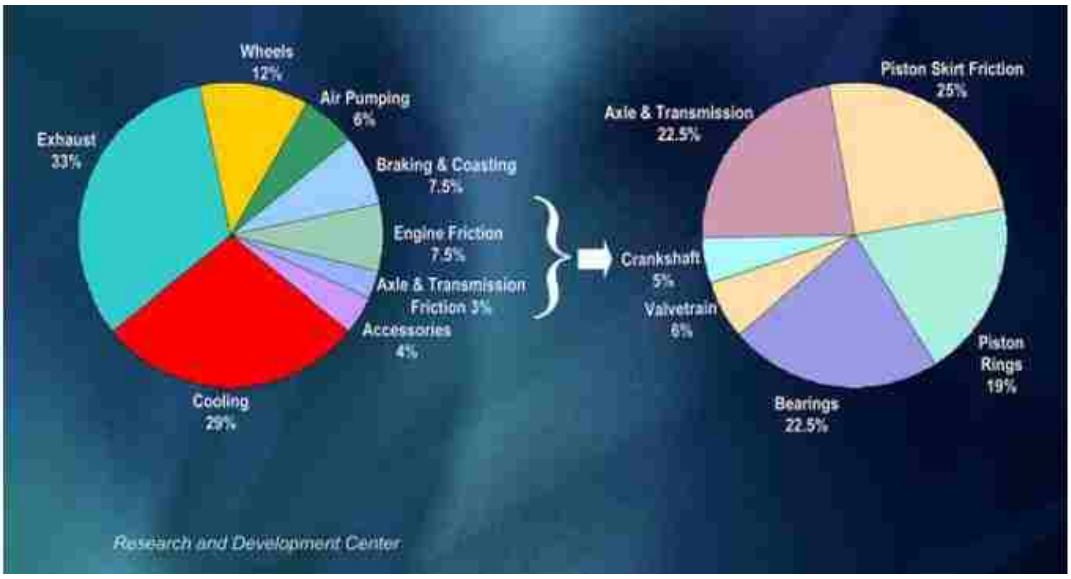

Figure 2- 2: Distribution of energy consumption in a light-duty vehicle. [1]

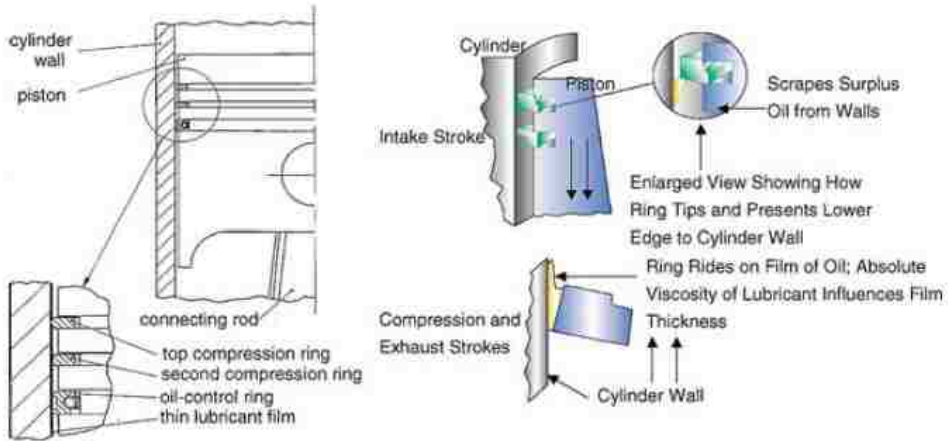

Figure 2- 3: Piston assembly and piston ring function from an internal combustion engine. [1]

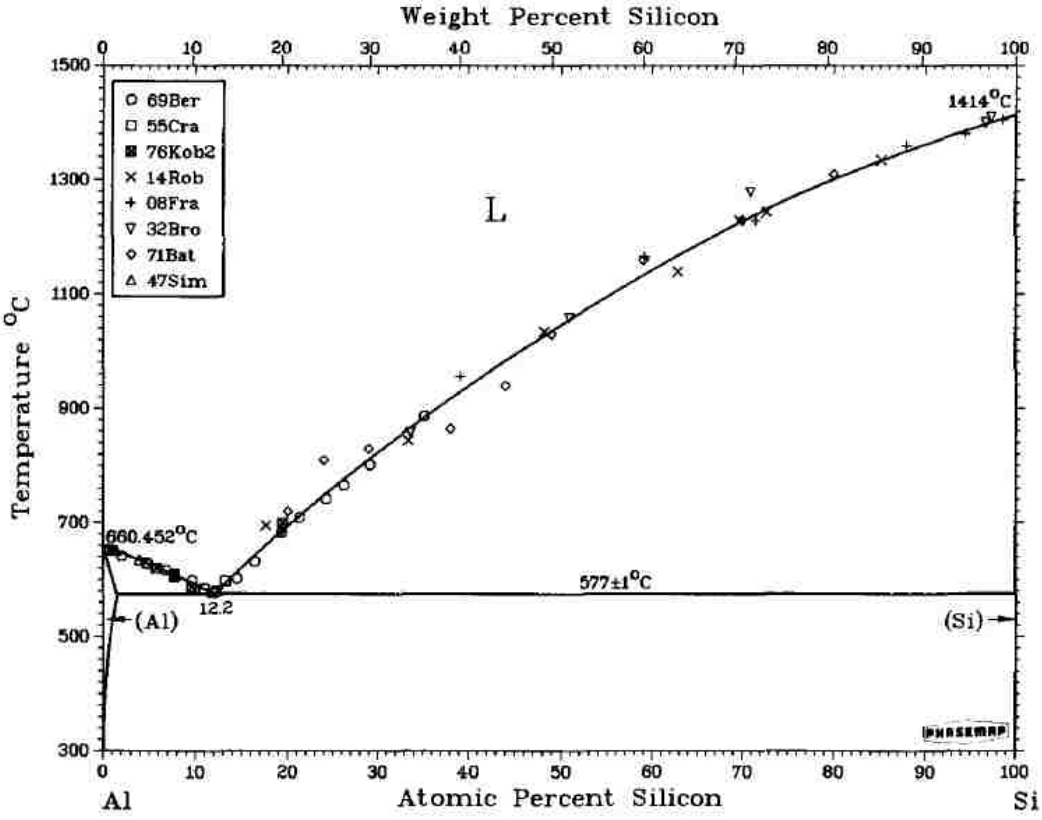

Figure 2- 4: Phase diagram for Al-Si alloys. [29]

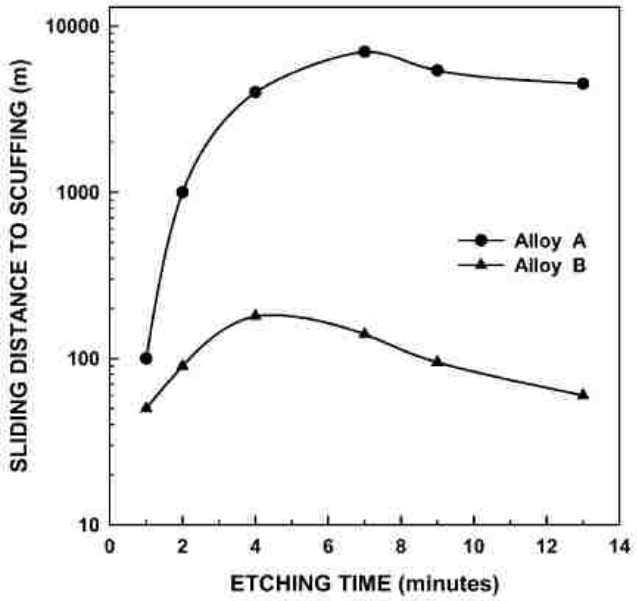

Figure 2- 5: Effects of etching time on the sliding distance to scuffing in Alloy A and B. The best condition for scuffing resistance was achieved between 5-7 minutes. Prolonged sliding past 7 minutes resulted in weakening of silicon particles/matrix bonding due to excessive dissolution of matrix. [30]

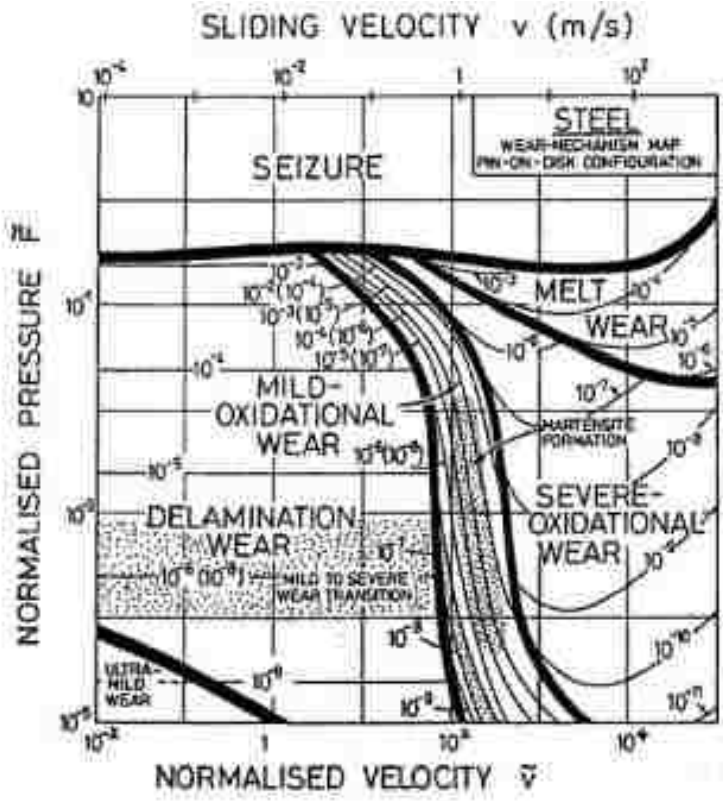

Figure 2- 6: Wear map for steel-on-steel during dry sliding. [34]

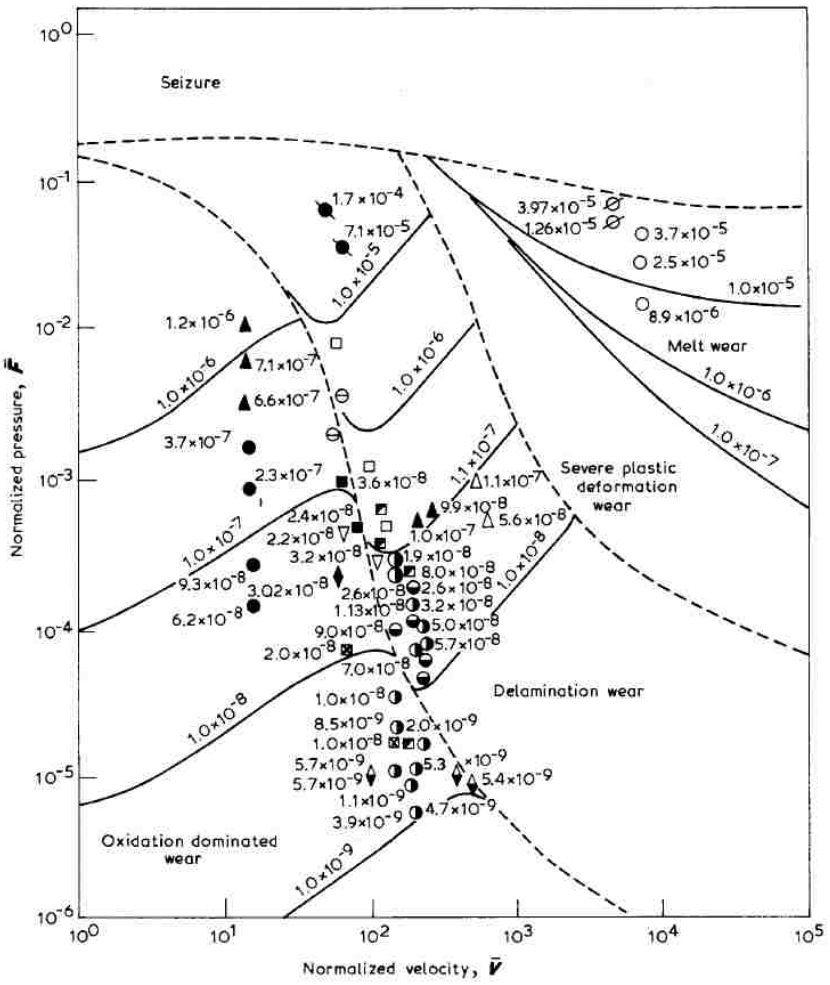

Figure 2- 7: Wear map of aluminum alloy outlining the boundaries for each wear mechanism. [35]

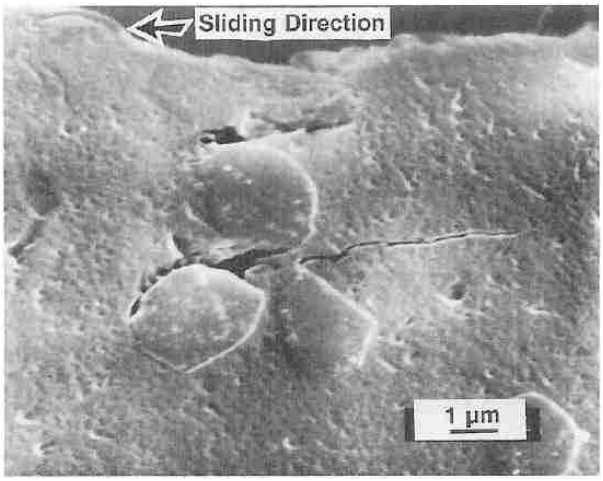

Figure 2- 8: Void and crack nucleation around the silicon particles under the contact surface. [36]

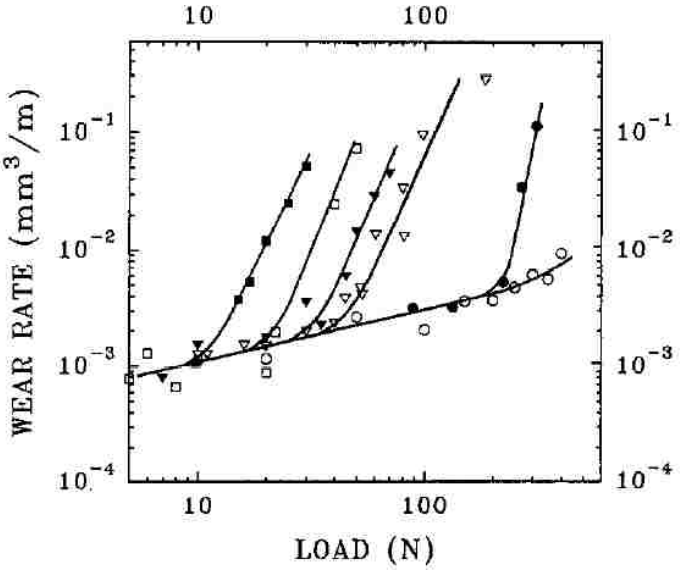

Figure 2- 9: Wear rate versus applied loads at different sliding velocities for Al 6061 alloy: (○) 0.2 m s $^{-1}$ (●)0.4 m s $^{-1}$ (▽)0.8 m s $^{-1}$ (▼)1.2 m s $^{-1}$ (□)2.0 m s $^{-1}$ (■)5.0 m s $^{-1}$. [37]

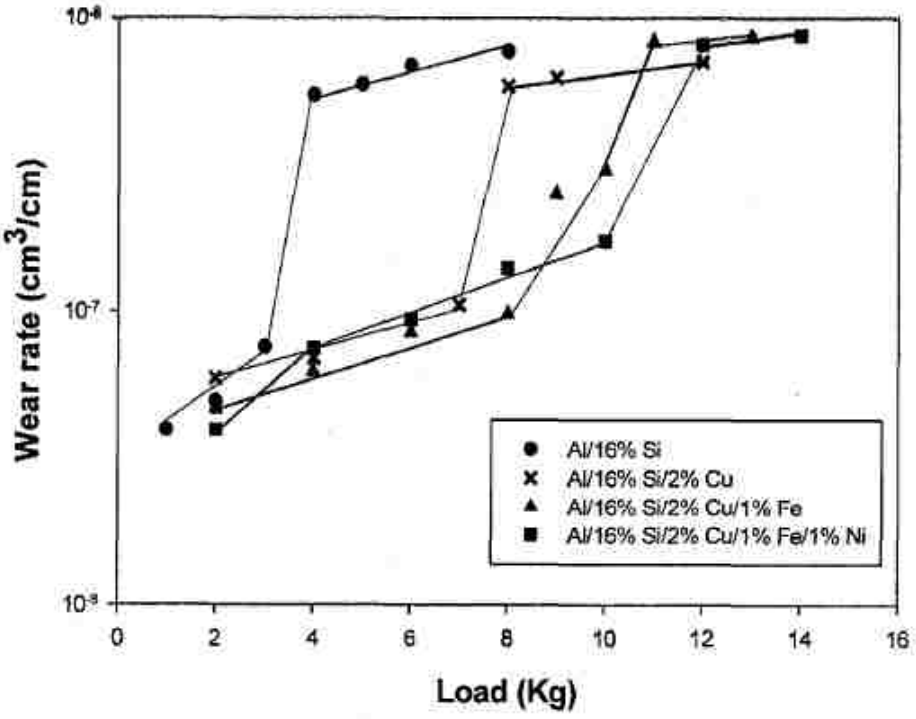

Figure 2- 10: Wear rate versus load for four Al-Si alloy systems. [38]

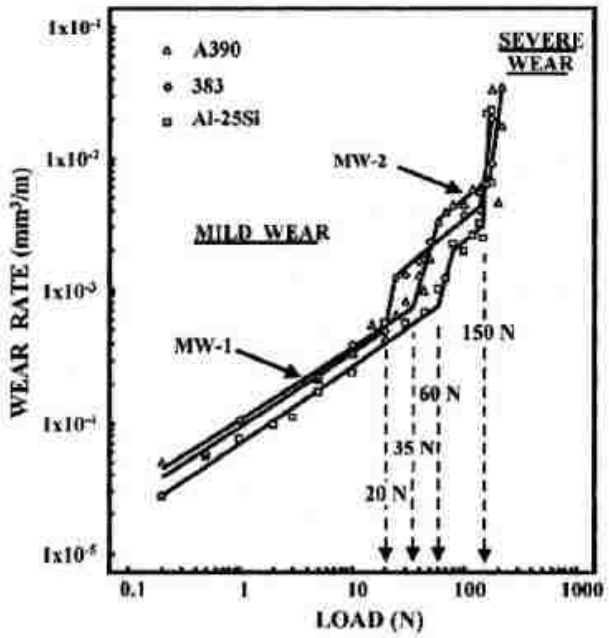

Figure 2- 11: Wear rates on Al-Si alloy under various loads in a controlled environment. [41]

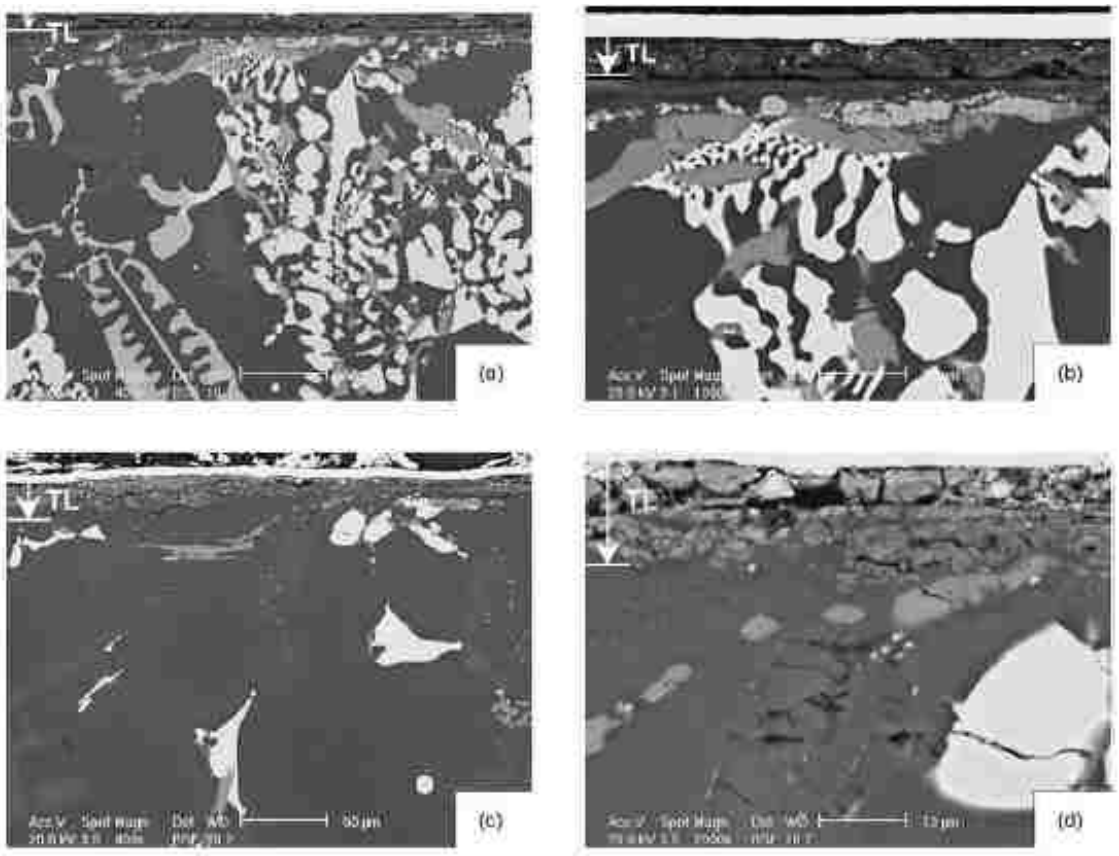

Figure 2- 12: SEM-BSE images of the tribolayer morphology: Wear in argon (a) and (b); wear in air (c) and (d). [43]

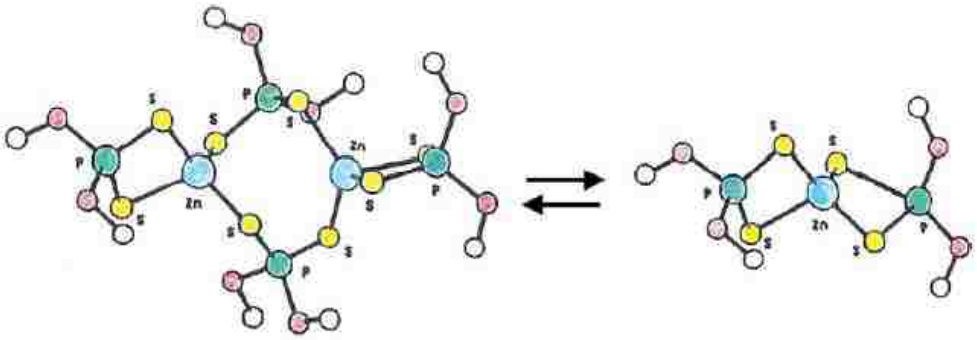

Figure 2- 13: Equilibrium between dimeric and monomeric ZDDP forms. [48]

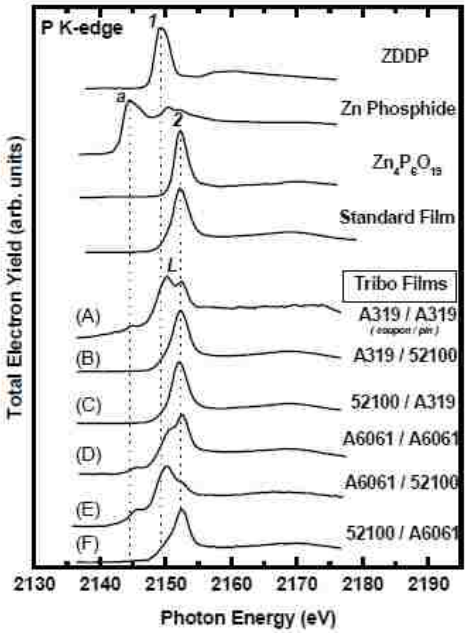

Figure 2- 14: The P K-edge spectra of model compounds, the standard film and those obtained from the wear scars of the systems listed. [9]

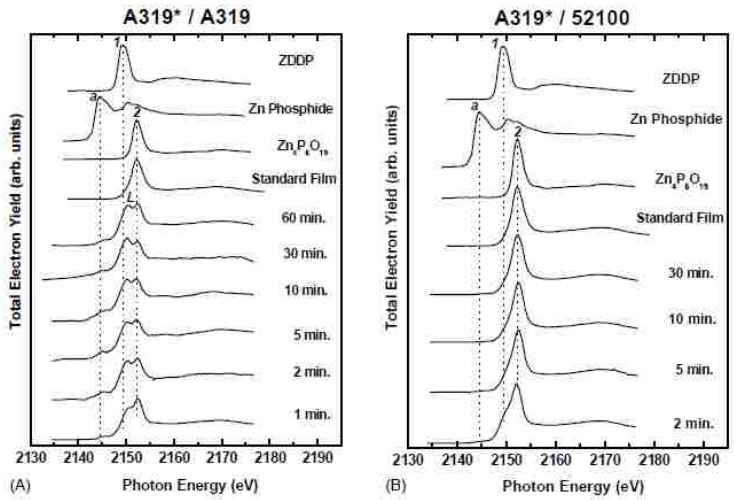

Figure 2- 15: Formation of antiwear film as a function of time on aluminum and steel system using ZDDP additives. [9]

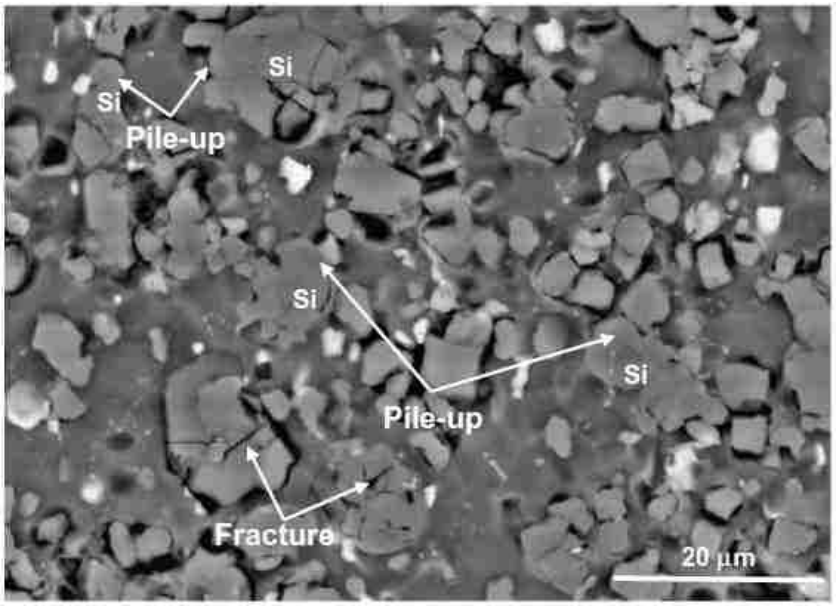

Figure 2- 16: Back scattered SEM image at 1.0 N of the worn surface of Al-25% Si after sliding for 5x 10^4 cycles. Silicon particles fracture and sink-into the matrix forming pile-up. [4]

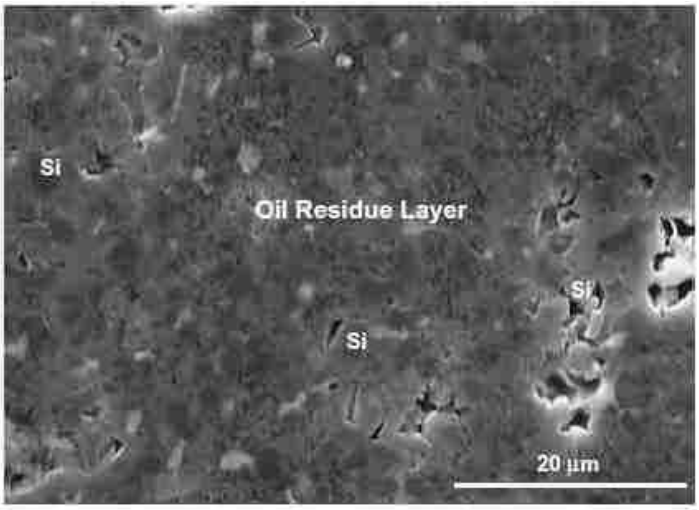

Figure 2- 17: Secondary SEM image at 2 N load on the worn surface of Al-25% Si after sliding for 6 x 10^5 cycles. The formation of a solid tribolayer occurred consisting of an oil residue layer rich in C, Ca, S, Zn and Aluminum oxide. [4]

Figure 2- 18: A surface profile where surface height y, relative to the mean line plotted against the distance. [56]

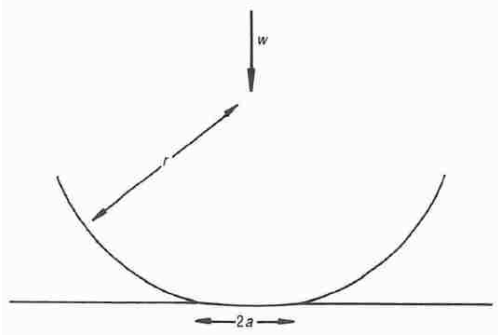

Figure 2- 19: Elastic deformation of a sphere of radius r, pressed against a plant surface under load W. Radius of the contact circle is a. [56]

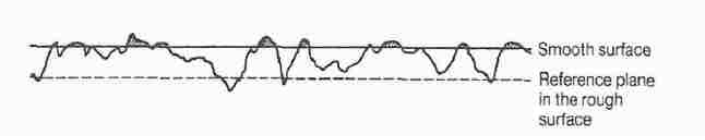

Figure 2- 20: Model for contact between a rough surface and a smooth rigid plane. [56]

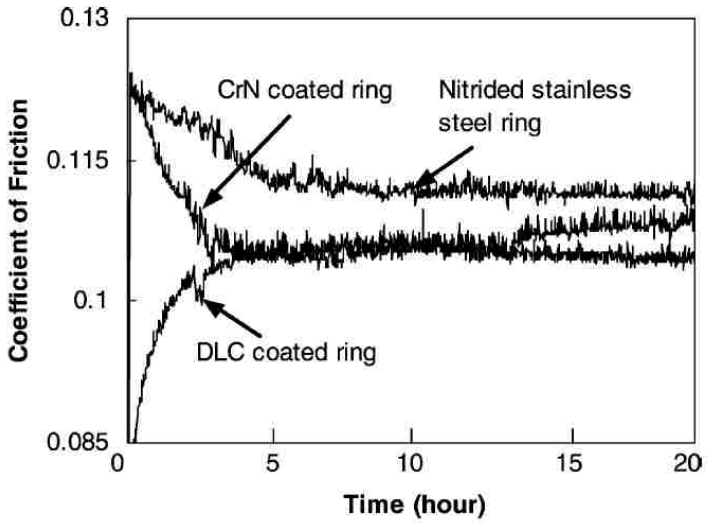

Figure 2- 21: Variation of friction coefficient for ring coatings sliding against cast iron liners in 5W30 mineral oil at 80N and 125 C. [12]

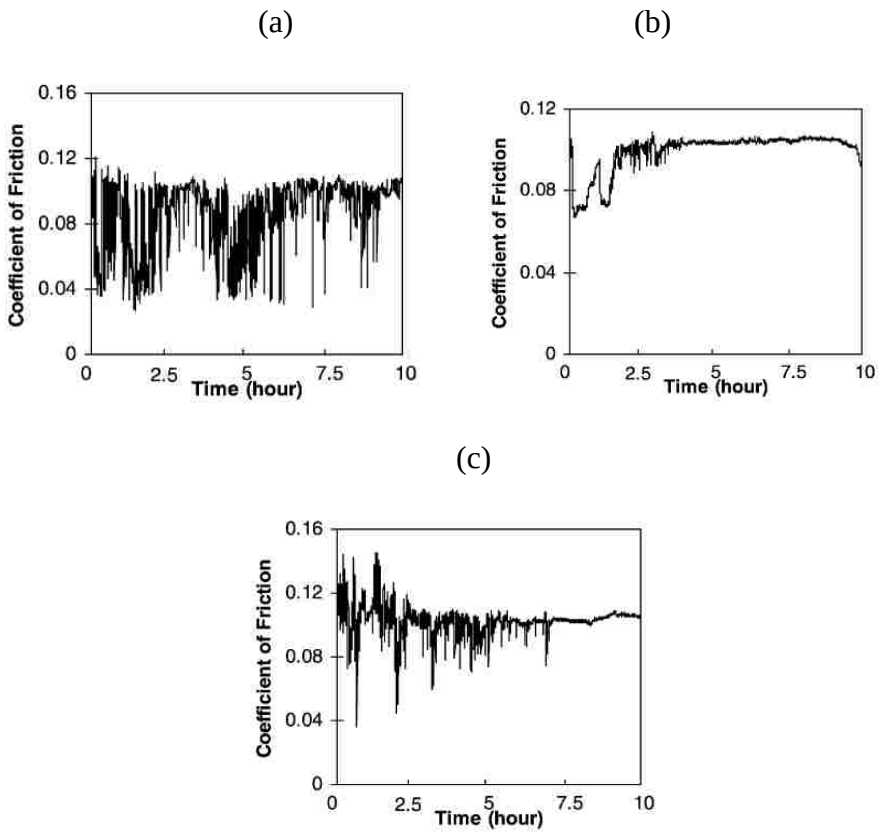

Figure 2- 22: Friction curves for ring coatings run against cast iron liner segments in a blend of E85 fuel and 5W30 engine oil. (a) NSS. (b) DLC coated. (c) CrN. [12]

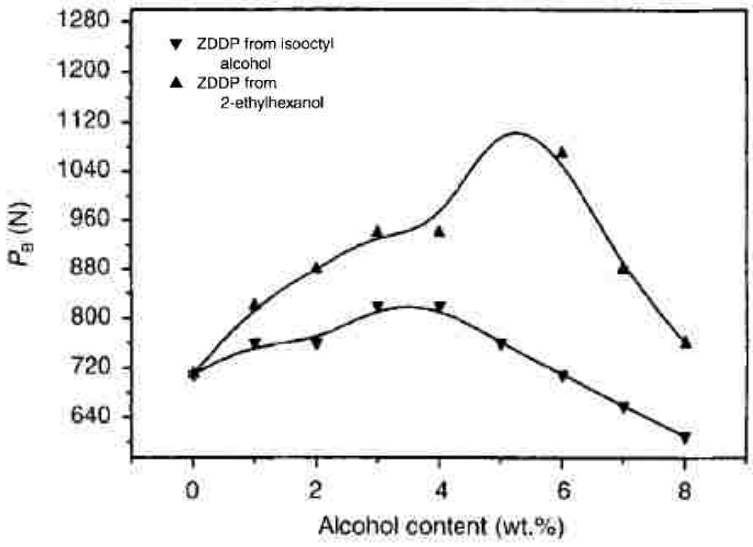

Figure 2- 23: Effects of alcohol content on the load-carrying capacity of ZDDP. [14]

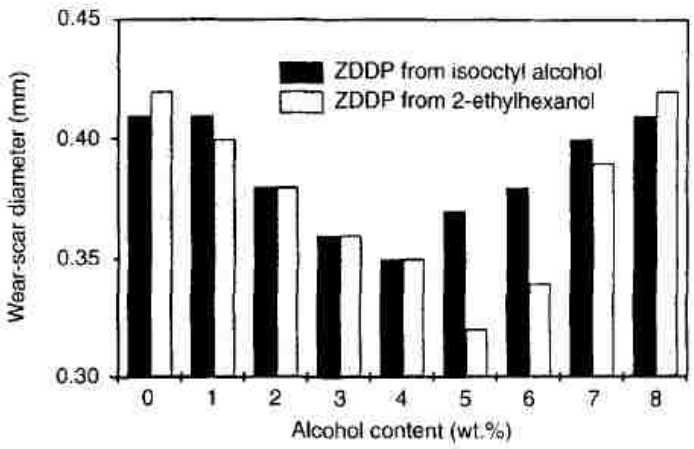

Figure 2- 24: Wear scar diameter of ZDDP for various alcohol contents. [14]

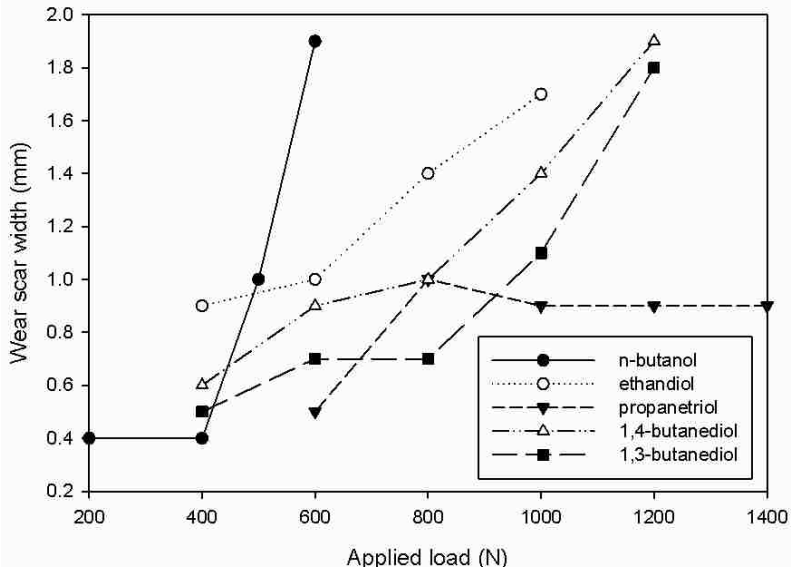

Figure 2- 25: Wear scar width of aluminum block as a function of applied load with the lubrication of base oil containing 3 wt.% alcohols. [18-19]

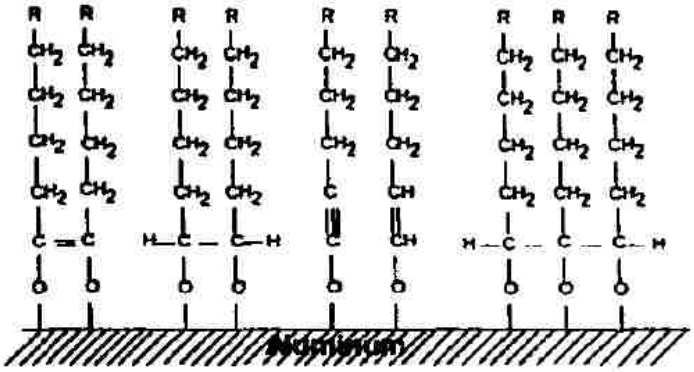

Figure 2- 26: The schematic diagram of alcohols chem.-adsorption and interaction with aluminum during friction process. [18]

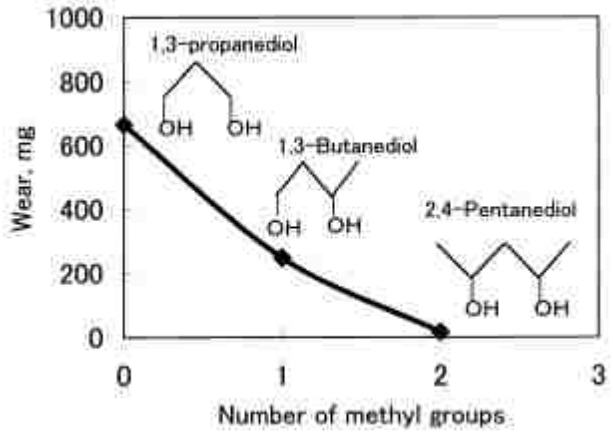

Figure 2- 27: Wear as a function of the number of methyl groups added to 1,3-propanediol. [17]

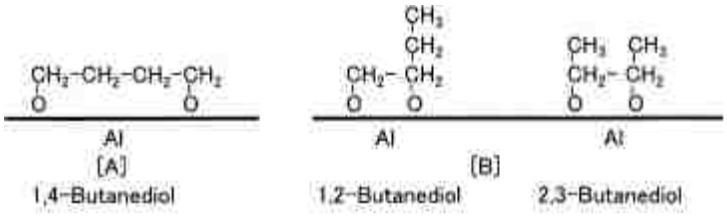

Figure 2- 28: The antiwear layer formation on friction surfaces. [17]

CHAPTER III MATERIALS AND EXPERIMENTAL PROCEDURES

3.1 Introduction

This chapter outlines all the information regarding the materials used for testing and the procedures used in order to study the alloy in the UMW regime. **Section 3.2** describes the alloy used for the experiments. **Section 3.3** describes the microstructure of the specific alloy followed by a description of the procedure for the sample surface preparation in **section 3.4**. Information of the surface morphology has been given in **section 3.5**, followed by a description of the testing equipment and parameters used for testing in **section 3.6**. **Section 3.7** describes the properties of the counterface material used during testing. **Section 3.8** describes the calculation for determining the lubrication regime, followed by an outline for quantifying the amount of volume loss after each wear tests in **section 3.9**. The final **section 3.10** of this chapter describes the equipment used in order to characterize the worn surfaces.

3.2 Eutectic Al-Si alloy

The alloy used in this research was a eutectic Al-Si alloy with 12.6% silicon content, and was cut from a sand casted block. The sample was then subjected to a heat treatment (T-7) consisting of a solution treatment at 490^{o}C for 6 hours, then a quench in forced air to less than 90^{o}C, cooling at between 80 and 100^{o}C/min, and followed by aging at 240^{o}C for 4 hours. The samples were provided by General Motors Research and Development Centre located in Warren, Michigan, USA. XPS analysis was conducted to determine the exact chemical composition and can be found in Table 3- 1. The hardness of the alloy was determined using a Brinell hardness tester (Buehler Micromet II- Model

1600-9000) and was measured to be 93.0 ± 1.0 using a tungsten carbide indenter at 500 Kg load [6]. The matrix hardness was measured at 1.65 ± 0.05 GPa using a Berkovich indenter at room temperature.

3.3 Microstructure of the Al-Si alloy tested

Samples for microstructure observations were prepared by conventional mechanical grinding and polishing techniques. The samples were wet ground using 180, 240, 400, 600, 1200 and 2400 SiC emery paper successively. After the grinding process, samples were polished using 3, 1, and 0.1 μm diamond suspensions. Samples were then etched using 10% NaOH for 5 seconds to reveal the microstructure. Quantitative microstructual measurements were conducted to measure the silicon particle length and width. An scanning electron microscopy (SEM) image representing an average area from the surface of the sample was used in order to quantify the morphology of the cast as shown in Figure 3- 1. The particle length was determined by measuring the distance parallel to the longest side; whereas, the width was determined by measuring perpendicular to the length of the particle. Histograms were generated to represent particle length and width with respect to the frequency of occurrence as shown in Figure 3- 2. Average silicon particle length, measured from 200 particles, was measured to be 21.11 ± 17.59 μm, whereas average particle width was measured to be 4.33 ± 2.88 μm. The aspect ratio, which is defined as the average particle length over the average particle width, was determined to be 4.9. The area density, defined as the total area, of silicon particles over the entire area was calculated to be 0.3.

3.4 Sample surface preparation for testing

The samples were mechanically wet ground using 180, 240, 400, 600, 1200, and 2400 SiC emery paper successively. Following the grinding procedure, the samples were polished using 3, 1 and 0.1μm diamond suspensions. In order to accurately model the surface of the linerless engine, the surface is chemically etching using a 10% NaOH solution for roughly 180 seconds based on the procedure outlined by Riahi et al. [30]. The etching process allows the aluminum matrix to dissolve while leaving the silicon particles elevated above the matrix level. Excess or early etching resulted in a decrease in the scuffing resistance of the alloy. After the etching procedure, the samples were ultrasonically cleaned in ethanol for 60 seconds to remove any debris.

3.5 Surface morphology

The surface of the sample was analyzed using a 3D white light optical profilometer (WYKO NT-1100), working in the vertical scanning interferometer (VSI) mode. The resultant surface scan data is statistically analyzed by creating a histogram of the number of points which were detected for each corresponding height. The unfitted histogram data can be deconvoluted to create two Gaussian curves to represent the aluminum matrix height and silicon particle height, as shown in Figure 3- 3, representing an etched surface before testing. The histogram data shows two distinctive peaks; the first peak represents the aluminum matrix level, and the second peak represents the exposed silicon particles.

3.6 Tribometer

Sliding wear tests were conducted on a pin-on-disc type wear tester (CSM tribometer, Switzerland). The samples were securely fixed at the centre to the sample

holder. The sample holder was then secured to the test cup. A lid was screwed on in order to prevent any overflow of lubrication during testing. The sample was initially flooded with lubricant before each test. A peristaltic pump was used to constantly deliver lubrication to the testing surface through a thin hose at a controlled rate of 0.04 ml/min as shown in Figure 3- 4. The wear track diameter, sliding speed and load were all fixed at 3 mm, 5 cm/s, and 2 N, respectively. The number of sliding cycles was changed respectively to understand the progression of wear. The temperature of the test environment was constant at room temperature. The summary of the testing parameters is listed in Table 3- 2.

3.7 Counterface material

The counterface material chosen for this research was a 6 mm diameter AISI 5200 grade steel ball. The chemical composition can be found in Table 3- 3. Before each test, the balls were secured inside the ball holder and polished using a 1μm diamond suspension and then cleaned ultrasonically using acetone for 60 seconds. The ball holder was rotated evenly in a circular motion during polishing in order to avoid flattening. Shown in Figure 3- 5 is a WYKO image obtained after polishing of the counterface ball.

3.8 Lubrication condition

To determine the lubrication regime for the sliding wear tests, the ratio of *(λ)* minimum lubrication thickness *(h_{min})* over the *r.m.s* surface roughness *(r*)* of the contacting bodies was calculated based on the following equation respectively [5]:

$$h_{min} = 1.79R^{0.47}\alpha^{0.49}\eta_o^{0.68}U^{0.68}(E^*)^{-0.12}W^{-0.07} \quad (3.1)$$

$$r^* = \sqrt{r_{particle}{}^2 + r_{ball}{}^2} \quad (3.2)$$

Where *R* is the radius of the counterface ball, *U* is the sliding speed, *W* is the normal load applied, and α and η_o represent the viscosity properties of the lubricating fluid. The constant α is a relationship dependent on the viscosity constant η_o estimated from the relationship:

$$\alpha \approx (0.6 + 0.965 \log_{10} \eta_o) \times 10^{-8} \quad (3.3)$$

To calculate the composite elastic modulus *(E*)* of the contacting body, the following equation is then used:

$$\frac{1}{E*} = \left[\frac{[1-(v_{Al-Si})^2}{E_{Al-Si}} + \frac{[1-(v_{steel})^2]}{E_{steel}}\right] \quad (3.4)$$

where $E_{Al\text{-}Si}$ is the elastic modulus of Al-Si and is calculated using:

$$E_{Al-si} = E_{Si} w_{Si} + E_{Al}(1 - w_{Si}) \quad (3.5)$$

where w_{Si} is the weight fraction of the silicon phase in the alloy, and $v_{Al\text{-}Si}$ is the Poisson's ratio of Al-Si which is calculated using:

$$v_{Al-Si} = v_{Si} w_{Si} + v_{Al}(1 - w_{Si}) \quad (3.6)$$

$r_{particle}$ and r_{ball} are the r.m.s roughness of the silicon particles and the steel ball.

Table 3- 4 and Table 3- 5 show the values used for the calculation of r^* and h_{min} for just ethanol and synthetic Mobile 1 engine oil (5W30) at 25^{o}C respectively. In order to determine the viscosity parameters for the blended condition, the Refutas method [63] can be employed to calculate the viscosity blending index *(VBI)* for each fluid by the following equation:

$$VBI = 14.534xln[\ln(\nu + 0.8)] + 10.975 \quad (3.7)$$

Where ν is the kinematic viscosity measured in centistokes (cSt). Based on the two blended fluids, the *VBN* number of the blend can be estimated using the following equation:

$$VBN_{Blend} = [X_A VBN_A] + [X_B VBN_B] \quad (3.8)$$

Where *X* is the mass fraction of each component in the blend. The final step is to determine the kinematic viscosity of the blend by the following equation:

$$v = \exp\left(\exp\left(\frac{VBN_{Blend} - 10.975}{14.534}\right)\right) - 0.8 \quad (3.9)$$

Based on the above calculation, the kinematic viscosity of the blended fluid was estimated to be 6.59 cSt. This value was then used to calculate the h_{min} of the blended fluids as shown in Table 3- 6. The ratio of h_{min} over r^* for just ethanol, 5W30 and the blend of 5W30/E85 was determined to be 0.012, 0.27 and 0.043 respectively. Because the ratio was below 1 for all cases, it can be concluded that boundary lubrication regime was achieved at the start of each test.

3.9 Quantitative measurement of volumetric wear loss

The material removed from the surface was quantified based on optical interference method instead of conventional electronic balance because the amount of material removed was too small to be detected. The optical interference method involves obtaining eight optical profilometry images around the wear track after each sample has been washed with hexane as illustrated in the schematic shown in Figure 3- 6. It has been shown that the pressure needed to initiate indentation of the silicon particle is roughly 2.89 times greater than the yield strength of the aluminum matrix [5-6, 49]. Since

embedding of the silicon particle is evident, it can be suggested that the exerted pressure on top of silicon particles exceeds the minimum pressure. Embedding silicon particles displace the matrix adjacent to the particles causing the formation of pileup. Continuation of sliding contact results in a transition point where the embedding silicon particles and the aluminum reach the same height (UMW II), exposing the matrix to the counterface. The counterface at this point begins to deform the surface and can be characterized by the formation of long grooves and scratches as the counterface ploughs the surface. This is illustrated in Figure 3- 7 (a) with a 2-D surface profile of the wear track at 10^6 sliding cycles with only 5W30 lubrication. This image illustrates a typical wear track showing the location of Si particles and the aluminum ridges (R) along the profile line A-A'. Shown in Figure 3- 7 (b) is the corresponding 3-D optical profilometry image of the area indicating the location of the profile line A-A' along with the Si particles and the aluminum ridges (R). The area indicated by the gray region is the material which would ideally be located between the grooves which can then be quantified as the material which has been removed. In order to quantify the amount of material removed, it is first necessary to determine a reference level in order to calculate the area. The reference level can be determined by observing the height distribution data, which is a statistical average of the number of points corresponding to the surface elevation along the entire area. The unfitted data can be evaluated by fitting Gaussian peaks as shown in Figure 3- 7 (c), as an example showing a section of the wear track at 10^6 sliding cycles with 5W30 lubrication fitted with three Gaussian peaks. The first peak represents the deepest points inside the wear track, followed by the unaffected matrix level. The third peak represents the piled up aluminum or reduced height of the silicon

particles adjacent to the wear track. The reference level is considered as the average highest points of the grooves inside the wear track, ideally located between the base matrix level and the reduced silicon particle height. This can be determined using the optical profilometry image analysis software (Vision 3.43). The error associated with locating the reference level was calculated by quantifying the volume loss based on the reference level located at the piled-up aluminum height and then quantifying the volume loss based on the reference level at the base matrix height. The change in the quantified volume was within ± 4% for each measurement. The area which falls below the reference level can be deemed as damage to the matrix. The unaffected areas to the left and right of the wear track was eliminated in order to minimize measurement errors. The advantage of employing such method increases the repeatability and reduces any operator induced errors. To calculate the total volumetric wear loss, the following equation was employed where the averaged area which is determined as the amount of material removed multiplied by the circumference of the wear track:

$$V = 2\pi R_w A_t \tag{3.10}$$

Where R_w represents the radius of the wear track (1.5mm) and A_t represents the average area of the 24 measurements. From each of the eight images, a total of three measurements are used in order to represent the overall wear track. Refer to Appendix A for calculations.

3.10 Worn surface characterization

The characterization of the worn surface included a number of techniques and equipment. The features on the surface of the wear track were observed using a scanning

electron microscope (JEOL 5800/EDAX) equipped with an energy dispersive spectroscopy (EDS). An optical microscope (Keyence VHK 600K) was also employed to observe the surface features of the wear track. In order to characterize the chemical composition of the wear track, a multi-functional X-ray photoelectron spectrometer (XPS- PHI-5702) was employed using a pass energy of 29.35 eV, an excitation source of Mg-Kα radiation (hv = 1253.6 eV), and a take-off angle of 35^{o}. The chamber pressure was held constant at $3x10^{-8}$ Torr. The binding energy of contaminated carbon (C1s: 284.8 eV) was used as a basis of reference.

Samples for FIB were prepared using the H-bar method, where a thin plate incorporating a section of the wear track was cut by a diamond saw with dimensions of 15 mm long, 1.5 mm wide and 5.5mm. The plate is then polished using SiC abrasive paper until the thickness of 30 μm is achieved. The sample is then cut to a semicircular geometry with a 1.5 mm radius as shown in Figure 3- 8. The sample is than thinned to the appropriate thickness using FIB milling by removing material from each parallel side of the sample. TEM observations were performed using a Philips EM 430 analytical TEM equipped with an Optical/AAT windowless X-ray energy dispersive spectrometer (EDS) operated at 300 kV. High resolution TEM and weak beam electron diffraction investigations were conducted using JOEL JEM-2100F field emission electron microscope. FTIR analysis was analysed in reflectance mode using a Continuum infrared microscope fitted with a Reflachromat (TM) 15X objective. Spot size of 100 microns x 100 microns were examined from both inside and outside the wear track, and each spectrum was collected by signal averaging one hundred spectra. Penetration depth varies based on the order of the wavelength, ranging from 2.5 to 25 μm [64].

% Si	% Cu	% FE	% Mn	% Mg	% Ni	% Ti	% Si	Bal.
12.6	0.87	0.37	0.79	0.26	1	0.11	0.02	Al

Table 3- 1: Chemical composition in wt. % of the GM-396 Al-Si alloy used in research.

Test Parameters	
Load:	2 N
Sliding Speed:	5 cm/s
Temperature:	24 °C
Lubrication:	Engine oil 5W30
	Engine oil/fuel mixture (E58/5W30) mixture at a 1:1 ratio
	Ethanol
Counterface:	52100 steel ball (6 mm)

Table 3- 2: Summary of the testing parameters.

% C	% Mn	% Si	% Cr	Bal.
0.98-1.1	0.25-0.45	0.15-0.30	1.30-1.60	Fe

Table 3- 3: Counterface material chemical composition.

R (m)	$\eta_{o\ (cSt)}$	α	U (m/s)	$r_{particles}$ (μm)	R_{ball} (μm)	E_{Al} (GPa)	E_{Si} (GPa)
0.003	1.54	7.81E-09	0.05	0.01	0.086	70	107
E_{Steel} (GPa)	w_{si}	V_{steel}	$E_{Al\text{-}Si}$ (GPa)	$\nu_{Al\text{-}Si}$	E* (GPa)	r* (μm)	h_{min} (μm)
210	0.12	0.33	74.4	0.33	61.8	0.08	0.001

Table 3- 4: Parameters used to estimate the film thickness (h_{min}) and r* for just ethanol.

R (m)	$\eta_{o\ (cSt)}$	α	U (m/s)	$r_{particles}$ (μm)	R_{ball} (μm)	E_{Al} (GPa)	E_{Si} (GPa)
0.003	65	2.35E-08	0.05	0.01	0.086	70	107
E_{Steel} (GPa)	w_{si}	V_{steel}	$E_{Al\text{-}Si}$ (GPa)	$\nu_{Al\text{-}Si}$	E* (GPa)	r* (μm)	h_{min} (μm)
210	0.12	0.33	74.4	0.33	61.8	0.08	0.023

Table 3- 5: Parameters used to estimate the film thickness (h_{min}) and r* for synthetic 5W30 engine oil.

R (m)	$\eta_{o\ (cSt)}$	α	U (m/s)	$r_{particles}$ (μm)	R_{ball} (μm)	E_{Al} (GPa)	E_{Si} (GPa)
0.003	0.59	3.90E-09	0.05	0.01	0.086	70	107
E_{Steel} (GPa)	w_{si}	V_{steel}	E_{Al-Si} (GPa)	ν_{Al-Si}	E* (GPa)	r* (μm)	h_{min} (μm)
210	0.12	0.33	74.4	0.33	61.8	0.08	0.037

Table 3- 6: Parameters used to estimate the film thickness (h_{min}) and r* for blend of 5W30/E85.

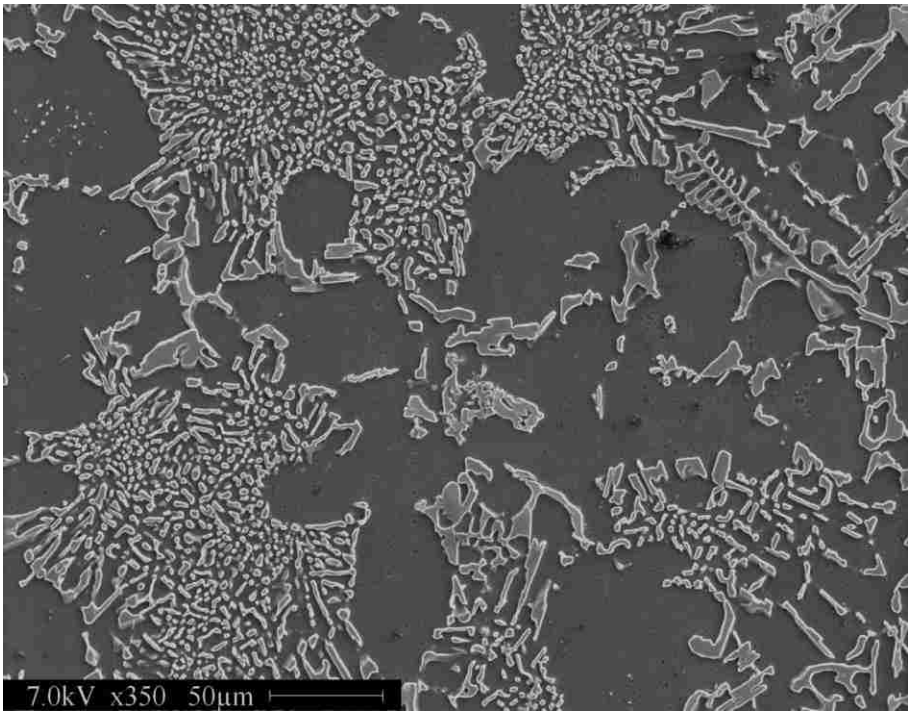

Figure 3- 1: Secondary electron micrograph of a typical microstructure of the Al-12.6% Si.

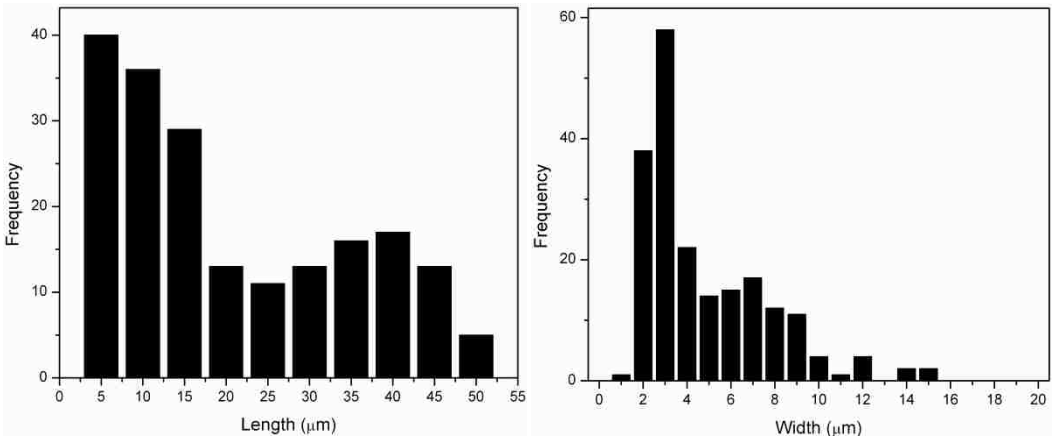

Figure 3- 2: Histogram showing the particle length and width distribution for Al-12.6% Si.

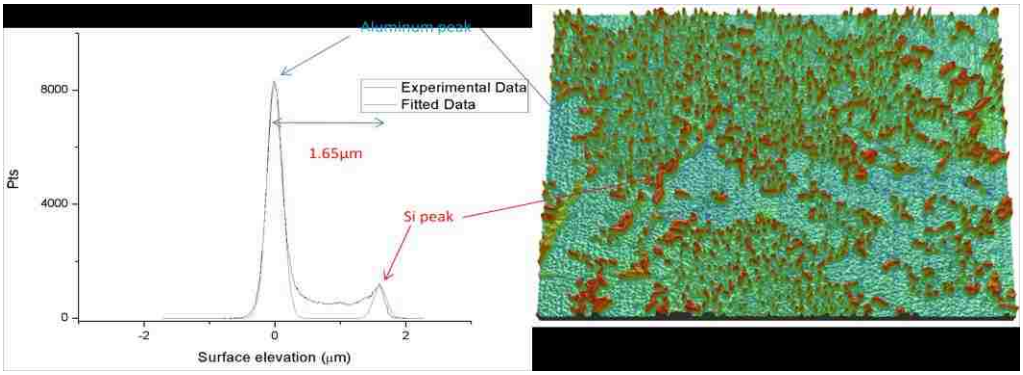

Figure 3- 3: 3-D optical surface profile of the etched surface of Al-12.6% Si. The first peak represents the aluminum surface while the second peak represents the exposed silicon particles.

Figure 3- 4: Setup used for pin on disk wear tests.

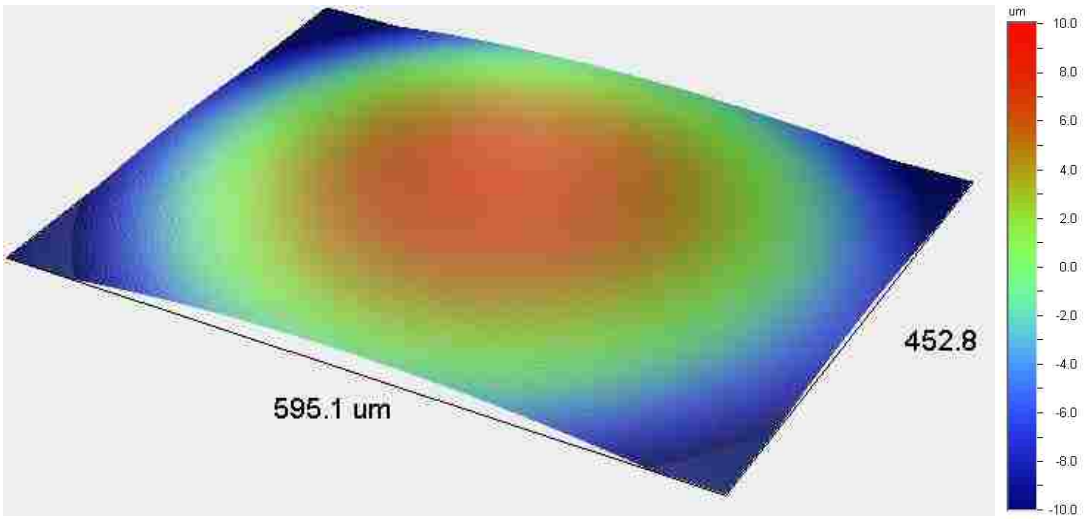

Figure 3- 5: WYKO image of the surface of counterface ball after polishing with 1 µm diamond suspension.

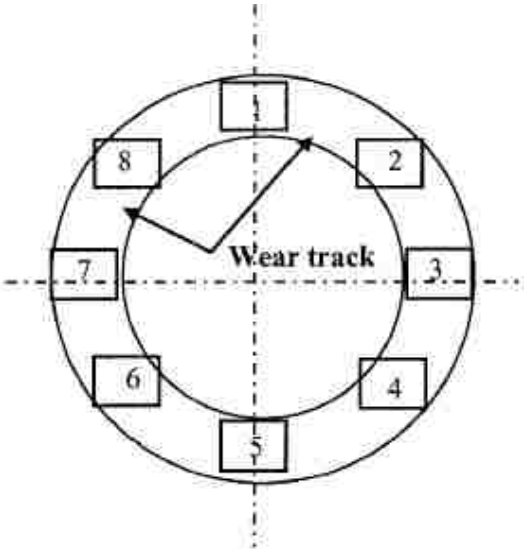

Figure 3- 6: Schematic drawing of the wear track where eight images are obtained along the wear track for calculation of volumetric wear loss.

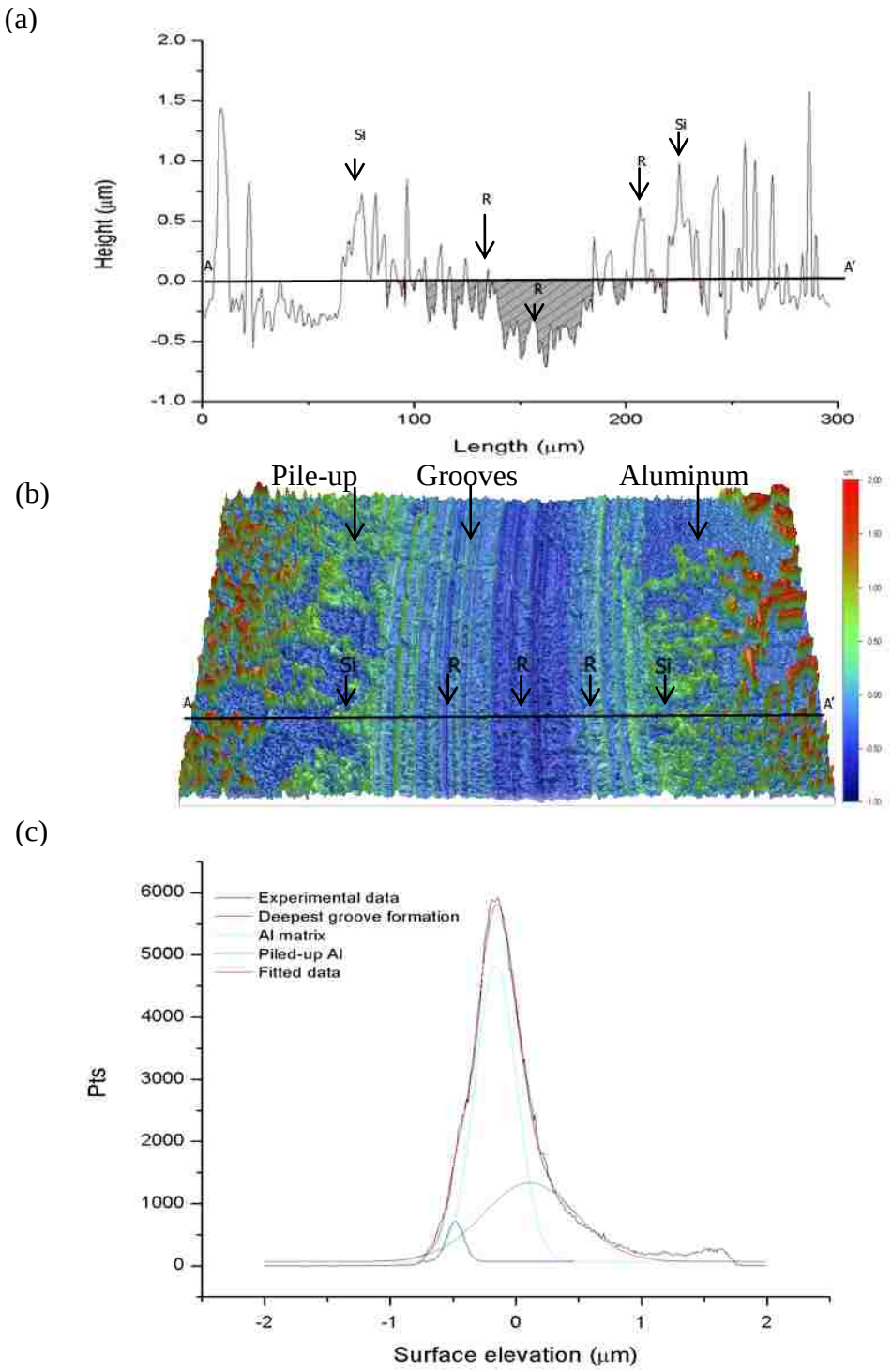

Figure 3- 7: (a) Cross-sectional profile line along A-A' showing the area considered to be damage due to wear by the formation of groves at 10^6 sliding cycles with 5W30 lubrication. Matching locations of Si particles and aluminum ridges (R). (b) 3-D surface profilometry image at 10^6 sliding cycles with 5W30 lubrication, showing the location of line profile indicated by A-A' and the location of Si particles and aluminum ridges (R). (c) Corresponding height histogram of the surface after wear test at 10^6 sliding cycles with 5W30 lubrication.

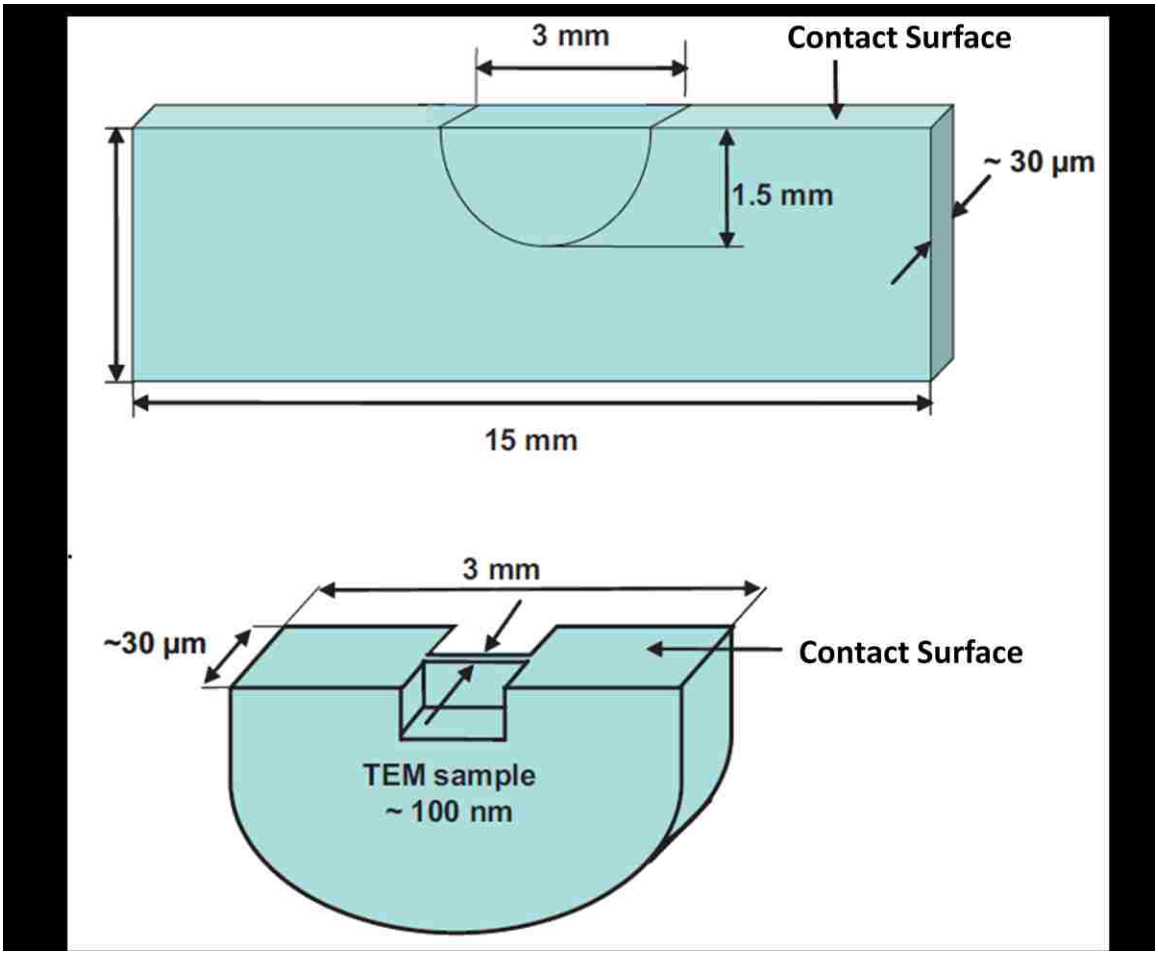

Figure 3- 8: Schematic of H-bar cross section technique used in order to prepare TEM samples. [8]

CHAPTER IV RESULTS AND OBSERVATIONS

4.1 Introduction

For the experiments described in Chapter 3, the progression of wear in the ultra mild wear (UMW) regime has been characterized through a combination of optical profilometry and scanning electron microscopy in this chapter. The chemical analysis of the tribolayer has been characterized through a combination of EDS, XPS, and FTIR analysis. The development of boundary lubricated wear with only 5W30 lubrication will be presented in **section 4.2**, followed by the development of wear under boundary lubrication with a mixture of E85 fuel plus 5W30 engine oil in **section 4.3**. The chemical characterization through XPS is presented in s**ection 4.4**. Subsurface damage characterization will be presented in **section 4.5**, followed by FTIR analysis in **section 4.6**. **Section 4.7** characterizes the wear with only ethanol as lubrication. **Section 4.8** discusses the coefficient of friction data correlated to the surface roughness of the wear tracks.

4.2 5W30

4.2.1 Volume loss with sliding cycles

Figure 4- 1 shows the volume loss of Al- 12.6% Si with sliding cycles under a 2N load under boundary lubrication with 5W30 engine oil at room temperature. Three stages of ultra mild wear (UMW) were identified. UMW I exists from 10^3 sliding cycles until 10^4 sliding cycles. No volume loss was detected. Transition to UMW II occurs at 10^4 sliding cycles until $5x10^4$ sliding cycles, characterized by rapid volume loss until transition to UMW III occurs where volume loss stabilizes. UMW III starts from $5x10^4$ sliding cycles until $1.5x10^6$ sliding cycles.

4.2.2 Surface damage evolution

Shown in Figure 4- 2 is an SEM micrograph of particles located inside the wear track at 10^3 sliding cycles. The instant that sliding contact initiates, the load is directly supported by the silicon particles, and cracking and fracturing of the silicon particles can be evidenced. More fracture is evidenced in needle like particles; whereas, the smaller particles appear to be intact. The start of pile-up formation can be evidenced due to the elevated matrix adjacent to the particle. Shown in Figure 4- 3 (a) is a 3-D optical profilometry image of the wear track at 10^3 sliding cycles showing the raised matrix around the silicon particle in the direction of sliding. The corresponding 3-D optical profilometry image of the flattened counterface is shown in Figure 4- 3 (b). The formation of the grooves can be observed corresponding the wear track. Shown in Figure 4- 4 is an SEM micrograph at $5x10^3$ sliding cycles showing evidence of pile-up formation. The formation of pile-up occurs greater in the direction of sliding. At each progressive stage in the UMW I, an increase in the amount of pile formation can be evidenced due to the sinking-in of the silicon particles. As the sliding continues, the sinking-in particles and raided matrix (pile-up) reach the same elevation. In the UMW I stage, contact is only limited to the elevated silicon particles, whereas the matrix remains undamaged resulting in no material loss. Transition to the UMW II stage results in contact between the piled-up matrix and the counterface, resulting in wear loss in the form of material removal.

The UMW II stage progresses from 10^4 until $5x10^4$ sliding cycles. Shown in Figure 4- 5 is an SEM micrograph of the wear track at $2.5x10^4$ sliding cycles. Contact between the counterface and the matrix can be evidenced. The piled up aluminum begins to smear in the direction of sliding; however, some of the matrix in the middle of the

wear track still appears to be unaffected. Shown in Figure 4- 6 is the wear track at $5x10^4$ sliding cycles. Found on top of silicon particles and nickel-iron particles are what appear to be pockets of oil residue (OR) consisting of Zn, S, P, O, C, and Al is evidenced through EDS analysis. Pockets of OR are more prominent towards the edges of the wear track, whereas within the centre of the wear track, the OR layer appears to be smeared across the harder particles.

Transition to the UMW III stage was accompanied by the stabilization of wear rates. Shown in Figure 4- 7 is an SEM image and EDS analysis of the wear track in the area highlighted. What appears on top of iron-nickel phases and silicon particles are pockets of OR. Pockets of OR consists of elements of Zn, S, C, and O. Analysis of the aluminum matrix showed trace amounts of oil additive elements including Ca. OR appears to be incorporated with the smeared aluminum. Wear tracks in the UMW III region appear uniform throughout the entire wear track as shown in the optical profilometry image at $3x10^5$ sliding cycles in Figure 4- 8 (a). The corresponding optical profilometry image of the counterface is shown in Figure 4- 8 (b). The removal of material can be associated with the formation of grooves due to the damage sustained on the counterface and the ploughing of the matrix from the fractured silicon particles.

4.3 5W30/E85

4.3.1 Volume loss with sliding cycles

Shown in Figure 4- 9 is the volumetric wear for Al-12.6% Si for various sliding cycles at 2N load under boundary lubrication with a mixture of E85 plus 5W30 engine oil at room temperature. The region of UMW I ranges from 10^3 sliding cycles till 10^4 sliding cycles, where no detectable volume loss occurred. Transition from UMW I to UMW II occurs at 10^4 sliding cycles and progresses until $3x10^5$ sliding cycles where large

amounts of volume loss occurs. Stabilization of wear loss occurs as UMW III is obtained.

4.3.2 Surface damage evolution

Shown in Figure 4- 10 is an SEM image of the wear track at $5x10^3$ sliding cycles from the UMW I regime. Silicon particle fracture and formation of pile-up occurs. Large amounts of particle fracture and debris were present throughout the wear track. Shown in Figure 4- 11 is a comparative SEM and WYKO image of a particle where the formation of pileup can clearly be evidenced. No evidence can be found for the formation of any oil residue layers.

Shown in Figure 4- 12 is a tilted (54^o) SEM micrograph of the wear track at 10^4 sliding cycles. The transition to the UMW II stage can be evidenced past this point due to the formation of grooves along the wear track. The grooves are responsible for the removal of material from the wear surface. The grooves form due to the damage to the counterface from the hard silicon particle. In addition, the fractured silicon particles act as third body abrasives which plough the surface and remove the material. The formation of grooves can be evidenced from the optical profilometry image of the wear track at 10^4 sliding cycles as shown in Figure 4- 13 (a) and the corresponding optical profilometry image of the counterface shown in Figure 4- 13 (b).

Shown in Figure 4- 14 is a comparative secondary electron and backscatter micrograph of the flattened matrix at $5x10^4$ sliding cycles (UMW II). The formation of grooves are harder to identify through the SEM micrographs; however, the use of optical profilometry image shows the formation of grooves as shown in Figure 4- 15 (a) at $5x10^4$ sliding cycles. The damage to the corresponding counterface can be seen in the optical profilometry image shown in Figure 4- 15 (b). Semi-quantitative EDS analysis was

conducted on the surface of the counterface at $5x10^4$ (UMW II) sliding cycles as shown in Figure 4- 16. EDS analysis showed concentrations of Fe, C, O, Ca and Si. The detection of Si suggests embedding of silicon fragments onto the counterface during sliding wear. Mainly iron oxide was detected on the surface.

The transition to the UMW III stage occurs as the wear rates stabilize. Shown in Figure 4- 17 is an SEM micrograph of the wear track at 10^6 sliding cycles, tilted at 54^o. The wear track appears non uniform. The formation of an oil residue layer can be evidenced through EDS analysis on the top elevated sections of the track where elements such as Zn, P, S, Can and C was detected as shown in Figure 4- 18.

4.4 XPS characterization

The chemical composition of the resultant tribolayer for wear track lubricated with only 5W30 or a mixture of E85 plus 5W30 at $3x10^5$ and 10^6 has been analyzed through XPS and is shown in Figure 4- 19 A-D. The tribolayer consists of Zn, O, C, Ca, S, Si and Al. Figure 4- 20 shows a comparative elemental composition analysis of the wear track at $3x10^5$ sliding cycles and 10^6 sliding cycles for both lubricated conditions. Wear tracks which develop under the mixed lubricated conditions show a richer concentration of additives in comparison to just engine oil lubricated wear tracks. An increase in the number of sliding cycles, results in an increase in the quantity of additives detected on the surface. The presence of these additives confirms the development of an oil residue layer. Scans on the wear track for zinc and sulphur rich film on the tribolayer under mixed lubricated condition at $3x10^5$ sliding cycles were also investigated to determine the type of film development. Binding energy for zinc compound was detected at 1021.71eV correlating to zinc oxide (ZnO) as shown in Figure 4- 21. Binding energy for sulphur at 168.61eV correlated to sulphate film formation as shown in Figure 4- 22.

Depth profiling inside the wear track at 10^6 sliding cycles for both lubricated conditions shows very similar results for Zn, Ca, Al, and Si as shown in Figure 4- 23; however, a higher concentration of carbon was detected for the mixed lubricated conditions in comparison to just engine oil as shown in Figure 4- 24. Additionally, a lower concentration of oxygen was also evidenced as shown in Figure 4- 24, for mixed lubricated condition.

4.5 Subsurface characterization of the tribolayer

Shown in Figure 4- 25 is the cross-section of a wear track at $3x10^5$ sliding cycles from the mixed lubricated test (E85 plus 5W30) prepared using the FIB milling technique. This overview section shows an area of the wear track identifying sunk-in silicon particles and deformed aluminum. Shown in Figure 4- 26 is the heavily deformed aluminum adjacent to a silicon particle. Ultra fine aluminum grains can be seen roughly 100-200 nm in size supporting an oil residue layer which appears to extend up to 120 nm below the contact surface. The aluminum grains below the heavily deformed aluminum and ultra fine aluminum grains appear to be larger in size, ranging from sizes greater than 300 nm. A discontinuous oil residue layer can be identified onto of the aluminum matrix, highlighted in the red box. The zoomed in TEM micrograph accompanied by the semi-quantitative chemical analysis (EDS) is shown in Figure 4- 27, where C, O, and Ca can be found. The depth of the oil residue layer was measured to be roughly 120 nm below the contact surface. Shown in Figure 4- 28 is sunk-in silicon particle at the same level as the adjacent aluminum. Due to the sliding contact from the counterface, the silicon particle appears to contain large dislocations and twin structures. Close examination of the interface using a fast Fourier transform (FFT) revealed a layer of amorphous structure and crystalline silicon structure as shown in Figure 4- 29. Shown in Figure 4- 30 is the

electron diffraction pattern at the interface where crystalline silicon and amorphous structure was identified. A zone axis of $[\bar{1}14]$ was indexed for the crystalline silicon particle.

4.6 Tribolayer characterization using FTIR

The chemical characteristic of the tribolayer was investigated employing FTIR scans inside the wear tracks. Shown in Figure 4- 31 (a), is the adsorption spectrum inside the wear track at 10^6 sliding cycles with a mixed E85/5W30 lubrication. Adsorption band characteristics from the stretching of the hydroxyl group located at 3400 cm^{-1} suggests that –OH groups form hydrogen bonds most probably belonging to alcohol. Doublets due to the stretching of the C-H bonds were identified at 2926, 2862 and 1410 cm^{-1} belonging to aliphatic hydrocarbons. Adsorption peaks located at 1622, 1578, 1134, and 1052 cm^{-1} corresponds to the stretching of C-O bond. Shown in Figure 4- 31 (b) is the adsorption spectrum inside the wear track at 10^6 sliding cycles with only 5W30 lubrication. No evidence can be identified belonging to the adsorption of alcohol layers because no alcohol was present during the wear test. Shown in Figure 4- 31 (c) is the adsorption band inside the wear tack with only ethanol lubrication. Due to the formation of large oxides no evidence of adsorption of alcohol was present.

4.7 Ethanol only wear tests

Wear tests using only ethanol as lubricant was also conducted in order to understand the behaviour of the alloy in the absence of engine oil. Figure 4- 32 shows the volume wear rates for two tests with only ethanol lubrication indicating high volume wear. Shown in Figure 4- 33 is a 3D optical profilometry image of the resultant wear track at 10^5 sliding cycles. The formation of a deep and wide wear track is evidenced. Shown in Figure 4- 34 is a secondary electron micrograph of the wear track at 10^4 sliding

cycles. A high concentration of oxygen was detected using semi-quantitative EDS on the surface of the wear track suggesting the formation of aluminum oxide and iron oxide as shown in Figure 4- 35. Surface oxide layers form as scales and detach from the matrix, acting as third body abrasives during sliding wear, resulting in high wear rates. Shown in Figure 4- 36 is the corresponding second electron micrograph and a semi-quantitative EDS analysis on the surface of the counterface at 10^5 sliding cycles. The formation of iron oxide and Si fragments were detected.

4.8 Coefficient of friction

Shown in Figure 4- 37 and Figure 4- 38 are the coefficient of friction (COF) data plotted versus the number of sliding cycles. The surface roughness of the corresponding wear track has been provided in order to correlate the behaviours. A decreasing trend in the COF values can be evidenced for both lubricated conditions. At the start of sliding, boundary lubricated regime was achieved resulting in high COF values. As the number of sliding cycles increased, the contact regime changed from boundary lubricated conditions to either mixed or hydrodynamic lubrication and in turn decreasing the COF values. The decrease in COF values can also be correlated to the formation of a stable protective oil residue layer which can act to separate the contacting surfaces. The roughness of the wear track showed a comparable behaviour to the COF, where a rougher wear track correlates to an increase in the COF value and vice versa. Higher COF values were also evidenced for mixed lubricated conditions in comparison to engine oil.

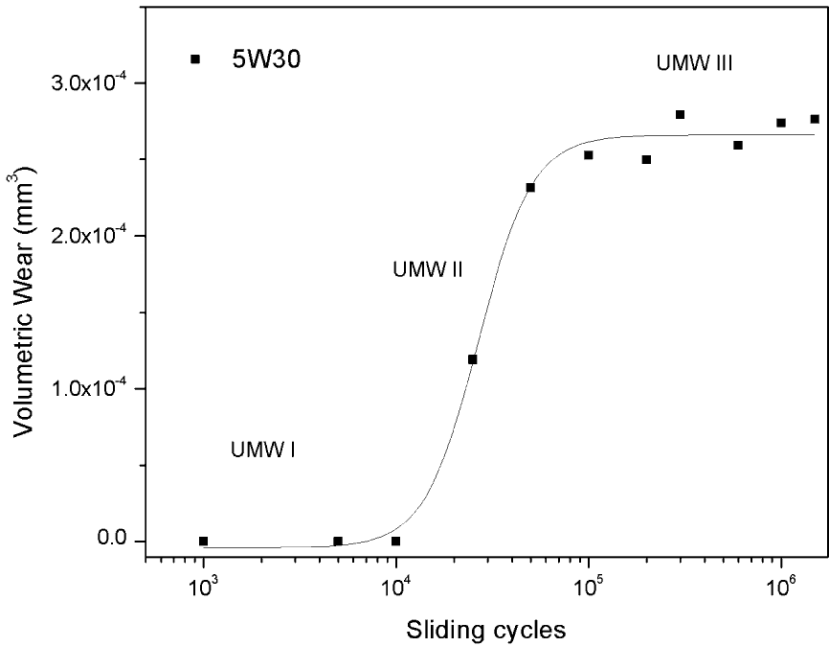

Figure 4- 1: Plot of volumetric wear with sliding cycles for Al-12.6% Si. Boundary lubrication was achieved using 5W30 lubrication using 2N load at room temperature.

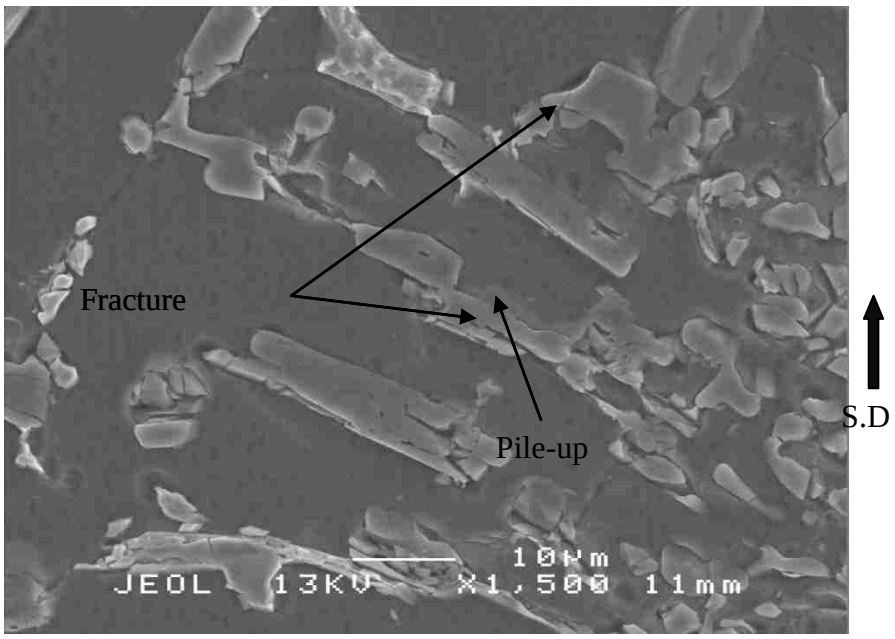

Figure 4- 2: Secondary electron micrograph at 10^3 sliding cycles using 2 N load and 5W30 lubrication at room temperature. Damage limited to silicon particles through fracture. Evidence of pile-up formation can be noticed.

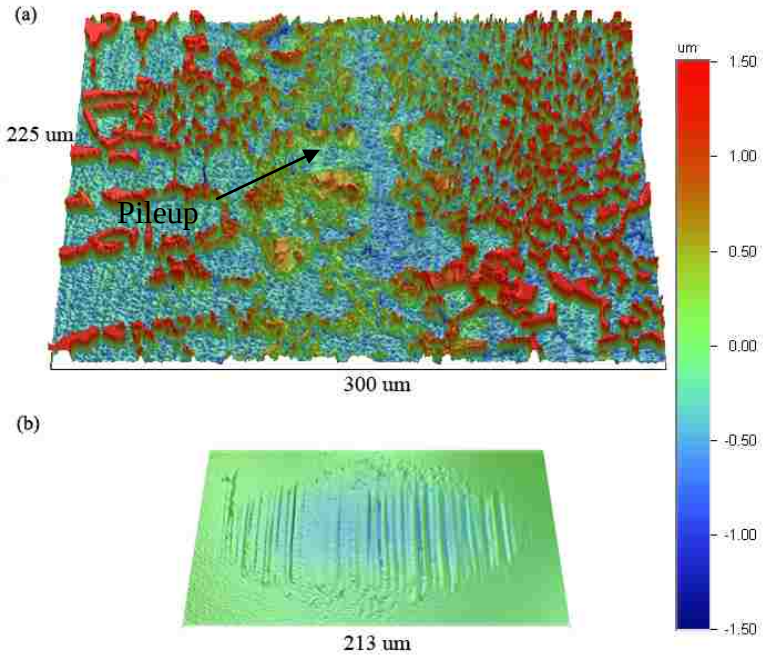

Figure 4- 3: (a) Optical profilometry image of the wear track at 10^3 sliding cycles with 2 N load under 5W30 boundary lubricated conditions. The formation of pileup can be evidenced adjacent to the silicon particles which support the load. (b) Corresponding optical profilometry image of the counterface surface.

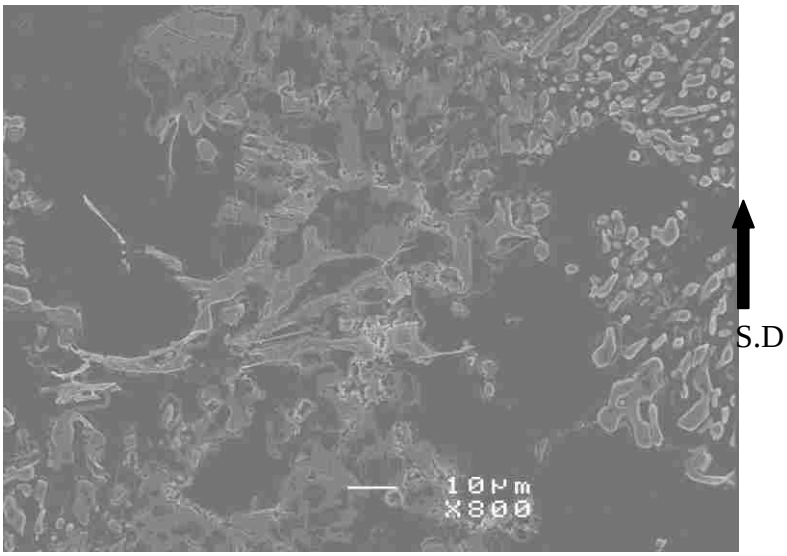

Figure 4- 4: Secondary electron micrograph at $5x10^3$ sliding cycles (UMW I) using 2 N load and 5W30 lubrication at room temperature. The sinking in of the particles results in the formation of pile along the direction of sliding.

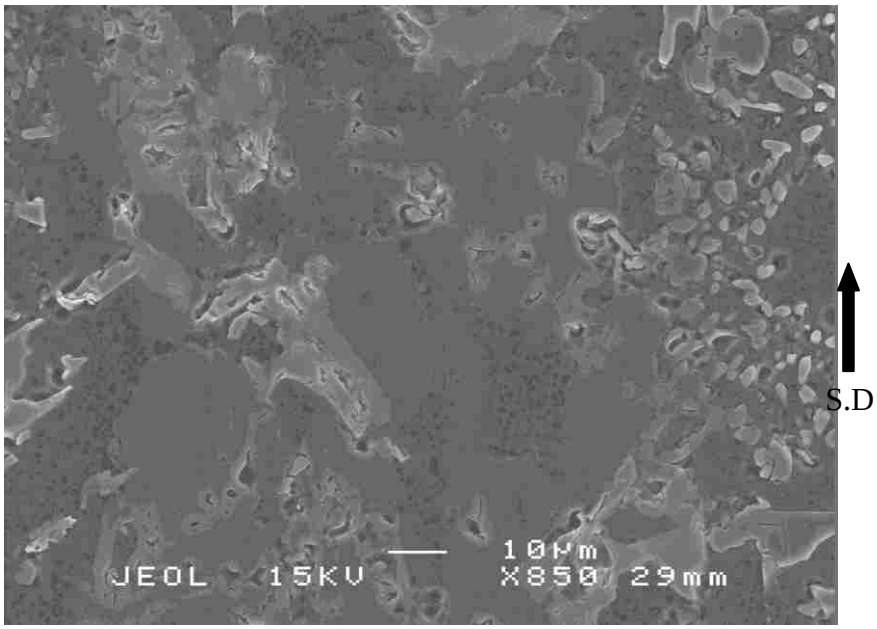

Figure 4- 5: Secondary electron micrograph at $2.5x10^4$ sliding cycles (UMW II) using 2 N load and 5W30 lubrication at room temperature. Aluminum matrix makes contact with counterface resulting in material removal.

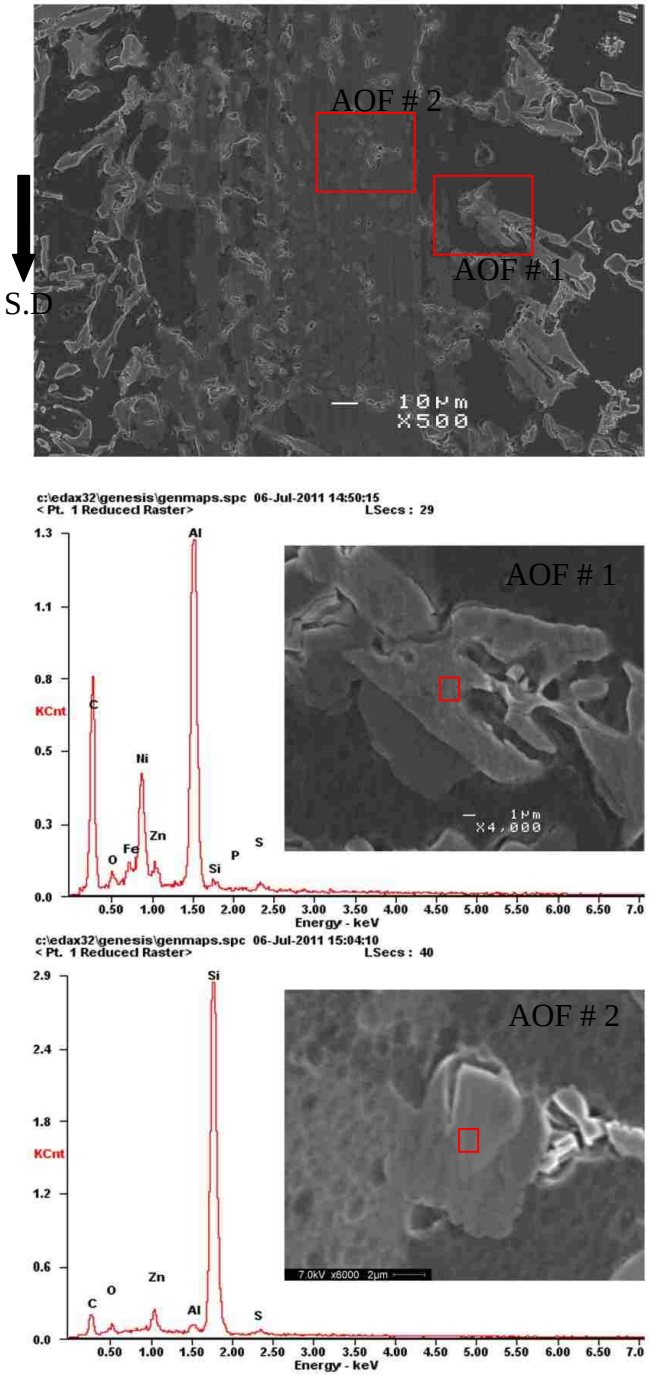

Figure 4- 6: Secondary electron micrograph at $5x10^4$ sliding cycles (UMW II) using 2 N load and 5W30 lubrication at room temperature. AOF # 1 shows the formation of pockets of oil residues on top of nickel iron particles towards the edge of the wear track. AOF # 2 shows smeared oil residue layer towards the center of the wear track.

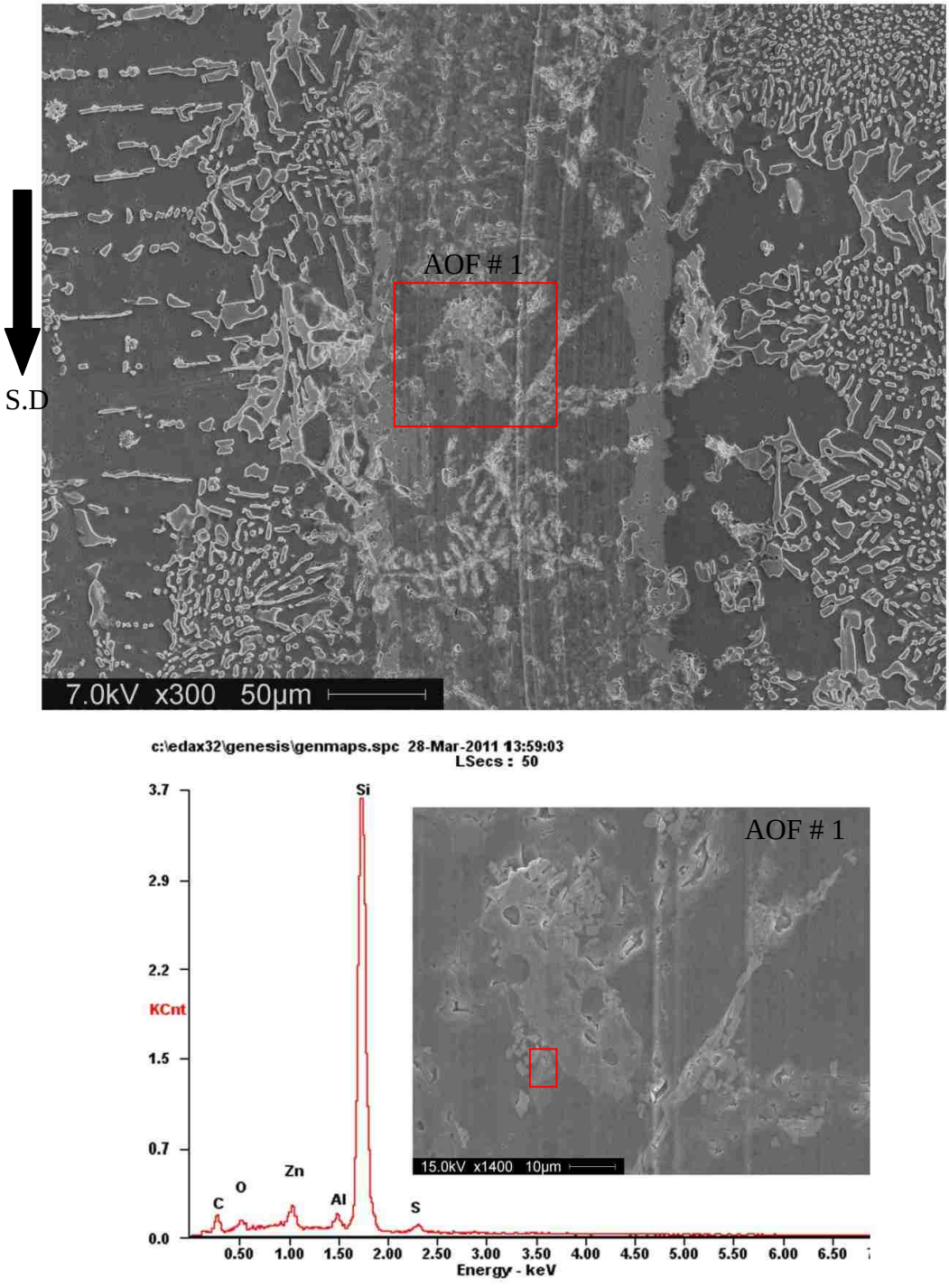

Figure 4- 7: Secondary electron micrograph at $3x10^5$ sliding cycles (UMW III) using 2 N load and 5W30 lubrication at room temperature. AOF # 1 shows pockets of oil residue on top of silicon particles in the wear track.

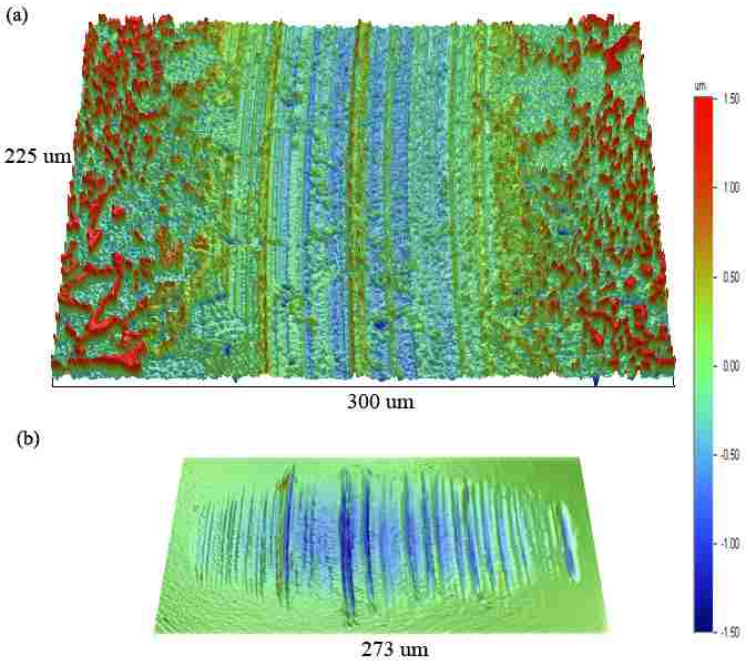

Figure 4- 8: (a) Optical profilometry image of the wear track at $3x10^5$ sliding cycles with 2 N load under 5W30 boundary lubricated conditions. Wear track appears uniform. Formation of grooves results in the removal of material. (b) Corresponding optical profilometry image of the counterface surface.

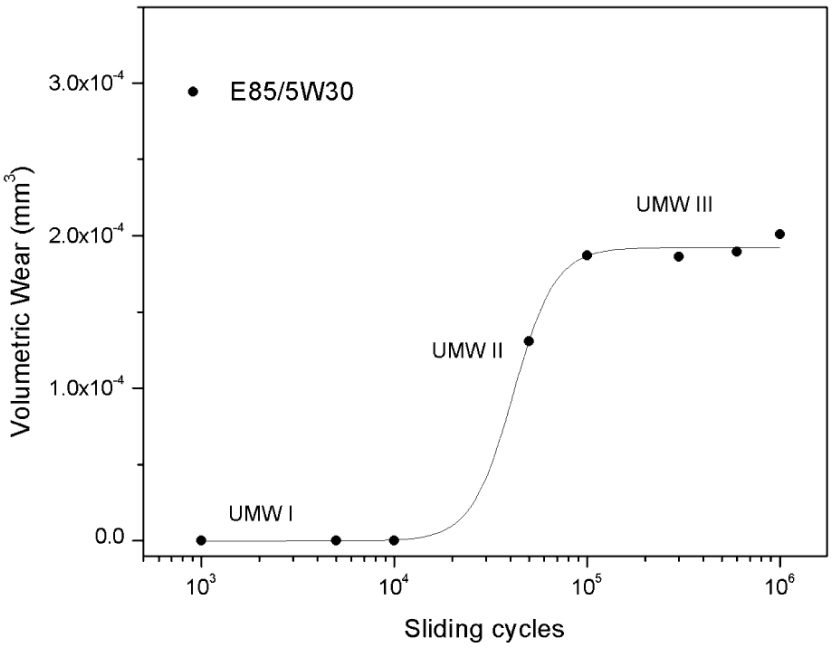

Figure 4- 9: Plot of volume loss with sliding cycles for Al-12.6% Si. Boundary lubrication was achieved using a mixture of 5W30/E85 lubrication using 2N load.

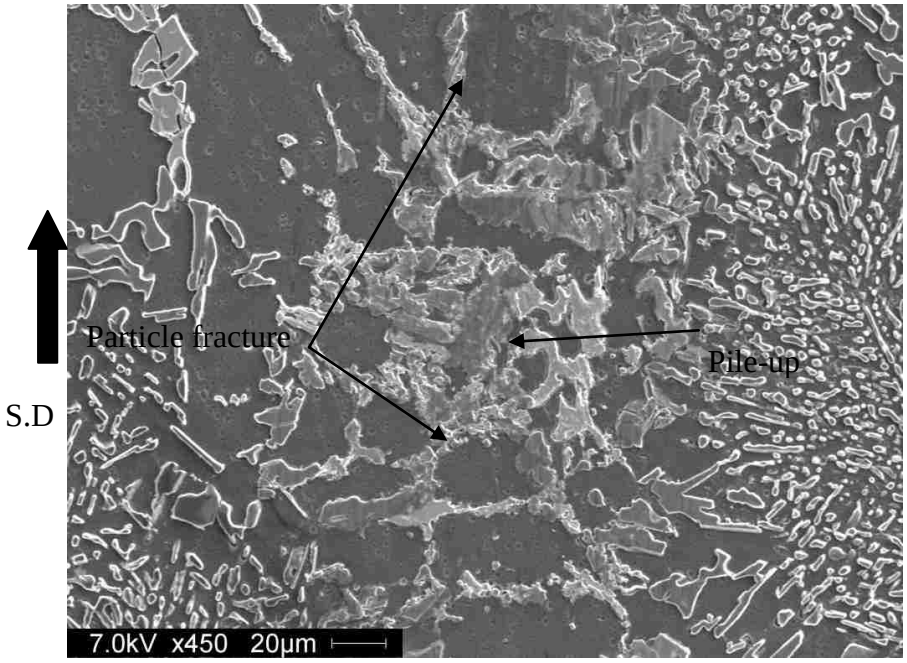

Figure 4- 10: Secondary electron micrograph at 5x10^3 sliding cycles using 2 N load and E85 plus 5W30 lubrication at room temperature. Damage limited to silicon particles through fracture. Evidence of pile-up formation can be noticed.

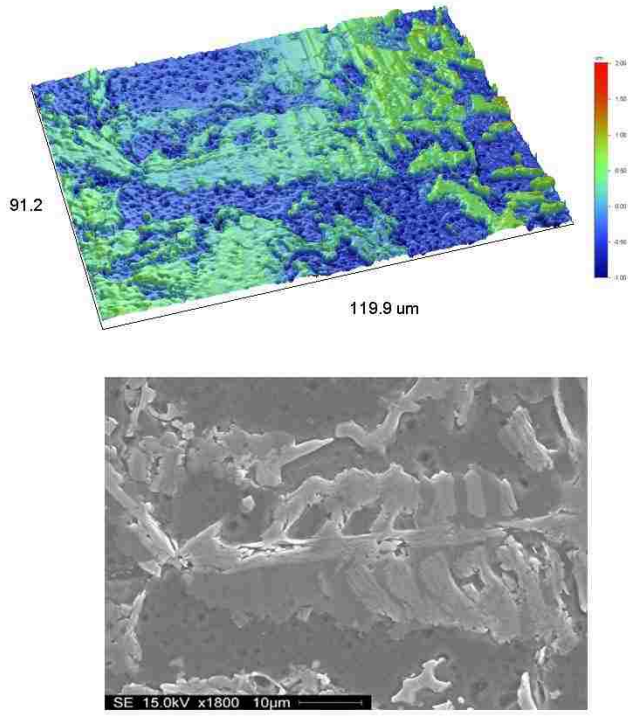

Figure 4- 11: Secondary electron micrograph and WYKO image at $5x10^3$ sliding cycles using 2 N load and a mixture of E85/5W30 lubrication at room temperature. Formation of pileup area in the wear track can be identified by the elevated matrix surrounding the particles.

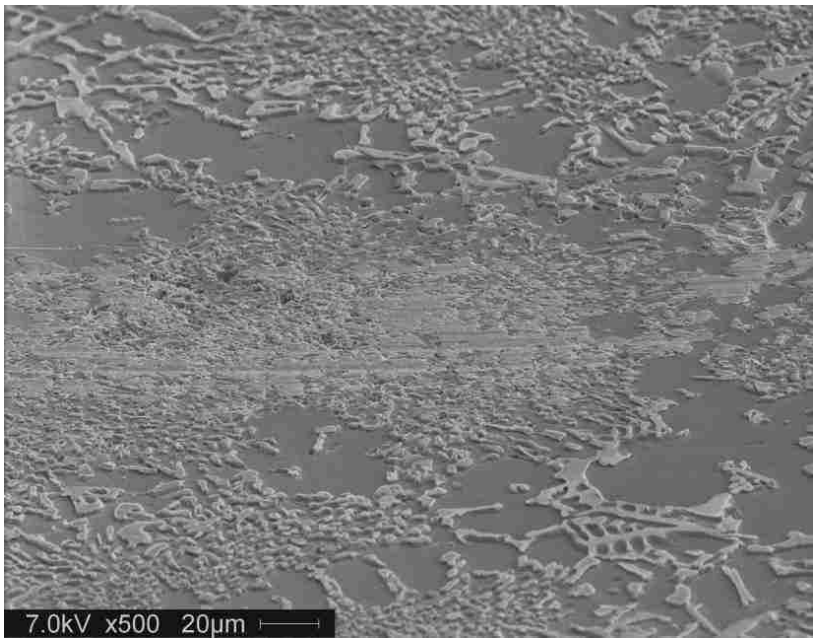

Figure 4- 12: Secondary electron micrograph at 10^4 sliding cycles (UMW I) using 2 N load and a mixture of E85/5W30 lubrication at room temperature. The formation of grooves along the wear track signifies the initiation of material removal from the surface.

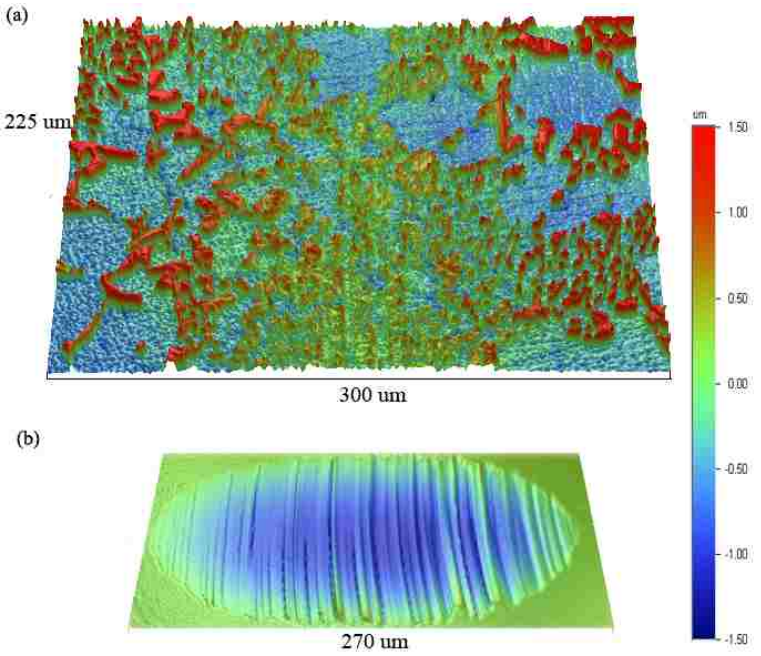

Figure 4- 13: (a) **Optical profilometry image of the wear track at 10^4 sliding cycles with 2 N load using a mixture of E85/5W30 lubricated conditions. Formation of grooves results in the removal of material. (b) Corresponding optical profilometry image of the counterface surface.**

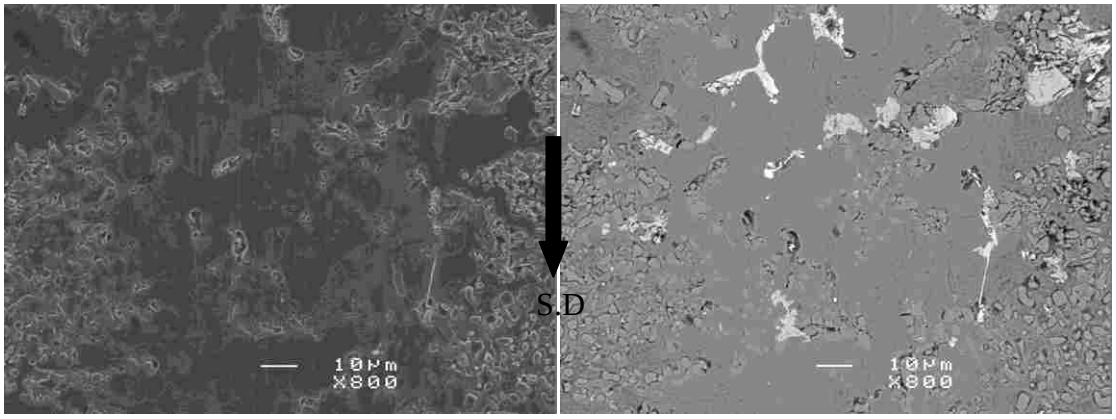

Figure 4- 14: Secondary electron micrograph and backscatter micrograph at $5x10^4$ sliding cycles (UMW II) with a 2 N load using a mixture of E85/5W30 lubricated conditions. The flattening of the matrix can be evidenced resulting in the formation of a compacted layer.

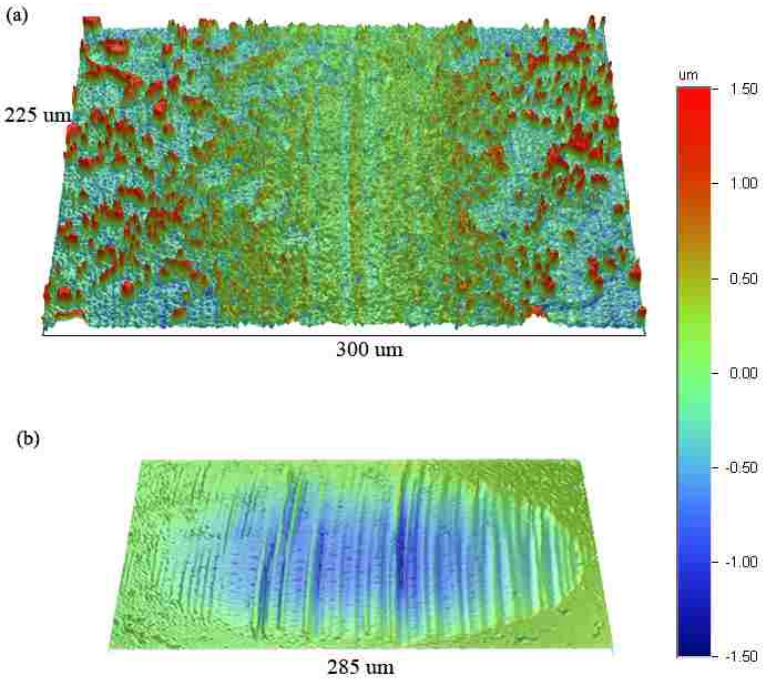

Figure 4- 15: (a) Optical profilometry image of the wear track at $5x10^4$ sliding cycles with 2 N load using a mixture of E85/5W30 lubricated conditions. Flattening of the matrix can be evidenced also the formation of grooves leading to the removal of material. (b) Corresponding optical profilometry image of the counterface.

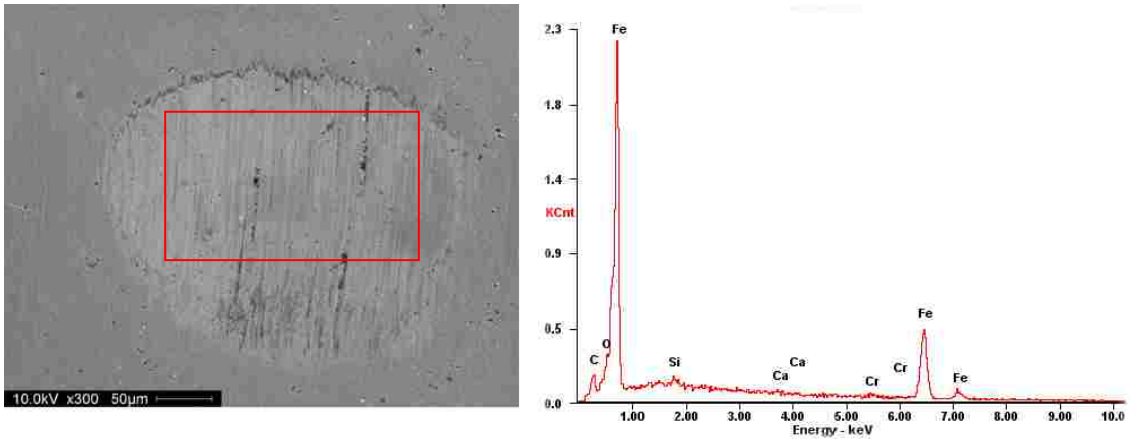

Figure 4- 16: Counterface at $5x10^4$ (UMW II) sliding cycles with a mixture of E85/5W30 lubrication. Semi-quantitative chemical analysis suggests the formation of iron oxide and embedding of silicon fragments.

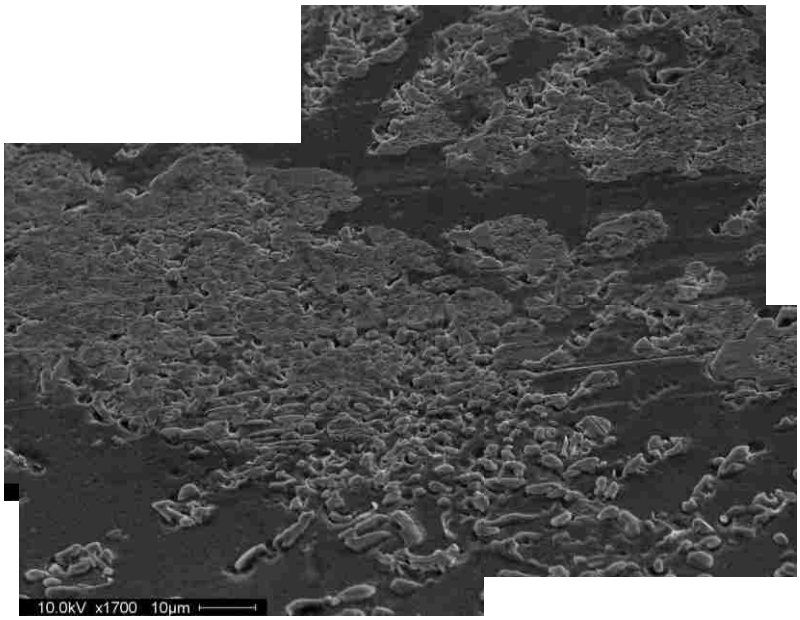

Figure 4- 17: Secondary electron micrograph at 10^6 sliding cycles (UMW III) using 2 N load and a mixture of E85/5W30 lubrication at room temperature.

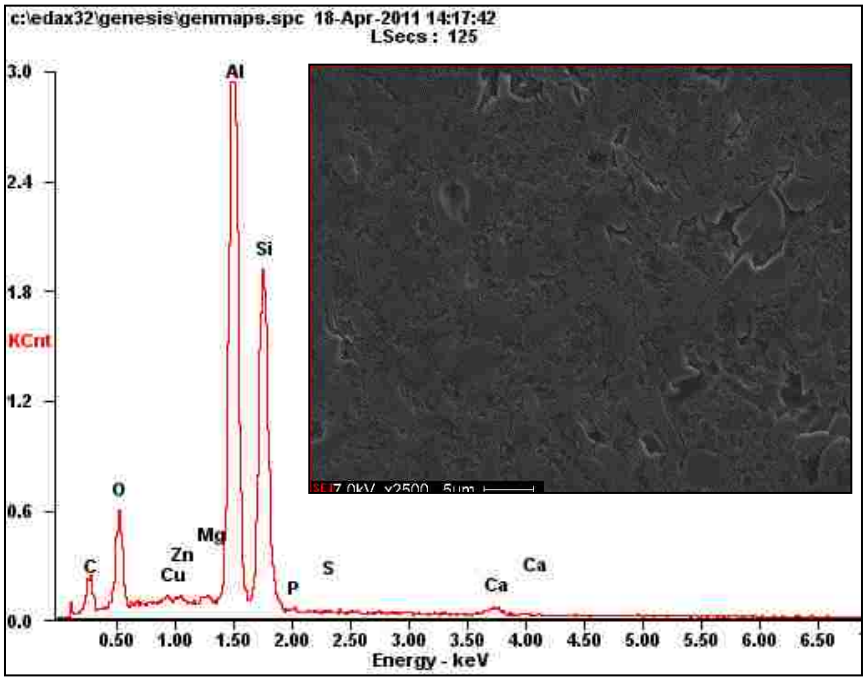

Figure 4- 18: EDS analysis inside the wear track at 10^6 sliding cycles (UMW III) using 2 N load and a mixture of E85/5W30 lubrication at room temperature. Traces of oil residue layer can be evidenced through the detection of Zn, P, S, Ca and C.

A

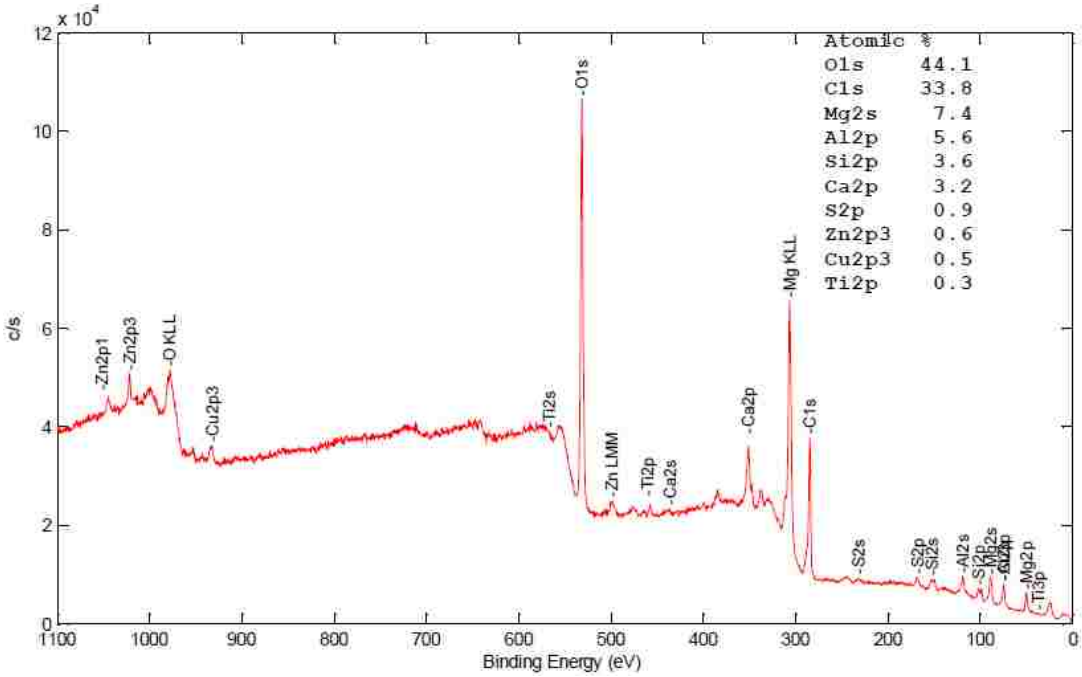
x 10^4
c/s
Binding Energy (eV)
Atomic %
O1s 44.1
C1s 33.8
Mg2s 7.4
Al2p 5.6
Si2p 3.6
Ca2p 3.2
S2p 0.9
Zn2p3 0.6
Cu2p3 0.5
Ti2p 0.3
Zn2p1
Zn2p3
O KLL
Cu2p3
Ti2s
O1s
Zn LMM
Ti2p
Ca2s
Ca2p
Mg KLL
C1s
S2s
S2p
Si2s
Al2s
Si2p
Mg2s
Mg2p
Ti3p

B

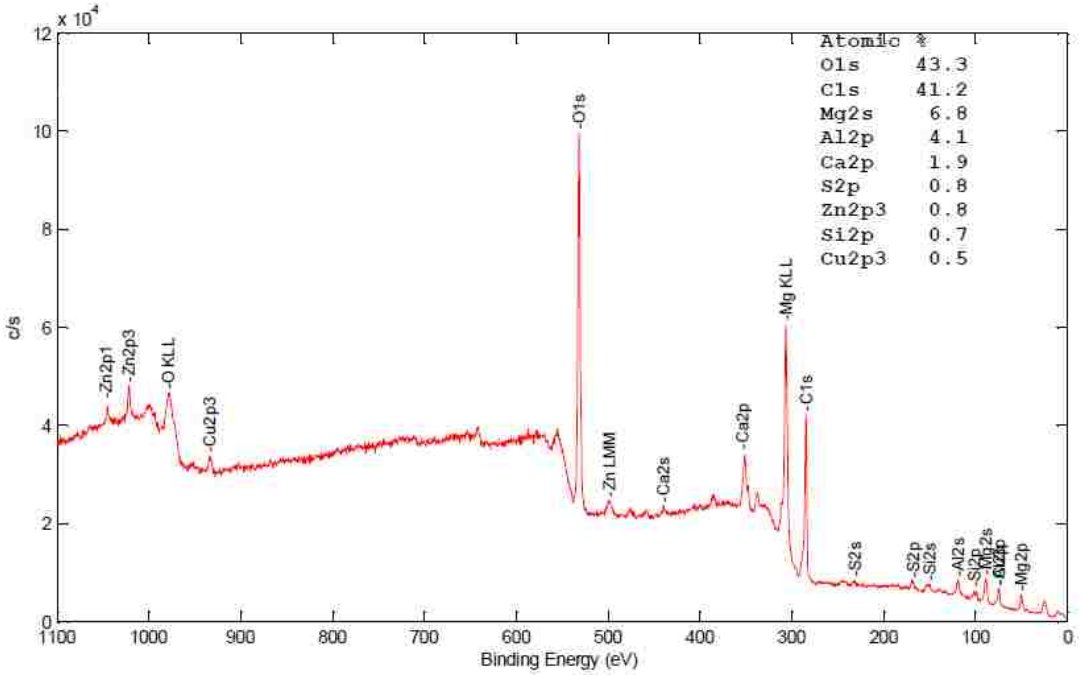
x 10^4
c/s
Binding Energy (eV)
Atomic %
O1s 43.3
C1s 41.2
Mg2s 6.8
Al2p 4.1
Ca2p 1.9
S2p 0.8
Zn2p3 0.8
Si2p 0.7
Cu2p3 0.5
Zn2p1
Zn2p3
O KLL
Cu2p3
O1s
Zn LMM
Ca2s
Ca2p
Mg KLL
C1s
S2s
S2p
Si2s
Al2s
Si2p
Mg2s
Mg2p

C

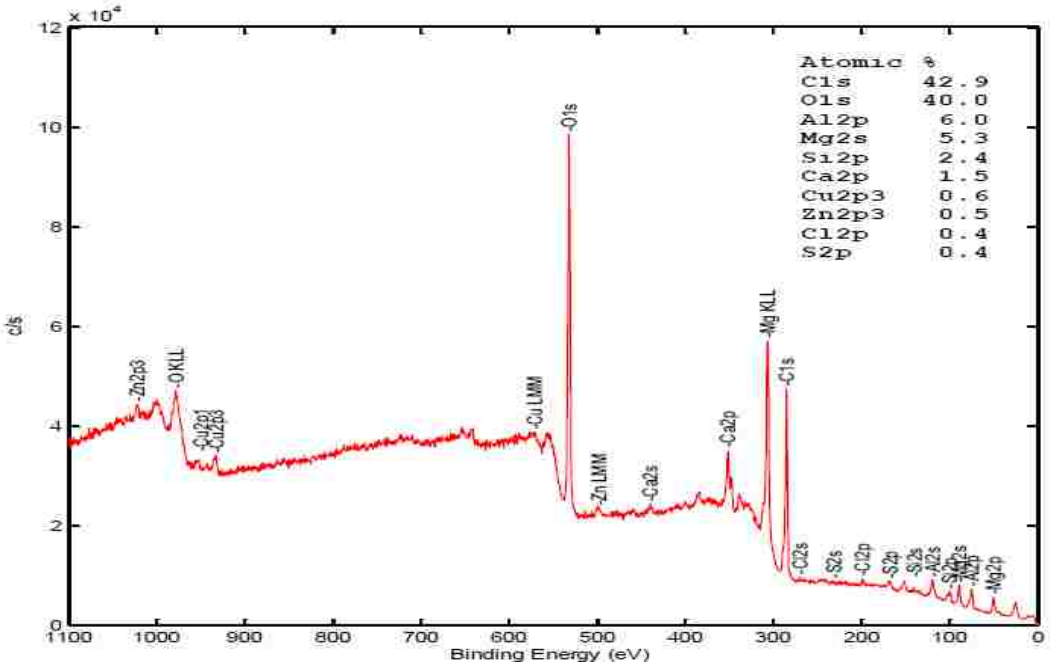

D

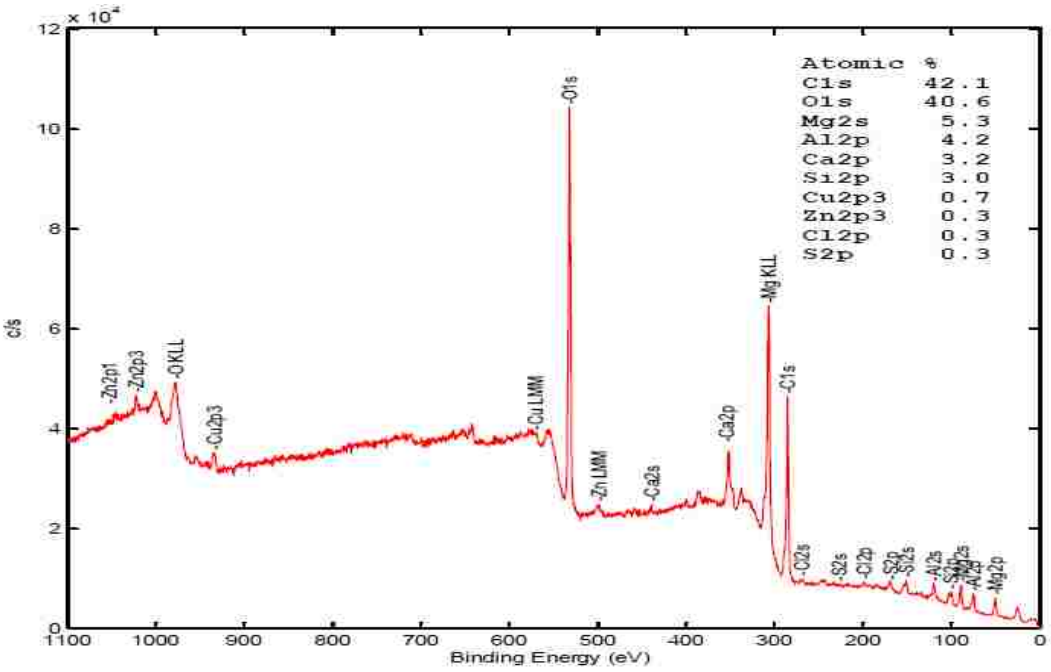

Figure 4- 19: XPS chemical composition of the tribolayer developed under 2N load; (A) $3x10^5$ sliding cycles using E85/5W30 mixed lubrication. (B) 10^6 sliding cycles using E85/5W30 mixed lubrication. (C) $3x10^5$ sliding cycles using 5W30 lubrication. (D) 10^6 sliding cycles using 5W30 lubrication.

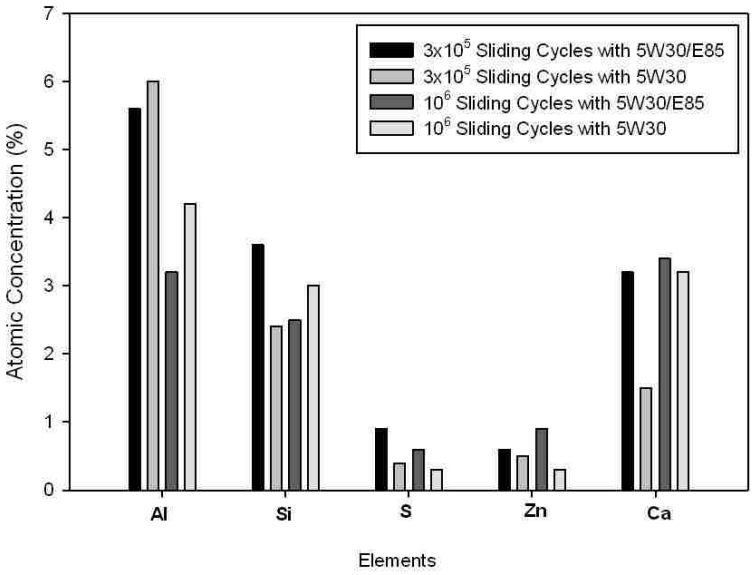

Figure 4- 20: Comparison of the chemical composition of the tribolayer using XPS to illustrate the differences in the concentration of elements compromising the oil residue layer.

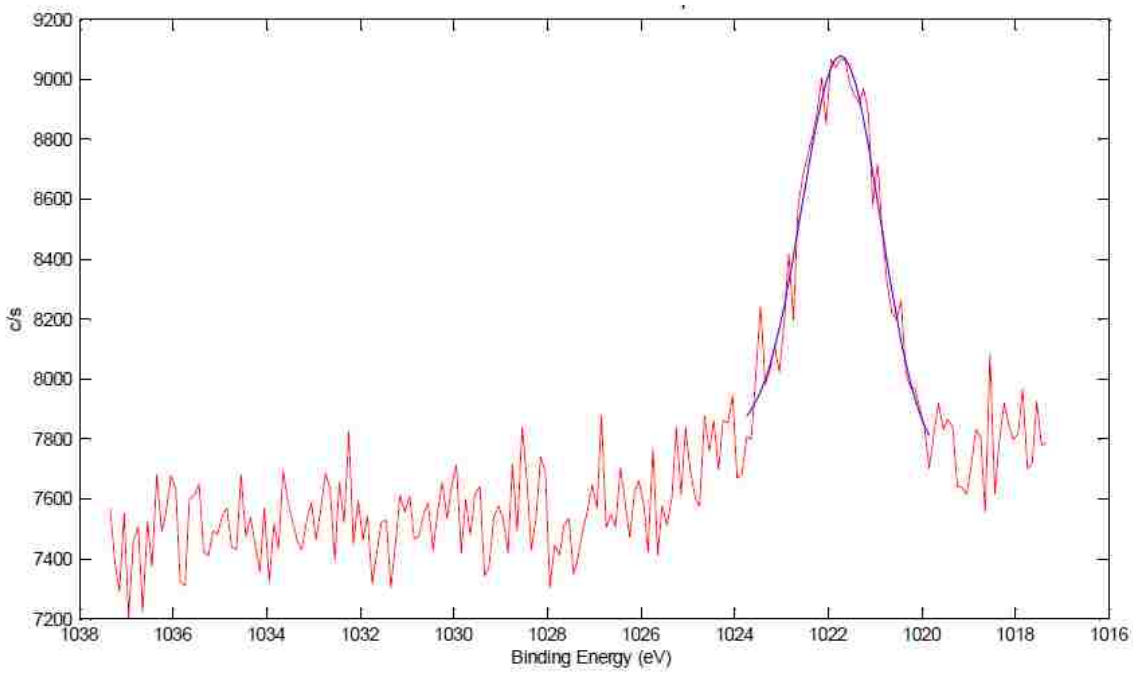

Figure 4- 21: XPS scans inside the wear track at $3x10^5$ sliding cycles with a mixture of E85/5W30 lubrication. Binding energy for ZnO film formation at 1021.71 eV was detected.

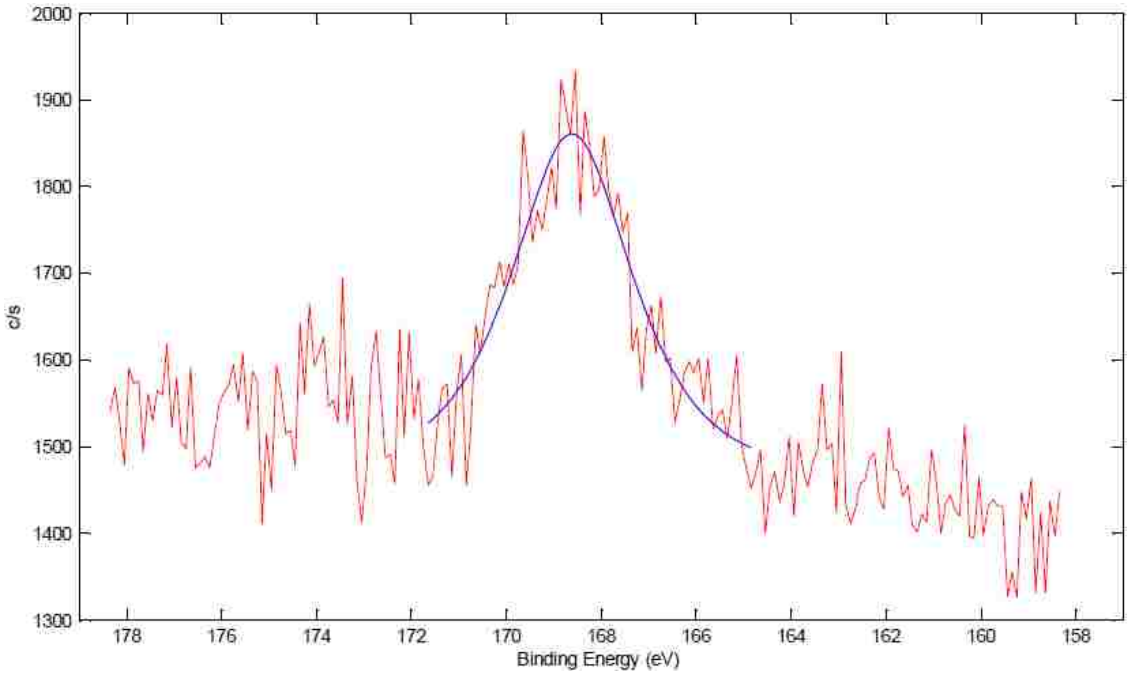

Figure 4- 22: XPS scans inside the wear track at $3x10^5$ sliding cycles with a mixture of E85/5W30 lubrication. Binding energy for sulphate film formation at 168.61 eV was detected.

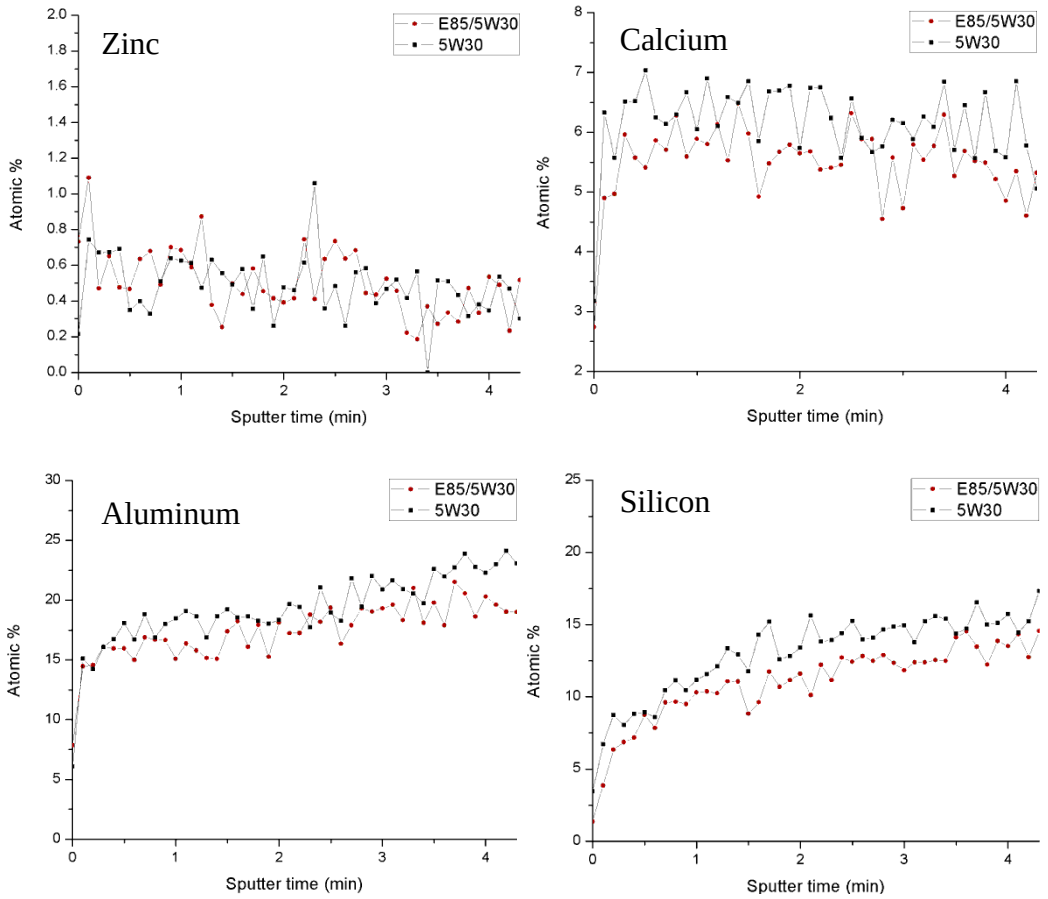

Figure 4- 23: XPS scan for zinc, calcium, aluminum, and silicon atomic % as a function of time inside wear track at 10^6 sliding cycles for both lubricated conditions.

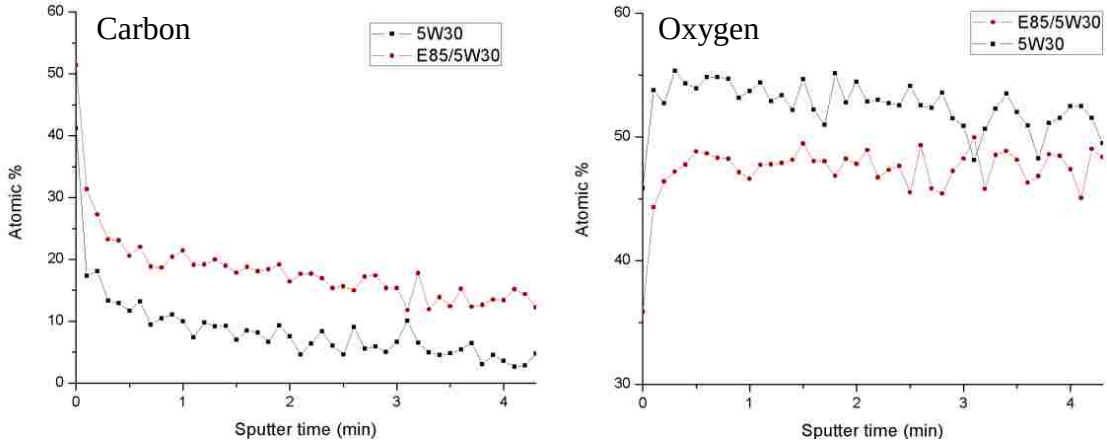

Figure 4- 24: XPS scan for carbon and oxygen atomic % as a function of time inside wear track at 10^6 sliding cycles for both lubricated conditions.

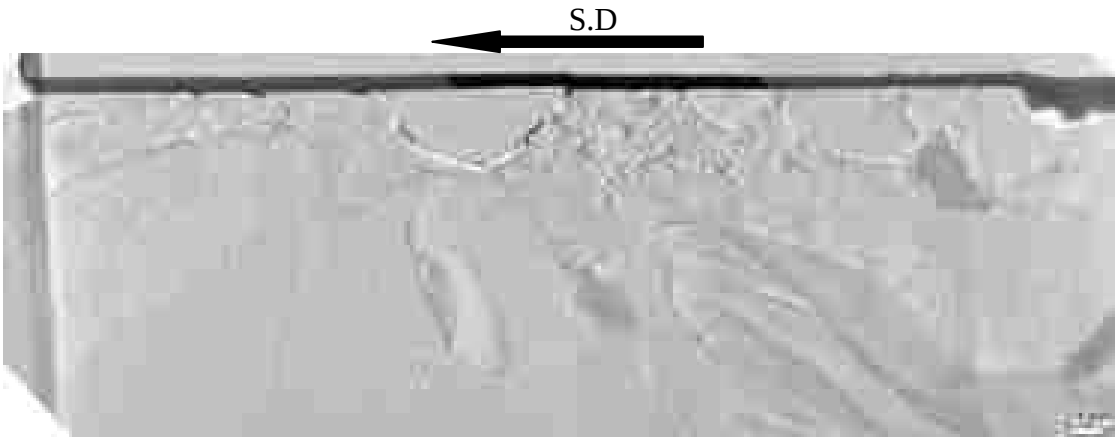

Figure 4- 25: Cross-sectional TEM micrograph of the wear track at $3x10^5$ sliding cycles under mixture of E85/5W30 lubrication.

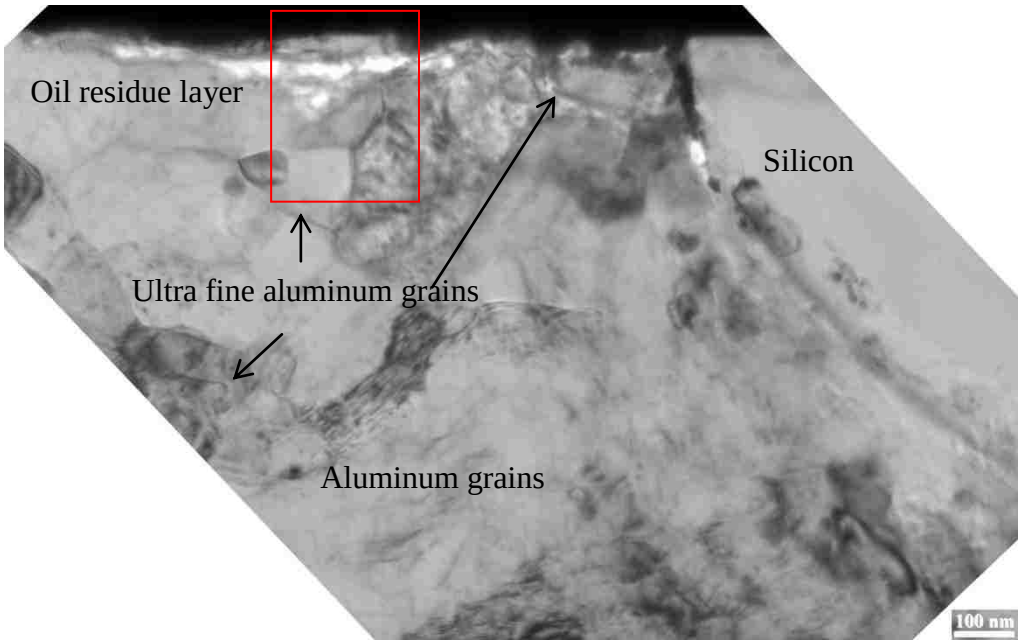

Figure 4- 26: Cross-sectional TEM micrograph of the heavily deformed aluminum featuring a nano-crystalline structure (100-200nm) supporting a thin oil residue layer near a silicon particle at $3x10^5$ sliding cycles under mixed E85 plus 5W30 boundary lubrication.

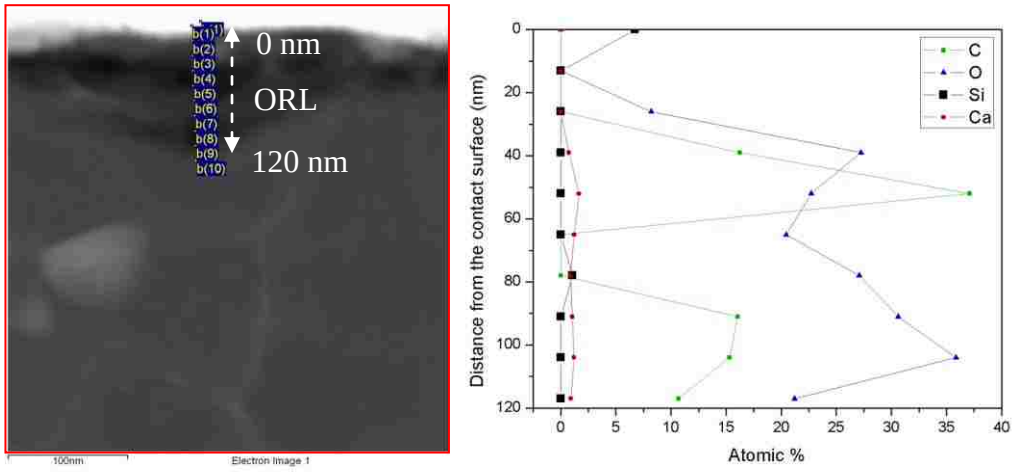

Figure 4- 27: TEM micrograph (a) zoomed in section outlined in Figure 4- 26, of the aluminum matrix featuring a discontinuous oil residue layer and EDS analysis location, (b) a plot of element concentration (at. %) vs. distance from the contact surface up to 120 nm illustrating the chemical composition of the oil residue.

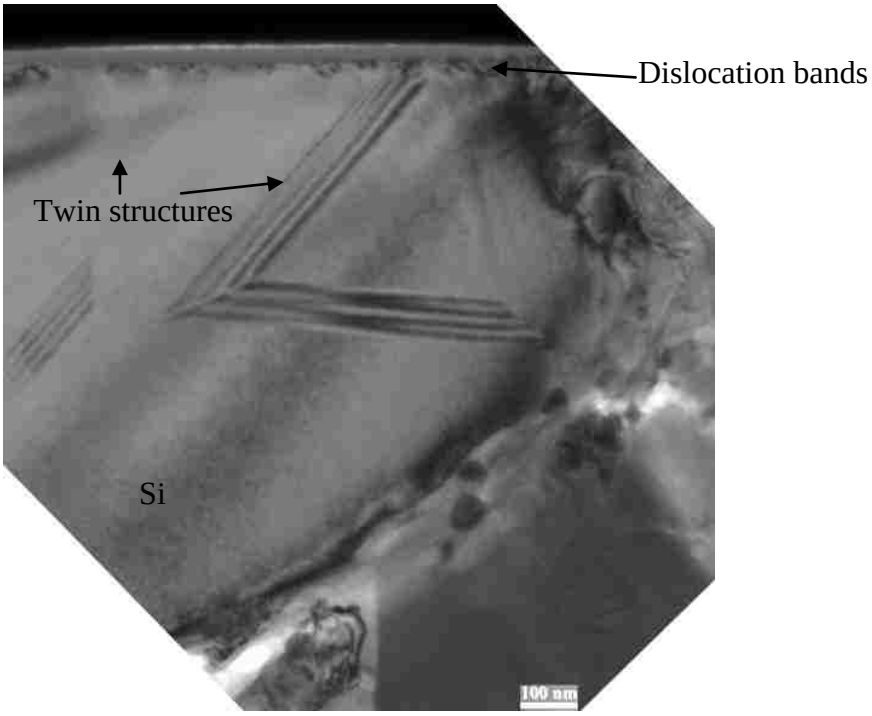

Figure 4- 28: Cross-sectional TEM micrograph of a silicon particle inside the wear track at $3x10^5$ sliding cycles under a mixture of E85/5W30 lubrication. The formation of twin structures and dislocations can be evidenced due to the sliding contact from counterface.

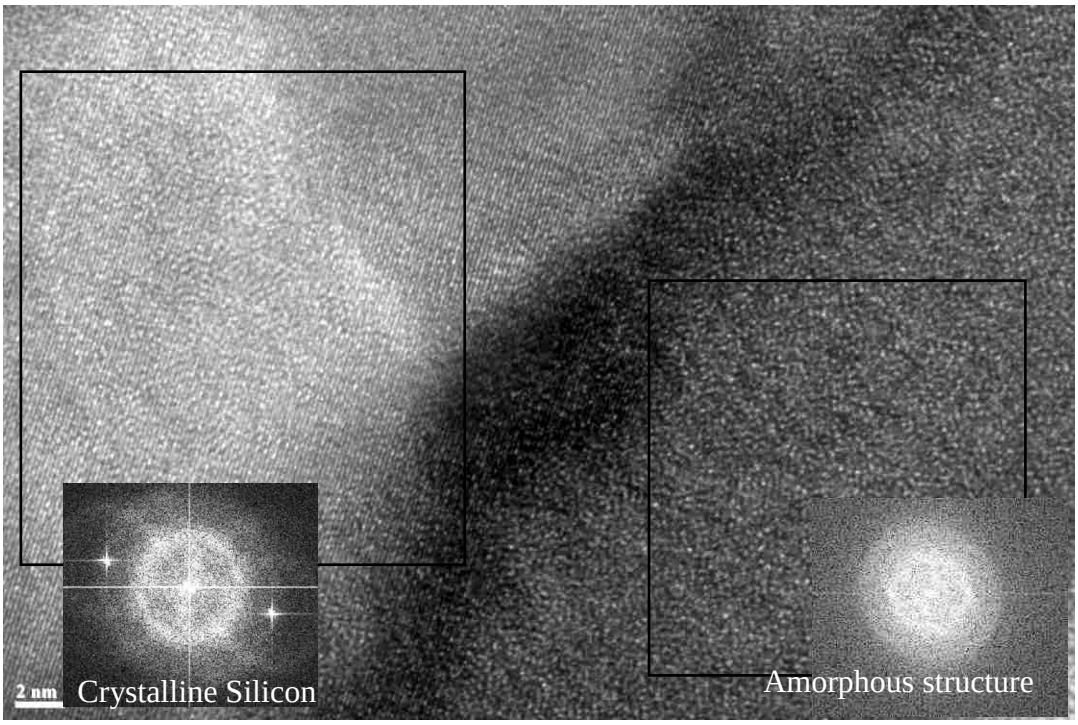

Figure 4- 29: HRTEM micrograph of the amorphous layer on top of the crystalline silicon particle. The formation of an amorphous layer can be evidenced on top of crystalline structure.

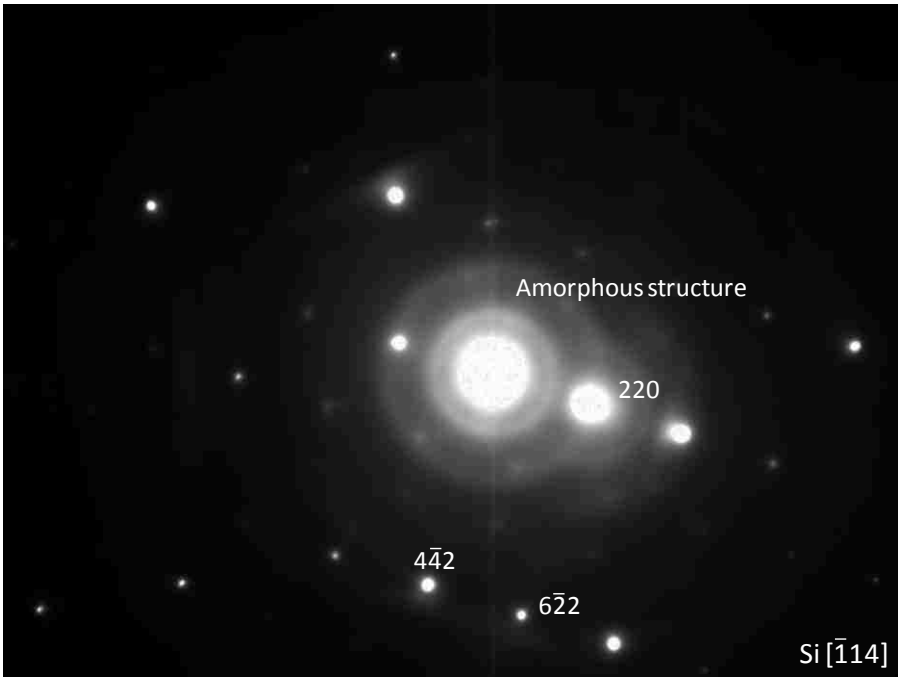

Figure 4- 30: Electron diffraction pattern at the silicon interface. Zone axis of [$\bar{1}$14] was indexed.

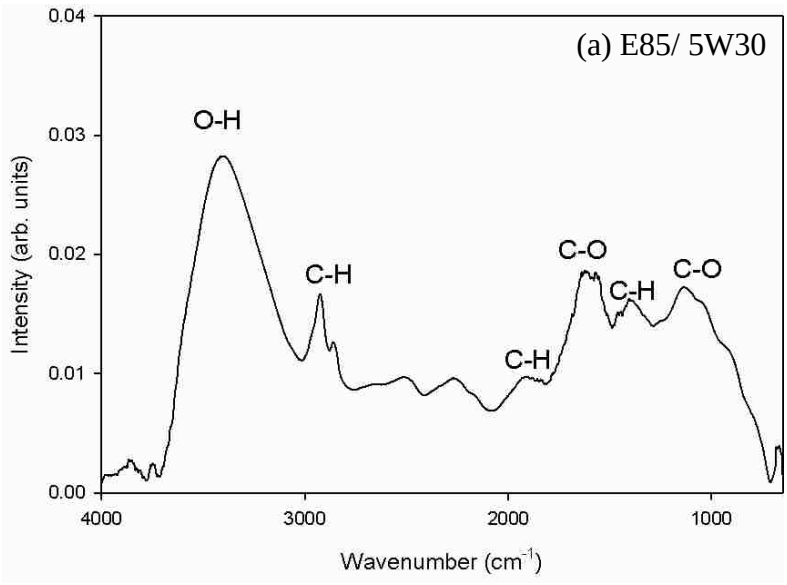
(a) E85/ 5W30
O-H
C-H
C-H
C-O
C-H
C-O
Intensity (arb. units)
Wavenumber (cm-1)
0.04
0.03
0.02
0.01
0.00
4000
3000
2000
1000

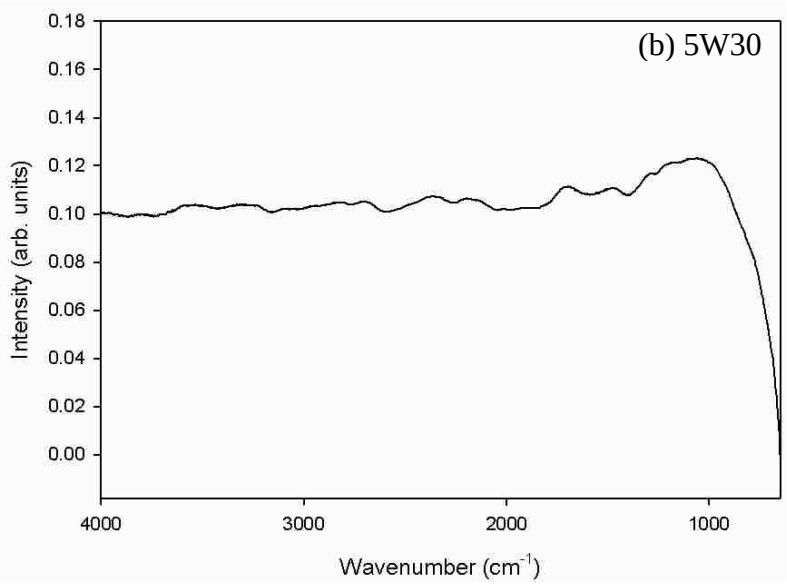
(b) 5W30
Intensity (arb. units)
Wavenumber (cm-1)
0.18
0.16
0.14
0.12
0.10
0.08
0.06
0.04
0.02
0.00
4000
3000
2000
1000

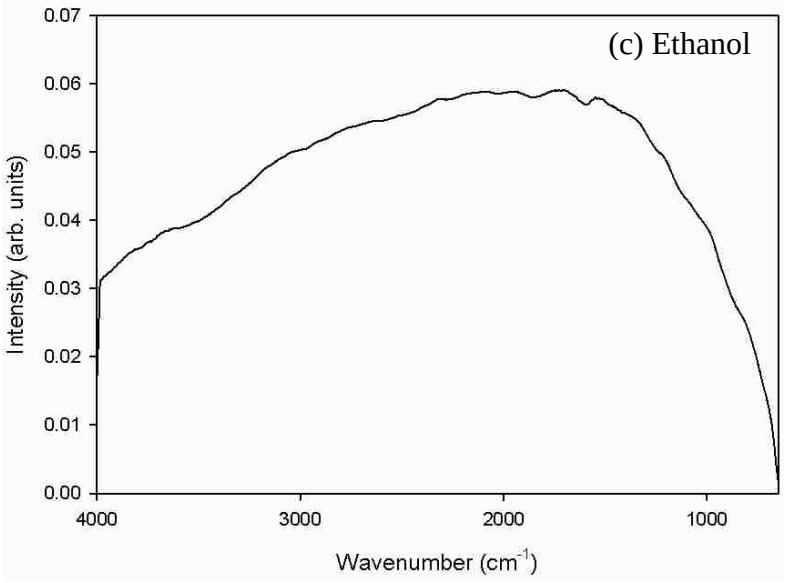

Figure 4- 31: FTIR analysis inside the wear track at 10^6 sliding cycles under 2N boundary lubrication with (a) E85/5W30 lubrication where adsorption of alcohol bands can be identified. (b) 5W30 lubricated wear tracks were no alcohol layers can be identified. (c) Lubricated with only ethanol were large oxide formation occurred. No film formation was evidenced with only ethanol.

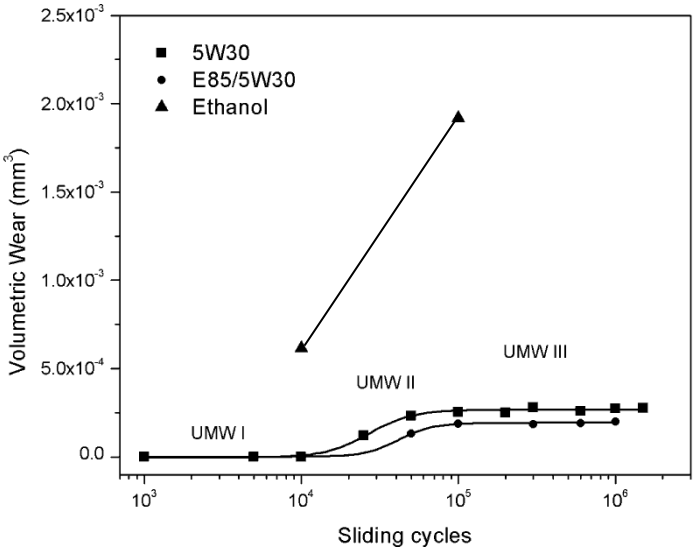

Figure 4- 32: Volumetric wear loss of Al-12.6% against sliding cycles with only ethanol lubrication, 5W30 lubrication and a mixture of 5W30/E85 at room temperature in boundary lubrication using 2N load with a sliding speed of 5 cm/s.

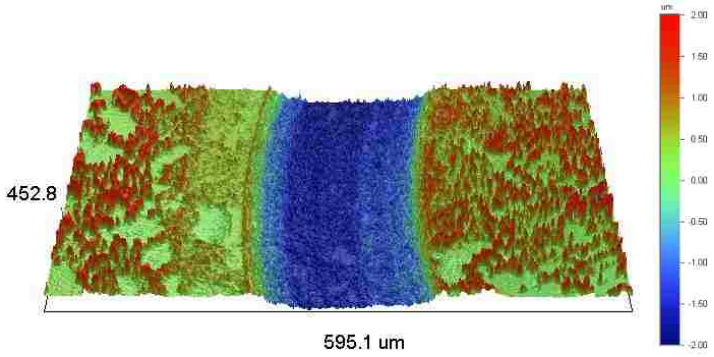

Figure 4- 33: 3D profilometry image of the wear track at 10^5 sliding cycles with ethanol lubrication.

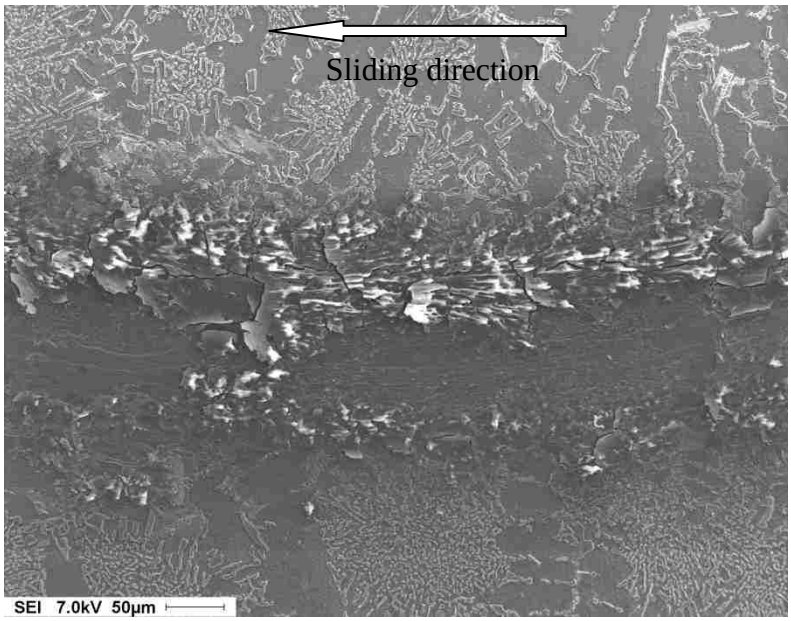

Figure 4- 34: Secondary electron micrograph inside the wear track at 10^4 sliding cycles with ethanol lubrication.

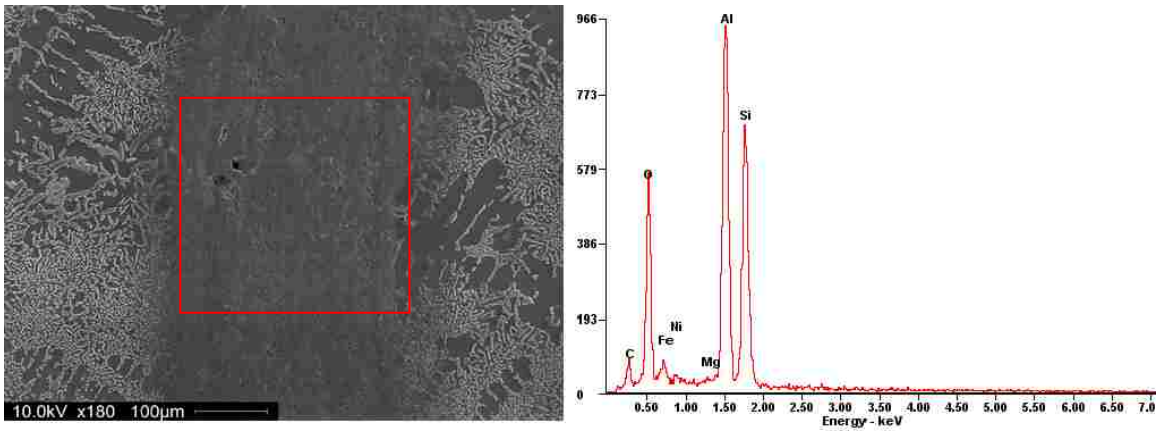

Figure 4- 35: EDS analysis inside wear track at 10^5 sliding cycles with only ethanol lubrication. Formation of aluminum oxide was evident.

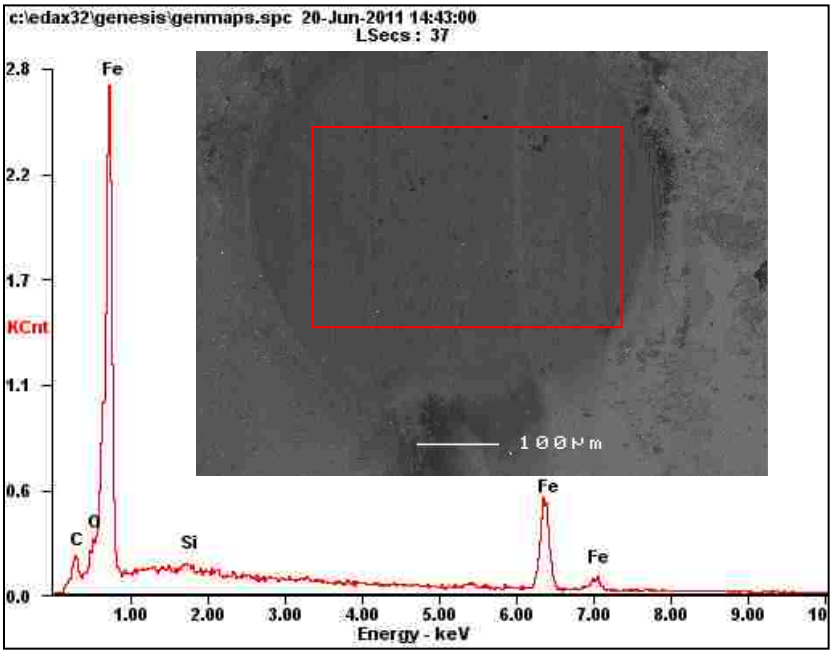

Figure 4- 36: Semi-quantitative EDS analysis on the worn surface of the counterface at 10^5 sliding cycles with only ethanol lubrication. Mainly iron oxide and Si fragments were detected.

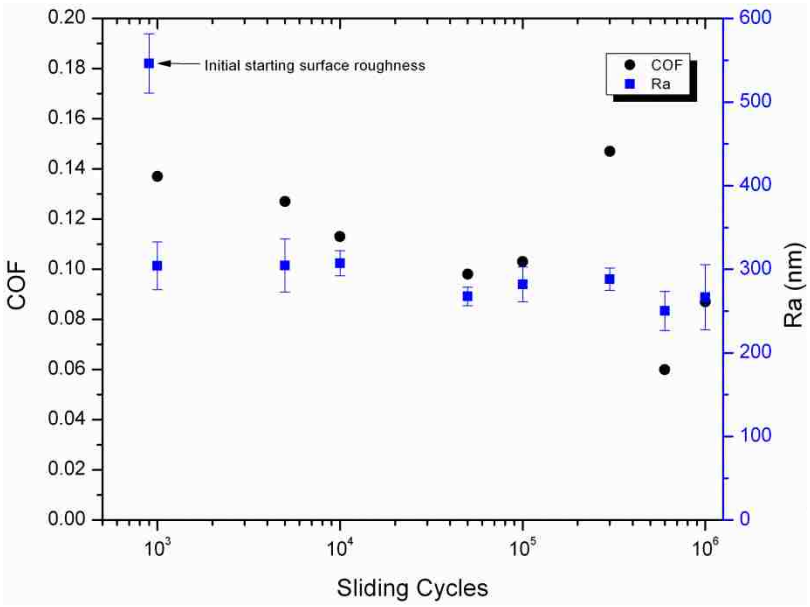

Figure 4- 37: Coefficient of friction values and surface roughness (Ra) inside the wear track lubricated with a mixture of E85/5W30 as a function of sliding cycles. Surface roughness measured from 8 different locations.

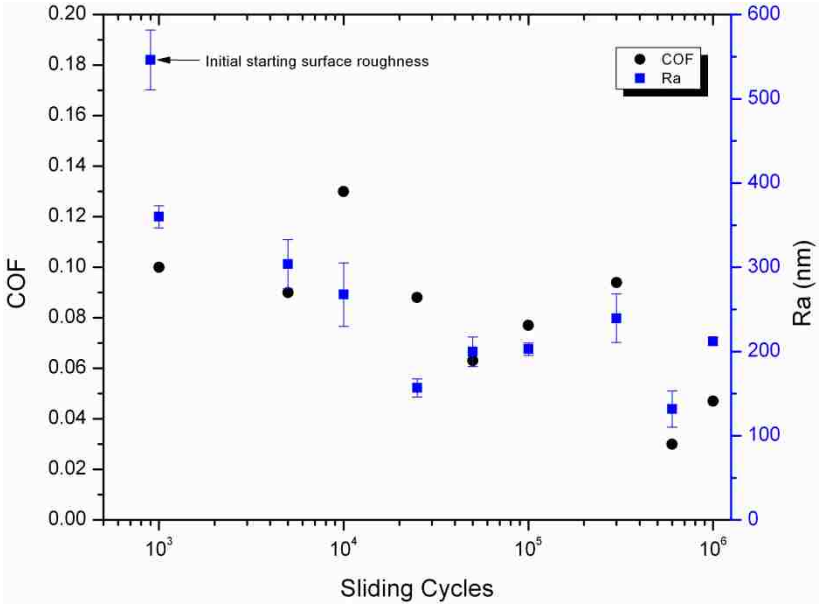

Figure 4- 38: Coefficient of friction values and surface roughness (Ra) inside the wear track lubricated with 5W30 as a function of sliding cycles. Surface roughness measured from 8 different locations.

CHAPTER V DISCUSSION

5.1 Introduction

This chapter discusses the wear mechanism for boundary lubricated conditions. The first section describes the mechanism of wear with only 5W30 lubrication. The second section describes the wear mechanism with E85 plus 5W30 lubrication.

5.2 Wear mechanism with engine oil

The wear mechanism of the Al-Si engine alloy under boundary lubrication with 5W30 can be characterized by three stages of ultra mild wear (UMW). Each progressive stage plays an important role in the overall development of the wear mechanism. In the first stage of UMW I, the contact between the counterface and the Al-Si alloy is limited to the top of silicon particles which protrude above the aluminum matrix. It is reasonable to suggest that the entire load is supported by the silicon particles because the silicon particles begin to crack and fracture leaving the matrix relatively undamaged [4, 6]. In addition, the silicon particles begin to embed into the matrix and can be evidenced by the formation of pileup, which occurs in order to accommodate the displacement caused by the semi-rigid particle indentation into the plastically deforming matrix. The progression of sliding results in a point where the embedding silicon particles and the piled-up matrix reach the same height. This signals the transition to the UMW II stage. The counterface and the matrix make contact, and deformed aluminum can be evidenced along the sliding direction. The material removal occurs due to the formation of grooves throughout the wear track. Formation of the oil residue layer can be evidenced in this regime. Round pockets of oil residue develop on top of hard silicon particles and on iron nickel phases. The formation of these pockets on the top of the harder particles can be attributed to the

resistance to deformation which they posses, which is a severe contrast to the softer aluminum matrix. Rounder pockets of oil residue are easily visible towards the edges of the wear track where less deformed aluminum smears over the pockets of oil residue due to the sliding of the counterface. Towards the centre of the wear track, the pockets of oil residue are less visible and can only be detected through EDS. The oil residue layer consists of Zn, S, Ca, C, and O as evidenced through XPS scans. Wear tracks appear to be uniform and consistent. The stabilization of the wear rates can be attributed to the formation of a stable oil residue layer. Similar observations have been reported by authors confirming the progression of wear in the UMW regime [4, 6, 9, 51].

5.3 Wear mechanism with 5W30 plus E85

Wear tests using a mixture of E85/5W30 on the Al-12.6 wt.% Si alloy provided the necessary wear resistance during sliding contact with a steel counterface. The wear resistance of the Al-12.6 wt.% Si alloy in the presence of E85/5W30 mixture can be discussed in terms of combined mechanical and chemical mechanisms. Three stages of UMW were observed. UMW I stage occurs over the period where the contact is limited to only silicon particles. Fracturing and embedding of the silicon particle into the soft aluminum matrix occurs. The embedding of the silicon particle forces the aluminum to pile-up adjacent to the embedding particle. Since the wear damage is only limited to silicon particles the aluminum matrix remains unaffected contributing to zero volume loss. Transition to the UMW II stage is accompanied by an increase in the volume wear. The piled-up aluminum and the embedding silicon particles reach the same height, exposing the aluminum to the counterface. Damage to the matrix occurs in the form of long grooves and scratches. The development of a protective oil residue film due to the interaction of engine oil additives were confirmed through semi-quantitative chemical

(EDS) analysis and quantitative XPS. Wear tracks which were lubricated with only engine oil showed the formation of concentrated pockets of oil residue which develop on top of the harder silicon and iron-nickel particles. When E85 was added to the engine oil, the formation of the pockets of oil residue was less evident. The absence of pockets of oil residue may be due to the thinning of the engine oil and the dilution of the engine oil.

The addition of E85 in engine oil did not significantly affect the development of the protective oil residue layer. Quantitative XPS chemical analysis on the surface of the mixed lubricated wear track produced a richer concentration of elements (Zn, S, and Ca) due to the engine oil additive. Engine oil additives such as ZDDP under pressure and elevated temperatures form stable protective oil residue films, rich in Zn, S, P, C, and Ca [4, 9, 51]. ZDDP additives also function as effective oxidation inhibitors by generating products which themselves act as effective oxidation inhibitors [48]. If ZDDP is mixed with large peroxides or by-products of combustion, the main ability of ZDDP as an effective antiwear agent is reduced resulting in reactions products such as dithiphosphate mono- and disulphides and either $ZnSO_4$ or ZnO. Andersson [65] observed through Raman spectroscopy on pure ZDDP crystals that when mixed with alcohol (ethanol/methanol), ZDDP decomposes into various molecules and by-products. It is reasonable to suggest that due to the presence of large amounts of alcohol in the engine oil, the ZDDP additives were effective in reducing the amount of oxidation development resulting in ZnO film formation and a rich deposit of Zn, S, and Ca as evidenced through the quantitative XPS analysis on the surface of the wear track.

The prevention of oxide layer formation through the development of a protective oil residue layer is an essential stage in preventing high wear rates. Wear tests in the

presence of only ethanol resulted in aluminum and iron oxide formation, resulted in high wear rates, unacceptable for linerless Al-Si engine operation.

Upon transition to the UMW III stage, the stabilization of the volume wear can be noticed. The stabilization of the wear rates can be attributed to the formation of a protective tribofilm. Dey et al. [6] and Meng et al. [8] who investigated the effect of tribofilm formation on Al-12.6 wt.% Si alloy lubricated with engine oil at room temperature concluded that a continuous tribofilm with a thickness of 40-80 nm can be expected in the UMW III stage under similar wear conditions. Subsurface characterization of the wear track which developed under the mixed lubricated condition at $3x10^5$ (UMW III) sliding cycles showed discontinuous oil residue film development.

Even though a discontinuous oil residue film was evidenced, low volume wear rates were still observed. This may be explained by observing the chemical reactions which occur during sliding contact. Hydrocarbons and alcohols have the ability to chemically adsorb and even react with metal surface which are often activated and accelerated by friction [66]. The negative-ion-radical action mechanism (NIRAM) can be used to further illustrate the interaction of alcohol during boundary lubrication. During the course of friction between two contacting bodies' particularly asperities, low-energy electrons are emitted creating positively charged spots on the contacting surface. The emitted low energy electrons (1-4 eV) react with the alcohol molecule to form negative ions and radicals. The negatively charged ions subsequently react with the positively charged spots to form protective antiwear tribochemical films responsible for maintaining low wear rates.

During the course of sliding, when the aluminum matrix became exposed to the counterface in UMW II, the exposed aluminum became positively charged, allowing for

the negatively charged alcohol ion to bond to the surface. Evidence for the chemically adsorbed/reacted tribochemical film was presented in the form of FTIR scans. The vibration of the O-H, C-H, and C-O bands suggests that these films existed inside the wear track. These adsorption bands were not evidenced with only engine oil lubrication and with only ethanol lubrication. Ethanol provided only limited lubricity, resulting in oxide layer formation (aluminum oxide and iron oxide) and prevented the formation of any protective tribochemical films. When E85 was mixed with engine oil, the formation of protective oil reside layers prevented oxide formation and allowed for the protective tribochemical film to be formed. Shown in Figure 5- 1 is a schematic of the proposed tribochemical film which occurs due to the sliding contact on Al-Si alloys. When the counterface passes over these films, it can be assumed that smearing of the aluminum over these films is possible over time, allowing the films to be developed in layers. Quantitative XPS depth characterization showed a rich concentration of carbon as a function of depth on wear tracks lubricated with E85 plus engine oil in comparison to just engine oil, suggesting that the protective carbon-rich tribochemical film became incorporated into the wear track. In addition, TEM characterization showed a thin layer of smeared aluminum on top of silicon particles, suggesting that the tribochemical film formation could also occur on top of the silicon particles.

The UMW mechanism for Al-12.6 wt.%Si alloy lubricated with 5W30 plus E85 can be summarized with a schematic diagram as shown in Figure 5- 2. During UMW-I the damage was limited to only silicon particles which fracture and embed into the matrix. Formation of pileup occurs. Embedding of the particle continuous the pileup material and the embedding silicon particles reach the same height, exposing the aluminum matrix to the counterface in UMW II. Protective tribochemical film due to

alcohol develops on top of exposed aluminum, providing a thin wear resistant layer. Oil additive layer develops onto of harder silicon and nickel-iron particles, proving an additional layer of support. Once a stable oil residue layer in conjunction with an alcohol adsorbed tribochemical layer forms on top of a sliding induced ultra fine aluminum grains, a reduction in the wear rate was observing, resulting in UMW III (Figure 5-2 b).

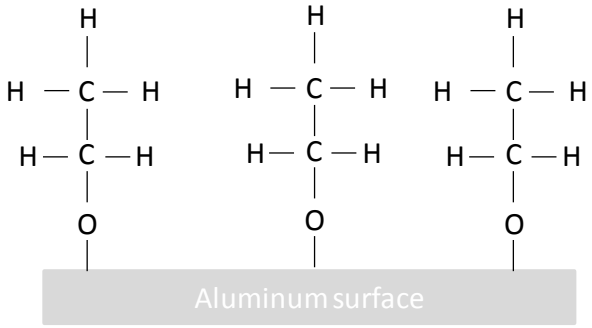

Figure 5- 1: Schematic of the possible tribochemical film formation on top of aluminum due to alcohol interaction.

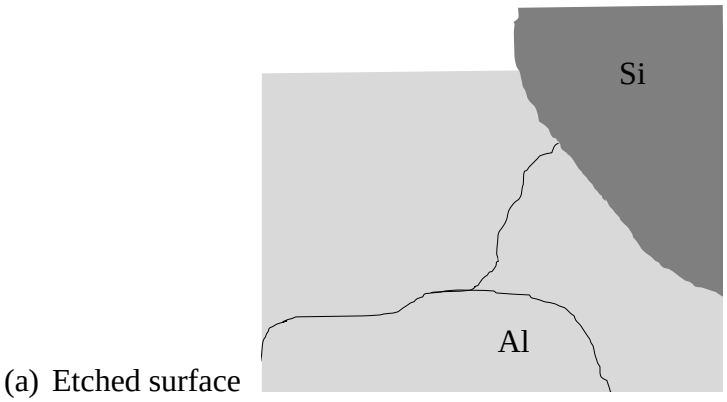

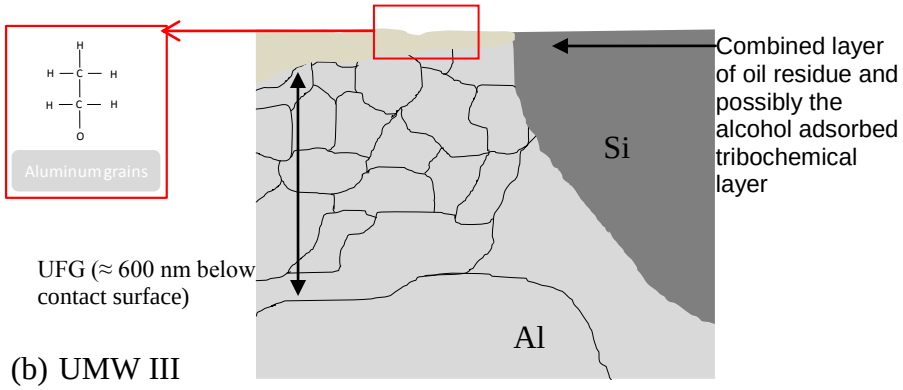

Figure 5- 2: Schematic diagram showing the UMW mechanism in Al-12.6 wt.% Si alloy using E85 plus 5W30 lubrication. (a) etched surface; (b) UMW III

CHAPTER VI CONCLUSIONS

1. Al-12.6% Si engine alloy was used in order to determine the damage in the UMW regime by first chemically etching the surface with 10% NaOH. The prepared surface is to represent the surface of a linerless Al-Si engine. Wear tests were conducted under boundary lubrication condition with only synthetic engine oil (5W30) or a contaminated engine oil conditions with a 1:1 mixture of synthetic engine oil (5W30) and E85 (85% ethanol and 15% regular gasoline) fuel.
2. Damage which was sustained on the surface of the Al-12.6% Si alloy after wear tests were quantified and characterized in order to determine the damage mechanism in the UMW regime.
3. Wear tests under both lubricated conditions showed similar UMW characteristics; however, lower wear rates were obtained when engine oil was mixed with E85 fuel.
4. The formation of the oil residue layer was evidenced for both lubricated conditions. The alcohol may act to prevent the formation of a thick oil residue layer; however, proved to be beneficial by forming tribochemical film due to the alcohol, resulting in less wear.
5. Polar attraction between the hydroxyl group (- OH) in the alcohol and the lubricating surface provided a suitable condition for an alcohol adsorbed layer to form which may provide an extra layer of wear resistance on the Al-Si alloy.
6. Wear tests with only ethanol resulted in mild wear conditions and the formation of aluminum oxide.

7. Addition of E85 in engine oil resulted in a slight increase in COF values in comparison to only engine oil.
8. Addition of E85 into engine oil does not result in any excess wear or any corrosive damage.

SUGGESTIONS FOR FUTURE RESEARCH

The complex mechanism of wear on the Al-12.6 wt.% Si alloy with E85 and engine oil lubrication was investigated focusing mainly on the effect of ethanol addition. Preliminary evidence was presented for the formation of a protective tribochemical film due to alcohol. The following suggestions have been recommended in order to better understand the interaction of alcohol during boundary lubricated conditions:

1. Chemical analysis employing ToF-SIMS can give insight into the structure of the tribochemical film on the Al-Si surface.
2. The effect of E85 on the wear behaviour of only engine oil additive packages should be investigated.
3. The wear behaviour of engine oil contaminated with water should be investigated since high concentration of water formulation has been suggested following engine oil analysis on bio-fuelled vehicles.
4. Wear mechanism should be correlated with linerless Al-Si engine following field tested conditions.
5. The stability of the oil residue layer and the tribochemical layer should be investigated.
6. The counterface material should be investigated in order to quantify the amount of volume loss and characterize the damage progression.

REFERENCES

[1] S. C. Tung and M. L. McMillan, "Automotive tribology overview of current advances and challenges for the future," *Tribology International,* vol. 37, pp. 517-536, 2004.

[2] E. P. Becker, "Trends in tribological materials and engine technology," *Tribology International,* vol. 37, pp. 569-575, 2004.

[3] R. E. Green, "Die Casting the Vega Engine Block," *Die Casting Engineer,* vol. 14, pp. 12-26, 1970.

[4] M. Chen, *et al.*, "Micromechanisms and mechanics of ultra-mild wear in Al-Si alloys," *Acta Materialia,* vol. 56, pp. 5605-5616, 2008.

[5] S. K. Dey, *et al.*, "Micromechanisms of low load wear in an Al-18.5% Si alloy," *Wear,* vol. 267, pp. 515-524, 2009.

[6] S. K. Dey, *et al.*, "Ultra-mild wear mechanisms of Al- 12.6 wt.% Si alloys at elevated temperature," *Wear,* 2011.

[7] M. Chen and A. T. Alpas, "Ultra-mild wear of a hypereutectic Al-18.5 wt.% Si alloy," *Wear,* vol. 265, pp. 186-195, 2008.

[8] X. Meng-Burany, *et al.*, "Subsurface sliding wear damage characterization in Al-Si alloys using focused ion beam and cross-sectional TEM techniques," *Wear,* vol. 270, pp. 152-162, 2011.

[9] M. A. Nicholls, *et al.*, "X-ray absorption spectroscopy of tribofilms produced from zinc dialkyl dithiophosphates on Al-Si alloys," *Wear,* vol. 257, pp. 311-328, 2004.

[10] G. Pereira, *et al.*, "Chemical characterization and nanomechanical properties of antiwear films fabricated from ZDDP on a near hypereutectic Al–Si alloy," *Tribology Letters,* vol. 18, pp. 411-427, 2005.

[11] P. De Silva, *et al.*, "Tribometer Investigation of the Frictional Response of Piston Rings when Lubricated with the Separated Phases of Lubricant Contaminated with the Gasoline Engine Biofuel Ethanol and Water," *Tribology Letters,* vol. 43, pp. 107-120, 2011.

[12] S. C. Tung and H. Gao, "Tribological characteristics and surface interaction between piston ring coatings and a blend of energy-conserving oils and ethanol fuels," *Wear,* vol. 255, pp. 1276-1285, 2003.

[13] S. E. Schwartz, "Laboratory Studies of the Effects of Methanol Fuel on Engine Oil and Materials," presented at the VI International Symposium on Alcohol Fuels Technology, Ottawa, Canada, 1984.

[14] X. Hu, *et al.*, "Tribochemical effect of impurities in zinc dialkyldithiophosphate in engine oil," *Lubrication Science,* vol. 15, pp. 351-360, 2003.

[15] C. Kajdas and W. Liu, "Tribochemistry of aluminium and aluminium alloy systems lubricated with liquids containing alcohol or amine additive types and some other lubricants — a review," *Lubrication Science,* vol. 16, pp. 267-292, 2004.

[16] Y. Wan, *et al.*, "Effects of diol compounds on the friction and wear of aluminum alloy in a lubricated aluminum-on-steel contact," *Wear,* vol. 193, pp. 99-104, 1996.

[17] S. Igari, *et al.*, "Effects of molecular structure of aliphatic diols and polyalkylene glycol as lubricants on the wear of aluminum," *Wear,* vol. 244, pp. 180-184, 2000.

[18] H. Yanhong and L. Weimin, "Tribological properties of alcohols as lubricating additives for aluminum-on-steel contact," *Wear,* vol. 218, pp. 244-249, 1998.
[19] L. Hu, *et al.*, "Investigation of tribochemical behavior of Al-Si alloy against itself lubricated by amines," *Wear,* vol. 243, pp. 60-67, 2000.
[20] T. Kubo, *et al.*, "Chemical analysis of boundary lubrication film formed on metal nitride coatings with ethanol by means of TOF-SIMS," *Wear,* vol. 268, pp. 1225-1229, 2010.
[21] B. S. Andersson, "Paper XVIII (iii) Company Perspectives in Vehicle Tribology - Volvo," in *Tribology Series*. vol. Volume 18, C. M. T. D. Dowson and M. Godet, Eds., ed: Elsevier, 1991, pp. 503-506.
[22] S. Tung and H. Gao, "Tribological Investigation of Piston Ring Coatings Operating in an Alternative Fuel and Engine Oil Blend," *Tribology Transactions,* vol. 45, pp. 381-389, 2002.
[23] M. Chen, *et al.*, "Ultra-mild wear in eutectic Al-Si alloys," *Wear,* vol. 263, pp. 552-561, 2007.
[24] B. E. Slattery, *et al.*, "Microstructural evolution of a eutectic Al-Si engine subjected to severe running conditions," *Materials Science and Engineering: A,* vol. 512, pp. 76-81, 2009.
[25] B. E. Slattery, *et al.*, "Investigation of wear induced surface and subsurface deformation in a linerless Al-Si engine," *Wear,* vol. 269, pp. 298-309, 2010.
[26] A. Edrisy, *et al.*, "Investigation of scuffing damage in aluminum engines with thermal spray coatings," *Wear,* vol. 259, pp. 1056-1062.
[27] A. Edrisy, *et al.*, "Wear mechanism maps for thermal-spray steel coatings," *Metallurgical and Materials Transactions A,* vol. 36, pp. 2737-2750, 2005.
[28] H. Ye, "An overview of the development of Al-Si-Alloy based material for engine applications," *Journal of Materials Engineering and Performance,* vol. 12, pp. 288-297, 2003.
[29] J. Murray and A. McAlister, "The Al-Si (Aluminum-Silicon) system," *Journal of Phase Equilibria,* vol. 5, pp. 74-84, 1984.
[30] A. R. Riahi, *et al.*, "Scuffing resistances of Al-Si alloys: effects of etching condition, surface roughness and particle morphology," *Materials Science and Engineering A,* vol. 343, pp. 76-81, 2003.
[31] J. L. Jorstad, "The hypereutectic aluminum silicon alloy used to cast the vega engine block," *Modern Casting,* vol. 1971, pp. 59-61, 1971.
[32] S. Das, *et al.*, "Effect of surface etching on the lubricated sliding wear of an eutectic aluminium–silicon alloy," *Tribology Letters,* vol. 21, pp. 193-204, 2006.
[33] Y. Wang, *et al.*, "Scuffing resistance of coated piston skirts run against cylinder bores," *Wear,* vol. 259, pp. 1041-1047, 2005.
[34] S. C. Lim and M. F. Ashby, "Wear-Mechanism Maps," *Acta metallurgica,* vol. 35, pp. 1-24, 1987.
[35] Y. Liu, *et al.*, "A map for wear mechanisms in aluminium alloys," *Journal of Materials Science,* vol. 26, pp. 99-102, 1991.
[36] J. Zhang and A. T. Alpas, "Delamination wear in ductile materials containing second phase particles," *Materials Science and Engineering: A,* vol. 160, pp. 25-35, 1993.
[37] J. Zhang and A. T. Alpas, "Transition between mild and severe wear in aluminium alloys," *Acta Materialia,* vol. 45, pp. 513-528, 1997.

[38] T. S. Eyre, "Wear Characteristics of Castings Used in Internal-Combustion Engines," *Metals technology*, vol. 11, pp. 81-90, 1984.
[39] B. K. Yen and T. Ishihara, "Effect of humidity on friction and wear of Al---Si eutectic alloy and Al---Si alloy-graphite composites," *Wear*, vol. 198, pp. 169-175, 1996.
[40] H. Goto, *et al.*, "The influence of oxygen and water vapour on the friction and wear of an aluminium alloy under fretting conditions," *Wear*, vol. 116, pp. 141-155, 1987.
[41] M. Elmadagli and A. T. Alpas, "Progression of wear in the mild wear regime of an Al-18.5% Si (A390) alloy," *Wear*, vol. 261, pp. 367-381, 2006.
[42] X. Y. Li and K. N. Tandon, "Mechanical mixing induced by sliding wear of an Al-Si alloy against M2 steel," *Wear*, vol. 225-229, pp. 640-648, 1999.
[43] J. Li, *et al.*, "FIB and TEM characterization of subsurfaces of an Al-Si alloy (A390) subjected to sliding wear," *Materials Science and Engineering: A*, vol. 421, pp. 317-327, 2006.
[44] A. Somi Reddy, *et al.*, "Mechanism of seizure of aluminium-silicon alloys dry sliding against steel," *Wear*, vol. 181-183, pp. 658-667, 1995.
[45] S. Wilson and A. T. Alpas, "Wear mechanism maps for metal matrix composites," *Wear*, vol. 212, pp. 41-49, 1997.
[46] K. C. Ludema, "A review of scuffing and running-in of lubricated surfaces, with asperities and oxides in perspective," *Wear*, vol. 100, pp. 315-331, 1984.
[47] P. A. Willermet, "Some engine oil additives and their effects on antiwear film formation," *Tribology Letters*, vol. 5, pp. 41-47, 1998.
[48] H. Spikes, "The History and Mechanisms of ZDDP," *Tribology Letters*, vol. 17, pp. 469-489, 2004.
[49] M. Chen, "Mechanics and mechanisms of surface damage in Al-Si alloys under ultra-mild wear conditions," Engineering Materials, Mechanical, Materials and Automotive engineering, University of Windsor, Windsor, 2008.
[50] J. M. Martin, *et al.*, "Synergistic effects in binary systems of lubricant additives: a chemical hardness approach," *Tribology Letters*, vol. 8, pp. 193-201, 2000.
[51] R. Heuberger, *et al.*, "XPS study of the influence of temperature on ZnDTP tribofilm composition," *Tribology Letters*, vol. 25, pp. 185-196, 2007.
[52] C. Grossiord, *et al.*, "Tribochemical interactions between Zndtp, Modtc and calcium borate," *Tribology Letters*, vol. 8, pp. 203-212, 2000.
[53] A. R. Riahi and A. T. Alpas, "Fracture of silicon-rich particles during sliding contact of Al-Si alloys," *Materials Science and Engineering: A*, vol. 441, pp. 326-330, 2006.
[54] Z. Ye, *et al.*, "An experimental investigation of piston skirt scuffing: a piston scuffing apparatus, experiments, and scuffing mechanism analyses," *Wear*, vol. 257, pp. 8-31, 2004.
[55] B. Slattery, "Linerless Eutectic Al-Si Engine Wear: Microstructural Evolution " Masters, Materials Engineering, University of Windsor, Windsor, Ontario, Canada, 2009.
[56] I. M. Hutchings, *Tribology : friction and wear of engineering materials*: Boca Raton, 1992.
[57] D. M. R. Raudys, "Internal-Combustion Engine Adaptaion for Using Ethanol Fuel," in *9th International Conference "Transport Means 2005"*, 2005.

[58] J. Weaver, *et al.*, "Composition and Behavior of Fuel Ethanol," vol. EPA/600/R-09/037, ed. Athens, GA: U.S. Environmental Protection Agency, 2009.
[59] B. Swiecki, "To E or not to E, The debate over E85," *Stamping Journal*, vol. September p. 26, 2006.
[60] S. Tung and S. Tseregounis, "An Investigation of Tribological Characteristics of Energy-Conserving Engine Oils Using a Reciprocating Bench Test," *SAE Technical Paper*, vol. 2000-01-1781, 2000.
[61] H. W. J. Marbach, *et al.*, "Effects of alcohol fuels and fully formulated lubricants on engine wear," *Journal Name: SAE Prepr.; (United States)*, p. Medium: X; Size: Pages: vp, 1981.
[62] HU, *et al.*, *Effect of 2-ethylhexanol on properties of zinc dialkyldithiophosphate* vol. 48. Leipzig, ALLEMAGNE: Fuchs-Informationsaufbereitung und-Verbreitung, 1996.
[63] R. E. Maples, "Petroleum Refinery Process Economics (2nd Edition)," ed: PennWell.
[64] P. R. Griffiths and J. A. De Haseth, *Fourier transform infrared spectrometry*. New York: Wiley, 1986.
[65] J. Andersson, "Feasibility of high pressure tribochemistry experiments from Raman study of lubricant additives at ambient conditions," Applied Physics and Mechanical Engineering / Physics, Luleå University of Technology, Sweden 2009.
[66] C. Kajdas and K. Hiratsuka, "Tribochemistry, tribocatalysis, and the negative-ion-radical action mechanism," *Proceedings of the Institution of Mechanical Engineers, Part J: Journal of Engineering Tribology*, vol. 223, pp. 827-848, June 1, 2009 2009.

APPENDIX A

APPENDIX A: Volume wear rate calculations.

Volume wear loss for each sample is quantified by obtaining three profilometry data from one WYKO image, indicated as profilometry line 1 (Column A&B), 2 (Column G&H), and 3(Column M&N). The left (low) and right (high) side of the wear track was used to quantify only the volume loss from within the wear track. The cut-off point is determined based on height distribution data. Column C, D, and E are used to verify that the data is within the wear track and does not exceed the cut-off point. Similarly column I, J, K, O, P, and Q are used for profilometry line 2 and 3. Column F is used to calculate the area of material removed. The sum of column F is the area used to calculate the volume wear loss. A total of 24 profilometry data is used to average the area of material removed.

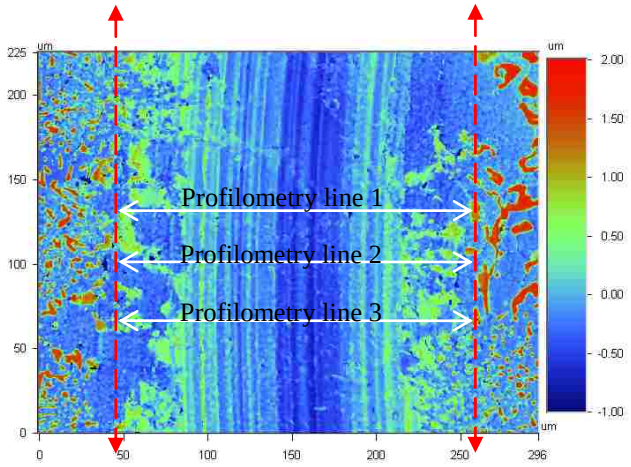

Left side of wear track (low)

Right side of wear track (high)

Profilometry line 1

Profilometry line 2

Profilometry line 3

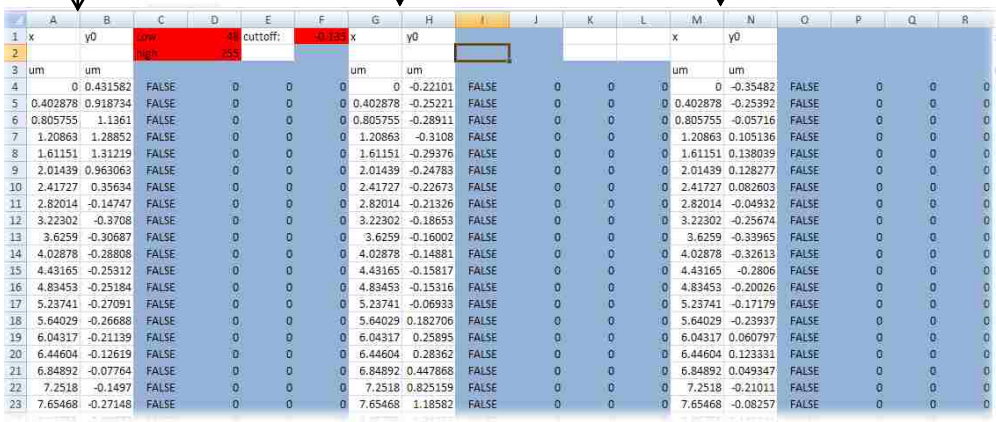

	A	B	C	D	E	F	G	H	I	J	K	L	M	N	O	P	Q	R
1	x	y0	low	48	cuttoff:	-0.125	x	y0					x	y0				
2			high	255														
3	um	um					um	um					um	um				
4	0	0.431582	FALSE	0	0	0	0	-0.22101	FALSE	0	0	0	0	-0.35482	FALSE	0	0	0
5	0.402878	0.918734	FALSE	0	0	0	0.402878	-0.25221	FALSE	0	0	0	0.402878	-0.25392	FALSE	0	0	0
6	0.805755	1.1361	FALSE	0	0	0	0.805755	-0.28911	FALSE	0	0	0	0.805755	-0.05716	FALSE	0	0	0
7	1.20863	1.28852	FALSE	0	0	0	1.20863	-0.3108	FALSE	0	0	0	1.20863	0.105136	FALSE	0	0	0
8	1.61151	1.31219	FALSE	0	0	0	1.61151	-0.29376	FALSE	0	0	0	1.61151	0.138039	FALSE	0	0	0
9	2.01439	0.963063	FALSE	0	0	0	2.01439	-0.24783	FALSE	0	0	0	2.01439	0.128277	FALSE	0	0	0
10	2.41727	0.35634	FALSE	0	0	0	2.41727	-0.22673	FALSE	0	0	0	2.41727	0.082603	FALSE	0	0	0
11	2.82014	-0.14747	FALSE	0	0	0	2.82014	-0.21326	FALSE	0	0	0	2.82014	-0.04932	FALSE	0	0	0
12	3.22302	-0.3708	FALSE	0	0	0	3.22302	-0.18653	FALSE	0	0	0	3.22302	-0.25674	FALSE	0	0	0
13	3.6259	-0.30687	FALSE	0	0	0	3.6259	-0.16002	FALSE	0	0	0	3.6259	-0.33965	FALSE	0	0	0
14	4.02878	-0.28808	FALSE	0	0	0	4.02878	-0.14881	FALSE	0	0	0	4.02878	-0.32613	FALSE	0	0	0
15	4.43165	-0.25312	FALSE	0	0	0	4.43165	-0.15817	FALSE	0	0	0	4.43165	-0.2806	FALSE	0	0	0
16	4.83453	-0.25184	FALSE	0	0	0	4.83453	-0.15316	FALSE	0	0	0	4.83453	-0.20026	FALSE	0	0	0
17	5.23741	-0.27091	FALSE	0	0	0	5.23741	-0.06933	FALSE	0	0	0	5.23741	-0.17179	FALSE	0	0	0
18	5.64029	-0.26688	FALSE	0	0	0	5.64029	0.182706	FALSE	0	0	0	5.64029	-0.23937	FALSE	0	0	0
19	6.04317	-0.21139	FALSE	0	0	0	6.04317	0.25895	FALSE	0	0	0	6.04317	0.060797	FALSE	0	0	0
20	6.44604	-0.12619	FALSE	0	0	0	6.44604	0.28362	FALSE	0	0	0	6.44604	0.123331	FALSE	0	0	0
21	6.84892	-0.07764	FALSE	0	0	0	6.84892	0.447868	FALSE	0	0	0	6.84892	0.049347	FALSE	0	0	0
22	7.2518	-0.1497	FALSE	0	0	0	7.2518	0.825159	FALSE	0	0	0	7.2518	-0.21011	FALSE	0	0	0
23	7.65468	-0.27148	FALSE	0	0	0	7.65468	1.18582	FALSE	0	0	0	7.65468	-0.08257	FALSE	0	0	0

Data break //

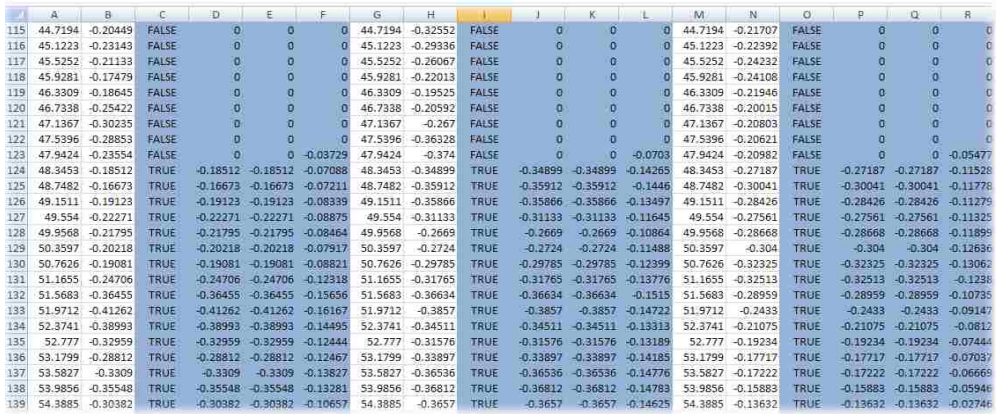

	A	B	C	D	E	F	G	H	I	J	K	L	M	N	O	P	Q	R
115	44.7194	-0.20449	FALSE	0	0	0	44.7194	-0.32552	FALSE	0	0	0	44.7194	-0.21707	FALSE	0	0	0
116	45.1223	-0.23143	FALSE	0	0	0	45.1223	-0.29336	FALSE	0	0	0	45.1223	-0.22392	FALSE	0	0	0
117	45.5252	-0.21133	FALSE	0	0	0	45.5252	-0.26067	FALSE	0	0	0	45.5252	-0.24232	FALSE	0	0	0
118	45.9281	-0.17479	FALSE	0	0	0	45.9281	-0.22013	FALSE	0	0	0	45.9281	-0.24108	FALSE	0	0	0
119	46.3309	-0.18645	FALSE	0	0	0	46.3309	-0.19525	FALSE	0	0	0	46.3309	-0.21946	FALSE	0	0	0
120	46.7338	-0.25422	FALSE	0	0	0	46.7338	-0.20592	FALSE	0	0	0	46.7338	-0.20015	FALSE	0	0	0
121	47.1367	-0.30235	FALSE	0	0	0	47.1367	-0.267	FALSE	0	0	0	47.1367	-0.20803	FALSE	0	0	0
122	47.5396	-0.28853	FALSE	0	0	0	47.5396	-0.36328	FALSE	0	0	0	47.5396	-0.20621	FALSE	0	0	0
123	47.9424	-0.23554	FALSE	0	0	-0.03729	47.9424	-0.374	FALSE	0	0	-0.0703	47.9424	-0.20982	FALSE	0	0	-0.05477
124	48.3453	-0.18512	TRUE	-0.18512	-0.18512	-0.07088	48.3453	-0.34899	TRUE	-0.34899	-0.34899	-0.14265	48.3453	-0.27187	TRUE	-0.27187	-0.27187	-0.11528
125	48.7482	-0.16673	TRUE	-0.16673	-0.16673	-0.07211	48.7482	-0.35912	TRUE	-0.35912	-0.35912	-0.1446	48.7482	-0.30041	TRUE	-0.30041	-0.30041	-0.11778
126	49.1511	-0.19123	TRUE	-0.19123	-0.19123	-0.08339	49.1511	-0.35866	TRUE	-0.35866	-0.35866	-0.13497	49.1511	-0.28426	TRUE	-0.28426	-0.28426	-0.11279
127	49.554	-0.22271	TRUE	-0.22271	-0.22271	-0.08875	49.554	-0.31133	TRUE	-0.31133	-0.31133	-0.11645	49.554	-0.27561	TRUE	-0.27561	-0.27561	-0.11325
128	49.9568	-0.21795	TRUE	-0.21795	-0.21795	-0.08464	49.9568	-0.2669	TRUE	-0.2669	-0.2669	-0.10864	49.9568	-0.28668	TRUE	-0.28668	-0.28668	-0.11899
129	50.3597	-0.20218	TRUE	-0.20218	-0.20218	-0.07917	50.3597	-0.2724	TRUE	-0.2724	-0.2724	-0.11488	50.3597	-0.304	TRUE	-0.304	-0.304	-0.12636
130	50.7626	-0.19081	TRUE	-0.19081	-0.19081	-0.08821	50.7626	-0.29785	TRUE	-0.29785	-0.29785	-0.12399	50.7626	-0.32325	TRUE	-0.32325	-0.32325	-0.13062
131	51.1655	-0.24706	TRUE	-0.24706	-0.24706	-0.12318	51.1655	-0.31765	TRUE	-0.31765	-0.31765	-0.13776	51.1655	-0.32513	TRUE	-0.32513	-0.32513	-0.1238
132	51.5683	-0.36455	TRUE	-0.36455	-0.36455	-0.15656	51.5683	-0.36634	TRUE	-0.36634	-0.36634	-0.1515	51.5683	-0.28959	TRUE	-0.28959	-0.28959	-0.10735
133	51.9712	-0.41262	TRUE	-0.41262	-0.41262	-0.16167	51.9712	-0.3857	TRUE	-0.3857	-0.3857	-0.14722	51.9712	-0.2433	TRUE	-0.2433	-0.2433	-0.09147
134	52.3741	-0.38993	TRUE	-0.38993	-0.38993	-0.14495	52.3741	-0.34511	TRUE	-0.34511	-0.34511	-0.13313	52.3741	-0.21075	TRUE	-0.21075	-0.21075	-0.0812
135	52.777	-0.32959	TRUE	-0.32959	-0.32959	-0.12444	52.777	-0.31576	TRUE	-0.31576	-0.31576	-0.13189	52.777	-0.19234	TRUE	-0.19234	-0.19234	-0.07444
136	53.1799	-0.28812	TRUE	-0.28812	-0.28812	-0.12467	53.1799	-0.33897	TRUE	-0.33897	-0.33897	-0.14185	53.1799	-0.17717	TRUE	-0.17717	-0.17717	-0.07037
137	53.5827	-0.3309	TRUE	-0.3309	-0.3309	-0.13827	53.5827	-0.36536	TRUE	-0.36536	-0.36536	-0.14776	53.5827	-0.17222	TRUE	-0.17222	-0.17222	-0.06669
138	53.9856	-0.35548	TRUE	-0.35548	-0.35548	-0.13281	53.9856	-0.36812	TRUE	-0.36812	-0.36812	-0.14783	53.9856	-0.15883	TRUE	-0.15883	-0.15883	-0.05946
139	54.3885	-0.30382	TRUE	-0.30382	-0.30382	-0.10657	54.3885	-0.3657	TRUE	-0.3657	-0.3657	-0.14625	54.3885	-0.13632	TRUE	-0.13632	-0.13632	-0.02746

Data break //

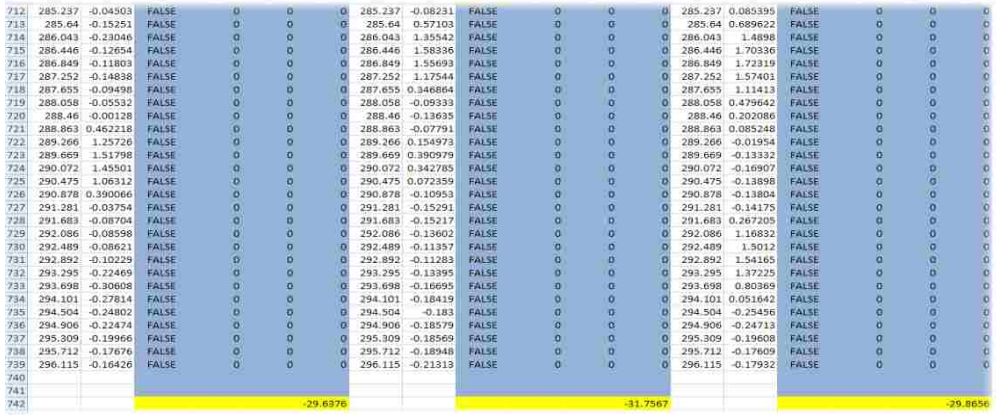

712	285.237	-0.04503	FALSE	0	0	0	285.237	-0.08231	FALSE	0	0	0	285.237	0.085395	FALSE	0	0	0
713	285.64	-0.15251	FALSE	0	0	0	285.64	0.57103	FALSE	0	0	0	285.64	0.689622	FALSE	0	0	0
714	286.043	-0.23046	FALSE	0	0	0	286.043	1.35542	FALSE	0	0	0	286.043	1.4898	FALSE	0	0	0
715	286.446	-0.12654	FALSE	0	0	0	286.446	1.58336	FALSE	0	0	0	286.446	1.70336	FALSE	0	0	0
716	286.849	-0.11803	FALSE	0	0	0	286.849	1.55693	FALSE	0	0	0	286.849	1.72319	FALSE	0	0	0
717	287.252	-0.14838	FALSE	0	0	0	287.252	1.17544	FALSE	0	0	0	287.252	1.57401	FALSE	0	0	0
718	287.655	-0.09498	FALSE	0	0	0	287.655	0.346864	FALSE	0	0	0	287.655	1.11413	FALSE	0	0	0
719	288.058	-0.05532	FALSE	0	0	0	288.058	-0.09333	FALSE	0	0	0	288.058	0.479642	FALSE	0	0	0
720	288.46	-0.00128	FALSE	0	0	0	288.46	-0.13635	FALSE	0	0	0	288.46	0.202086	FALSE	0	0	0
721	288.863	0.462218	FALSE	0	0	0	288.863	-0.07791	FALSE	0	0	0	288.863	0.085248	FALSE	0	0	0
722	289.266	1.25726	FALSE	0	0	0	289.266	0.154973	FALSE	0	0	0	289.266	-0.01954	FALSE	0	0	0
723	289.669	1.51798	FALSE	0	0	0	289.669	0.390979	FALSE	0	0	0	289.669	-0.13332	FALSE	0	0	0
724	290.072	1.45501	FALSE	0	0	0	290.072	0.342785	FALSE	0	0	0	290.072	-0.16907	FALSE	0	0	0
725	290.475	1.06312	FALSE	0	0	0	290.475	0.072359	FALSE	0	0	0	290.475	-0.13898	FALSE	0	0	0
726	290.878	0.390066	FALSE	0	0	0	290.878	-0.10953	FALSE	0	0	0	290.878	-0.13804	FALSE	0	0	0
727	291.281	-0.03754	FALSE	0	0	0	291.281	-0.15291	FALSE	0	0	0	291.281	-0.14175	FALSE	0	0	0
728	291.683	-0.08704	FALSE	0	0	0	291.683	-0.15217	FALSE	0	0	0	291.683	0.267205	FALSE	0	0	0
729	292.086	-0.08598	FALSE	0	0	0	292.086	-0.13602	FALSE	0	0	0	292.086	1.16832	FALSE	0	0	0
730	292.489	-0.08621	FALSE	0	0	0	292.489	-0.11357	FALSE	0	0	0	292.489	1.9012	FALSE	0	0	0
731	292.892	-0.10229	FALSE	0	0	0	292.892	-0.11283	FALSE	0	0	0	292.892	1.54165	FALSE	0	0	0
732	293.295	-0.22469	FALSE	0	0	0	293.295	-0.13395	FALSE	0	0	0	293.295	1.37225	FALSE	0	0	0
733	293.698	-0.30608	FALSE	0	0	0	293.698	-0.16695	FALSE	0	0	0	293.698	0.80369	FALSE	0	0	0
734	294.101	-0.27814	FALSE	0	0	0	294.101	-0.18419	FALSE	0	0	0	294.101	0.051642	FALSE	0	0	0
735	294.504	-0.24802	FALSE	0	0	0	294.504	-0.183	FALSE	0	0	0	294.504	-0.25456	FALSE	0	0	0
736	294.906	-0.22474	FALSE	0	0	0	294.906	-0.18579	FALSE	0	0	0	294.906	-0.24713	FALSE	0	0	0
737	295.309	-0.19966	FALSE	0	0	0	295.309	-0.18569	FALSE	0	0	0	295.309	-0.19608	FALSE	0	0	0
738	295.712	-0.17676	FALSE	0	0	0	295.712	-0.18948	FALSE	0	0	0	295.712	-0.17609	FALSE	0	0	0
739	296.115	-0.16426	FALSE	0	0	0	296.115	-0.21313	FALSE	0	0	0	296.115	-0.17932	FALSE	0	0	0
740																		
741																		
742						-29.6376						-31.7567						-29.8656

VITA AUCTORIS

NAME: Victor Vimalrajan Francis

PLACE OF BIRTH: Vavuniya, Sri Lanka

DATE OF BIRTH: 1984

EDUCATION: Ontario Secondary School Diploma
Chaminade College School
Toronto, ON
1999– 2003

Bachelor of Applied Science
Honours Mechanical Engineering – Materials Option (Co-op)
University of Windsor
Windsor, ON
2003 – 2009

Master of Applied Science
Engineering Materials
University of Windsor
Windsor, ON